Clemson University

TigerPrints

All Theses Theses

12-2021

Development and Validation of an Analytical Modeling Tool for Solar Borehole Heat Exchangers

Adam Ornelles
adornel@clemson.edu

Follow this and additional works at: https://tigerprints.clemson.edu/all_theses

Part of the Environmental Engineering Commons

Recommended Citation

Ornelles, Adam, "Development and Validation of an Analytical Modeling Tool for Solar Borehole Heat Exchangers" (2021). *All Theses*. 3691.
https://tigerprints.clemson.edu/all_theses/3691

This Thesis is brought to you for free and open access by the Theses at TigerPrints. It has been accepted for inclusion in All Theses by an authorized administrator of TigerPrints. For more information, please contact kokeefe@clemson.edu.

Clemson University
TigerPrints

All Theses Theses

12-2021

Development and Validation of an Analytical Modeling Tool for Solar Borehole Heat Exchangers

Adam Ornelles

Follow this and additional works at: https://tigerprints.clemson.edu/all_theses

Part of the Environmental Engineering Commons

DEVELOPMENT AND VALIDATION OF AN ANALYTICAL MODELING TOOL FOR SOLAR BOREHOLE HEAT EXCHANGERS

A Thesis
Presented to
the Graduate School of
Clemson University

In Partial Fulfillment
of the Requirements for the Degree
Master of Science
Hydrogeology

---

by
Adam Davidson Ornelles
December 2021

Accepted by:
Ronald Falta, Comittee Chair
Lawrence Murdoch
Scott Brame

ABSTRACT

The objective of this project was to create an accessible analytical modeling tool for thermal borehole heat exchangers to be used for designing solar-powered remediation systems. Volatile Organic Compounds (VOCs) these systems are designed to remediate, such as chlorinated solvents, are an widespread groundwater contaminants across the United States. Due to their non-aqueous and degradation-resistant nature, chlorinated solvents persist in the environment for long periods leading to far-traveling contaminant plumes, necessitating subsurface remediation.

While many remediation methods are available to treat chlorinated solvents, they are all limited by cost and remediation time. Thermal In-Situ Sustainable Remediation systems (TISR^{TM}, U.S. patent number 10,384,246 & 10,688,545) were developed by Arcadis as a novel approach to reducing remediation costs by acting as a supplementary solution, powered by solar energy, to reduce the runtime of pre-existing remediation strategies. By moderately heating the subsurface 5-20 degrees Celsius to improve biodegradation and multiphase extraction, TISR systems can reduce the expected lifetime of remediation projects by half. TISR systems are relatively inexpensive and quickly contribute value that outweighs their cost. Because TISR units can be beneficial to most remediation efforts, there is interest in developing a rapid TISR modeling tool to expedite and streamline the design of TISR installations.

This project focuses on developing a simplified analytical modeling tool, coded in Visual Basic, that can be easily operated with a user interface in Excel. While more-

complex numerical models often offer superior accuracy in modeling heterogeneous systems, they can be excessively time-consuming and complicated for use in the field or for testing various system configurations quickly. The analytical modeling tool, as it is called, uses a novel solution to model borehole heat exchangers, able to simulate multiple boreholes at once in 3 dimensions with variable heat flow rates and groundwater flow. The objective of this research was to tune and validate the TISR modeling tool by comparing it to the proven TOUGH multiphase modeling codes and data from existing TISR pilot test sites. It was shown that the TISR modeling performs with similar accuracy to numerical modeling methods while accurately simulating data from real-world TISR pilot sites in Colorado and Mexico.

ACKNOWLEDGEMENTS

Deepest appreciation to my research advisor Dr. Falta, who always quickly responds to questions, is patient in his responses and is exceedingly knowledgeable in the field of hydrogeology and groundwater modeling. While life was difficult completing my thesis during the peak of COVID, Dr. Falta has guided me through the process.

Thank you to my committee member Dr. Murdoch who taught many fun classes on the topic of hydrogeology that expanded my perspective on mathematic strategies to solve geological problems during my education at Clemson.

Thanks to my committee member Prof. Scott Brame for leading a memorable COVID Clemson field camp for us TAs, who got to film well installations and more with cameras, microphones, and hand sanitizer. I am so thankful to have had the in-person field camp experience during covid due to his effort in adapting the course.

This research project was funded under project number ER20-5028, for the Environmental Security Technology Certification Program (ESTCP) in conjunction with Arcadis. Sincerest appreciation to the group at Arcadis for the data and correspondence.

Also, thanks to my partner Hannah for keeping me on track and motivated while she was simultaneously taking hydrogeology in grad school at UW Madison across the country.

TABLE OF CONTENTS

TITLE PAGE i
ABSTRACT ii
ACKNOWLEDGEMENTS vi
FIGURES vii
TABLES xii
1. INTRODUCTION 1
1.1 Characteristics of Analytical Versus Numerical Models 6
1.2 Thermal In-Situ Remediation 9
2. RESEARCH OBJECTIVES 14
3. DEVELOPING AN ANALYTICAL SOLUTION FOR LOW-TEMPERATURE BOREHOLE HEAT EXCHANGERS (TISR MODELING TOOL) 15
3.1 Background 15
3.2 Current Analytical Solutions for Borehole Heat Exchangers 15
3.3 Variable Line Source for Borehole Heat Exchangers 18
3.4 Superposition of Multiple Borehole Heat Exchangers 20
3.5 Variable Heat Flow over Transient Time Periods 21
3.6 Accounting for Partially Saturated Conditions 21
3.7 Solution for Adjusting Groundwater Flow Direction 23
3.8 Modeling Tool and Interface 24
4. CALCULATING HEAT FLOW FROM BOREHOLE HEAT EXCHANGERS 27
4.1 Background on TISR System Functionality 27
4.2 Calculating Heat Flow From Pre-Existing Borehole Data 28
4.3 Estimating Heat Flow from Solar Insolation For Modeling 30
4.3.1 Estimating Average Yearly Heat Flow Rate 30
4.3.2 Estimating Average Monthly Heat Flow Rate 32
5. COMPARISON OF ANALYTICAL AND NUMERICAL MODELS WITH NO GROUNDWATER FLOW 34
5.1 Single Borehole Heat Exchanger Models with No Flow 34
5.1.1 Methods: Identical Saturated Models 34
5.1.2 Results: Identical Saturated Models 38

5.1.3 Methods: Analytical Model Versus Partially Saturated Numerical Models 40
5.1.4 Results: Analytical Versus Partially Saturated Numerical Models 45
5.1.5 Methods: Analytical Model Versus High Permeability Numerical Model 49
5.1.6 Results: Analytical Model Versus High Permeability Numerical Model 50
5.2 Single Borehole Heat Exchanger Model with Groundwater Flow 53
5.2.1 Methods 53
5.2.2 Results 57
5.3 Multiple Borehole Heat Exchanger Model with Seasonally Variable Heat Flow .. 59
5.3.1 Methods 59
5.3.2 Results: Comparing Model Cross-Sections 64
5.3.3 Results: Identical Models 68
5.3.4 Results: Saturated Analytical Model vs. Partially Saturated Numerical Model69
5.4 Conclusions 70
6. SIMULATING THE COLORADO DEPARTMENT OF TRANSPORTATION TISR SITE USING THE TISR MODELING TOOL 73
6.1 Characterization of The CDOT Site 73
6.2 Methods 77
6.2.1 Calculating Actual Heat Flow (Q) from CDOT Site 77
6.2.2 Estimated Heat Flow (Q) Using the Solar Insolation Tool 78
6.2.3 Simulating the CDOT Site with the TISR Modeling Tool 79
6.3 Results 82
6.4 Conclusion 86
7. MEXICO SITE SIMULATION 89
7.1 Background 89
7.3 Results 93
7.4 Conclusion 94
8. FINAL CONCLUSIONS 96
REFERENCES 97
APPENDIX 101

FIGURES

Figure 1: Diagram of a Thermal In-Situ Remediation system (TISR^{TM}). Permission for use granted by Randhawa Davinder, Arcadis (Divine, 2020). 9

Figure 2: The relation of moderate subsurface temperature increase from a TISR system to elimination of TCE, and increase in constituents of Vinyl Chloride reduction (Divine, 2020). 11

Figure 3: Reduction in the active remediation time of TCE, based on standard biologically enhanced treatment, represented by the orange lines, versus the anticipated TISR-enhanced rate of treatment, versus the the expected natural attenuation rate of removal, in grey at the CDOT site (Divine, 2020). 13

Figure 4: Diagram of how the coordinate system in the analytical solution is rotated relative to the desired groundwater flow direction. 24

Figure 5: Example of the graphical user interface for the analytical modeling solution coded in Visual Basic..... 25

Figure 6: Example of the cross-sectional contour plots of heat using the Excel user interface. The x-y plot shows a top down view of the model at a set depth, the x-z cross-section shows the side view of the model along a set y coordinate. 26

Figure 7: Example of how transient temperature is recorded by the modeling tool at observation points placed around the borehole..... 26

Figure 8: Simplified conceptual model of TISR^{TM} systems, used to calculate heat flow from a borehole heat exchanger using borehole inlet and outlet temperature readings. 28

Figure 9: Example of the solar heat flow calculator tool that sends data to the analytical model..... 30

Figure 10: SRCC Certification for the “SPP-30A” solar collector, used as the representative rate of solar efficiency used to define 30-tube evacuated solar collectors in the model. 31

Figure 11: SRCC Certification for the “SPP-Spartan” flat panel, used as the representative rate of collector efficiency for flat panels in the model (the flat panel efficiency is referred to in units of energy per area as flat panel collector sizes vary more widely in area than evacuated tube arrays). 32

Figure 12: Example of monthly solar insolation rates relative to average, produced by the SRMONLAT ModelE AR5 Nasa code at various latititudes. 33

Figure 13: Conceptual model for comparing the analytical model to the numerical model in single borehole scenarios with no flow defining borehole placement and model boundaries. 36

Figure 14: 3-dimensional representation of the simplified model in Petrasim operating off the Toughv2.1 code. Boreholes and monitoring wells are represented by red lines, while grey lines outline the integral finite difference grid. 37

Figure 15: Saturated numerical model showing temperature gradient interpolated between grids at T=15 months after the boreholes were turned off. Presented as a 3-dimensional sliced plane view of z=-7 and y = 1. Model orientation indicated in the bottom left. 38

Figure 16: Comparison of temperatures observed in the saturated analytical flow model and saturated numerical flow model. Observation points at depth z=7.5m. 39

Figure 17: Cross-sectional view of the contours of water pressure in the partially saturated models, in Pascals. Numerical models have fixed pressure heads used to emulate a vadose zones. Model A) has a water table depth of 5 meters. Model B) has a depth to water table of 7.5 meters. Model C) has a depth to water table of 9 meters. 41

Figure 18: Interpolated heat conductivity, by depth, of the numerical models with water tables at depths of 5, 7.5, and 9 meters depth. 42

Figure 19: Heat conductivity plot used by the 5m, 7.5m, and 9m, analytical groundwater models to estimate average thermal conductivity along the length of the borehole from 5m to 10m depth. 43

Figure 20: Comparison of temperature over time observed in the saturated analytical model at a permeability of $1x10^{-12}$ and groundwater depth of 5 meters. Observation points at depth z=7.75m, 1m, 3m, and 5m from the BHE. 45

Figure 21: Comparison of temperature over time observed in the saturated analytical model at a permeability of $1x10^{-12}$ m^2 and groundwater depth of 7.5 meters. Observation points at depth z=7.75m, 1m, 3m, and 5m from the BHE. 46

Figure 22: Comparison of temperature over time observed in the saturated analytical model at a permeability of $1x10^{-12}$ m^2 and groundwater depth of 9 meters. Observation points at depth z=7.75m, 1m, 3m, and 5m from the BHE. 47

Figure 23: Cross sectional side view of the heat plume created by the borehole heat exchanger, in the numerical model at t = 360 days. 48

Figure 24: Cross sectional side view of the heat plume from the borehole heat exchanger created with the analytical model at t = 360 days. 49

Figure 25: Cross-sectional side view of the temperature contours in the A) analytical model assuming saturated conditions versus B) the numerical model at a permeability of $6x10^{-10}$ m^2 with an unsaturated zone directly above the borehole. 51

Figure 26: Comparison of the analytical and numerical model temperatures when simulating a system with a hydraulic conductivity of $9.81x10^{-4}$ m/s at a distance of 1m from the borehole, with the observation taken at 7.5m depth. 51

Figure 27: Average percent error, via NRMSE of the analytical model when attempting to model heat flow in increasingly high hydraulic conductivities, ranging from $9.8x10^{-9}$ to $4.9x10^{-3}$ m/s with measurements taken 1m from the borehole heat exchanger. 52

Figure 28: Maximum % error of the analytical model when attempting to model heat flow in increasingly high hydraulic conductivities, ranging from $9.8x10^{-9}$ to $4.9x10^{-3}$ m/s with measurements taken 1m from the borehole heat exchanger at its midpoint. 52

Figure 29: Conceptual model of the diagonal flow scenario created to compare flow scenarios in the numerical and analytical models. Blue dotted lines indicate the simulated well screens used to induce flow. 53

Figure 30: Cross-sectional top view at depth z=8.75m of an exaggerated example (not used for the model) of a pressure gradient induced from injection in the bottom left, and pumping in the top right, to create diagonal groundwater flow through the highlighted area of interest. 55

Figure 31: Cross-sectional top view of temperature (°C) at depth z=8.75 of the numerical flow model. A) T=10 day; B) T=360 days; C) T=390 Days; D) T=668 days. 57

Figure 32: Cross-sectional top view of temperature (°C) at depth z=8.75 in the analytical flow model. A) T=10 day; B) T=360 days; C) T=390 Days; D) T=668 days. 58

Figure 33: Comparison of temperature over time observed in the analytical flow model and numerical flow model. Observation points at depth z=8.75m and distances 1.41, 2.83, and 7.07m from the heater. 59

Figure 34: Simplified map of the CDOT site and coordinates of observation wells and borehole heat exchangers (BHEs) used for modeling. 61

Figure 35: Monthly heat flow rates used to simulate seasonal heat flow in the multi-borehole models. 63

Figure 36: Top-down view of the multi-borehole numerical model at a depth of 7.75 meters. T= 3 years. 64

Figure 37: Top-down sliced plane view of the multi-borehole analytical model temperature at a depth of z=7.75. T = 3 years. 65

Figure 38: Cross-sectional side view of the multi-borehole numerical model temperature at y=1. T = 2 years. (Temperature appears pronounced where the cross-section intersects BHE4 and not the other boreholes, which are offset.)..... 66

Figure 39: Cross-sectional side view of the multi-borehole numerical model temperature at y=1. T = 3 year created using the analytical model. (Temperature appears pronounced where the cross-section intersects BHE4 and not the other boreholes, which are offset.) 67

Figure 40: Comparison of temperature over time in the analytical multi-borehole model and saturated numerical multi-borehole model (expected)..... 68

Figure 41: Comparison of the temperature over time of the analytical multi-borehole model and the numerical multi-borehole model with 5m vadose zone. 69

Figure 42: Comparison of thermal plume contours viewd in a side cross-section of the heat plume created by the analytical model assuming homogenous conditions A) and the numerical model B) with a vadose zone directly above the borehole heater, represented by the red lines..... 71

Figure 43: Maximum % error of the analytical model when attempting to model heat flow in increasingly high hydraulic conductivities, ranging from $9.8x10^{-9}$ to $4.9x10^{-3}$ m/s with measurements taken 1m from the borehole heat exchanger at its midpoint. 72

Figure 43: A map of the CDOT TISR site installed by Arcadis. Red dots mark monitoring wells while blue stars indicate borehole heat exchanger placement..... **Error! Bookmark not defined.**

Figure 44: Observed increase in temperature over the ambient subsurface temperature at the CDOT site. 76

Figure 45: The average daily rate of heat flow from a single borehole at the CDOT site calculated from observed data (when available) and a smoothed monthly heat flow rate (in red) used for modeling purposes. 78

Figure 46: Monthly average heat flow rates (per borehole) used to operate the CDOT site model calculated from solar insolation. 79

Figure 47: Graphical user interface of the TISR modeling tool exhibiting parameters used to model the CDOT site analytically. 81

Figure 48: Comparison of temperature over time predicted by the analytical model using calculated heat flow from the CDOT site versus actual observed temperatures. Temperatures taken at z=7.75m depth. 83

Figure 49: Comparison of the temperature over time predicted by the analytical model using estimated heat flow using the solar insolation heat flow calculator versus actual observed temperatures at the CDOT site. 85

Figure 50: Normalized RMSEs comparing modeled temperatures of the two CDOT models versus the actual observed temperatures from the CDOT site. 87

Figure 51: Measured increases in temperature at the Mexico Site after TISR system installation. 90

Figure 52: A map of the Mexico site layout. Borehole heat exchangers are represented as red dots, while blue dots represent the thermocouples. 91

Figure 53: Monthly average heat flow rates (per borehole) used to calculate the heat flow in the Mexico Site model. 93

Figure 54: Comparison of the temperature over time predicted by the analytical model versus actual observed temperatures at the Mexico Site. Temperatures were taken at z=5m depth. 94

TABLES

Table 1: Aquifer properties used by the single borehole saturated analytical model and single borehole saturated numerical model. 35

Table 2: Aquifer properties used by the analytical model and paired unsaturated numerical models. 44

Table 3: Properties used by the partially saturated numerical models with a high permeability. 50

Table 4: Aquifer properties used by the analytical and numerical models with groundwater flow. 54

Table 5: Aquifer properties used by the analytical multi-borehole model and numerical multi-borehole model. 62

Table 6: Aquifer properties used by the analytical model to simulate the CDOT site. 80

Table 7: Coordinate system used to model the CDOT Site, map of the CDOT site can be seen in Figure 42. 80

Table 8: Coordinate system and aquifer properties used to construct the Mexico Site model. 92

1. INTRODUCTION

Groundwater is the largest reserve of accessible freshwater in the United States, playing a tremendous role in agricultural irrigation and drinking water (Stephens Et al., 2020). Moreover, groundwater discharge influences the majority of surface water (Roy & Bickerton, 2012). With access to potable water in the United States contingent on the quality of our aquifers, contamination in the subsurface is of primary concern and increasingly crucial as fresh water becomes a scarcer resource (Kummu, Et al., 2016). Developing modeling tools to optimize efficient cleanup of groundwater pollution is paramount to protecting humanity's freshwater resources. In this project, an analytical modeling tool was developed to expedite the installation and efficiency of solar thermal remediation systems, furthering this goal of providing clean groundwater.

Some of the most common groundwater pollutants are volatile organic contaminants (VOCs) originating from non-aqueous phase liquids (NAPLs) derived from petroleum products and solvents and cleaners for domestic and industrial purposes. NAPLs are immiscible liquids, many of which slowly degrade in the subsurface (Huling, 1991). As concentrated NAPLs remain in place, they release a spreading contaminant plume of aqueous and gaseous VOCs that are hazardous to humans (Huling, 1991). VOCs and their constituents, trichloroethylene (TCE), dichloroethylene, and vinyl chloride, for example, can contaminate large volumes of aquifers, requiring expensive water treatment (Guha Et al., 2012).

When NAPL contaminants release into the environment through a spill, leak, or improper disposal, they flow downwards to the groundwater table through the vadose zone (Huling, 1991). Liquid NAPL stays relatively immobile horizontally in the subsurface, traveling primarily due to density-driven flow or vapor migration instead of advection (Huling, 1991). The two categories of NAPLs, dense or light non-aqueous phase liquids, are split by relative density because of their differing behavior once they interact with the water table. Dense non-aqueous phase liquids (DNAPLs) such as TCE sink below the water table. Light non-aqueous phase liquids (LNAPLs), such as benzene, toluene, ethylene, and xylene, are less dense than water and perch on top of the water table, becoming smeared throughout the capillary fringe due to fluctuating water table levels (Huling, 1991).

The multiphase transport and storage of VOCs make monitoring and addressing groundwater contamination a complex topic. Once in the subsurface, NAPLs may occupy four states in a process known as multiphase mass partitioning (Washington, 1996). NAPLs remain a liquid that stays in pore space or dissolves and adsorbs into the matrix of the aquifer material, partitioning to the solid (adsorption), partitioning as gas vapor, or partitioning in small concentrations as an aqueous form (Mcdade Et al., 2005). Aqueous phase VOCs such as TCE solubilize at low concentrations from liquid NAPL that is in contact with groundwater, releasing a contaminant plume that flows far distances in the subsurface (Rivett Et al., 2011). Groundwater contaminant plumes discharge into wells and surface water, posing a significant environmental hazard (Rivett, Et al., 2011). Initially, the connection between VOCs and adverse health effects went unnoticed,

famously highlighted in the 1980 Woburn trichloroethylene contamination suits (Heneghan, 2000). Seemingly harmless at the time, NAPL chemicals were stored in leaking tanks and even deliberately dumped into streams and pits across the country. Before being recognized as an issue, sweeping contamination plumes from NAPLs were allowed to spread for decades. Sixty percent of Superfund sites, contaminated areas deemed by the EPA as a national priority, are TCE contamination sites (Heneghan, 2000). Superfund sites may originate from large-scale sources, such as the Marine Corps Base Camp Lejeune, while other equally hazardous sites could be small point sources, such as dry cleaners or auto repair shops (Huling, 1991). Despite the ubiquitous issue of NAPL contamination across the country, remediating these sites remains complex and prohibitively expensive.

Initially, NAPL contamination was addressed with a pump and treat remediation method to remove liquid NAPL and hydraulically contain contaminant plumes (Mackay & Cherry, 1989.) The general belief was that with enough pumping and dilution, even residual NAPL could eventually be drawn out, with permeable reactive barriers used to limit plume spread as well. Both of these methods prevented further contamination spread but ultimately proved ineffective in eliminating the source of the NAPL contaminants. Despite pumping and natural attenuation, base levels of VOCs continued to release from contaminated aquifers at a harmful level with a long half-life that made natural attenuation insufficient in most time scales (Doty & Travis, 1990). Eventually, it was discovered that aquifer materials retain dissolved NAPLs in low permeability matrixes and continue to release a contaminant plume despite years of pumping and

removal of the source NAPL, a process known as "matrix diffusion" (Seyadabbasi et al., 2012). Furthermore, the pumping and treatment of contaminated water for decades is too expensive and logistically demanding to function as a permanent solution in many cases. Due to matrix diffusion, fueled by strong, diffusive forces, costly and intense remediation methods beyond pumping are used to eliminate NAPL contamination from aquifers.

Air sparging, enhanced bioremediation, chemical oxidation, surfactant flushing, and thermal treatment are active in-situ remediation solutions to VOC contamination. These methods address contamination at the source, known as source depletion, unlike pump-and-treat or permeable reactive barriers. Negative factors considered when implementing in-situ treatment are the cost of infrastructure, energy usage, capital costs, and storage and treatment of generated waste material. The median NAPL remediation project costs $440,000, with large projects quickly reaching the multimillion-dollar range (McDade et al., 2005). Air sparging, enhanced bioremediation, chemical oxidation, and surfactant flushing require an understanding of the aquifer before they pump and inject into the aquifer. Creating a detailed cross-section of the aquifer and a detailed groundwater model to predict remediation performance is often necessary and sometimes a deterrent when planning these systems (Rahbeb & Mohtar, 2007).

Meanwhile, traditional thermal remediation methods rely on heating the aquifer material to remove VOC contaminants through volatilization. Heating the subsurface to high temperatures demands new power delivery infrastructure and incurs high energy costs (McDade et al., 2012).

The model in this project focuses on modeling low temperature, less than 100 degrees C, thermal borehole heat exchangers powered using solar energy. Modeling these systems is, in some manners, easier than modeling groundwater flow. The thermal conductivity of aquifer materials is relatively uniform regardless of grain size and substrate, allowing for straightforward thermal modeling compared to groundwater modeling (Ferguson, 2007). In contrast, an aquifer's permeability and other hydraulic characteristics vary in order of magnitude, making installing non-thermal remediation systems more complex.

In low-temperature thermal remediations systems, heat primarily spreads through heat conduction in the subsurface from a grouted coil of transfer fluid (Molina et al., 2011). The spread of heat is dictated by the thermal conductivity of the aquifer material itself, referred to as λ_{dry}, or a combination of the aquifer material and water in the pore voids, referred to as λ_{wet}. Heat may also travel in the form of advective flow, moving with the flow of groundwater. In scenarios of high hydraulic conductivity, natural convection, flow due to the buoyancy of heated water may occur.

The thermal conductivity of various aquifer materials has been well documented in databases for ground source heat pump usage, with the natural ranges of λ_{wet} varying from 0.5 to 8 W/m°C in extreme cases with values most often staying in the range of 1.5 to 4 W/m°C with an average of 2.5 W/m°C (Dalla et al., 2020).

1.1 Characteristics of Analytical Versus Numerical Models

Models function as vital tools in identifying the most efficient usage of remediation systems by projecting potential outcomes and optimizing designs, allowing for better contaminant cleanup and efficient use of capital. The objective of this project was to produce an analytical modeling tool that can be used to quickly and easily design solar borehole heat exchanger systems while remaining accurate.

When choosing modeling software, one must decide to use a fast and user-friendly program or sacrifice ease of use and speed for a computationally intense but more accurate system (Conceicao, 2002). Simplified groundwater models are typically based on analytical solutions, while more detailed models use numerical solutions based on a finite difference or finite element approach. Because of ease of use and quick processing times, the borehole heat exchanger modeling solution developed in this project was of an analytical nature.

Analytical models use closed-form analytical functions that represent natural processes such as heat transfer, advective flow, or diffusive processes. These functions are based on variables determined from user inputs such as energy flux, aquifer material properties, and simple boundary conditions (Anderson et al., 2015). Using analytical methods, a groundwater model typically generalizes the subsurface, overlooking heterogeneities, such as low permeability clay lenses or fracture flow, and struggle to capture complex 3-dimensional processes (Freeze & Witherspoon, 1966). Analytical models are flexible and quick tools for modeling large quantities of locations or multiple scenarios while applicable in most scenarios with generalizations (Zipper, et al., 2019).

REMChlor (Remediation Evaluation Model for Chlorinated Solvents) is a widely used example of an analytical solution for modeling groundwater remediation of VOCs (Falta, 2007). As a simplified analytical model, REMChlor is fast to use for designing various outcomes, beneficial for testing and optimizing remediation strategies. The limitations of REMChlor, characteristic of analytical groundwater models, are that one must assume the groundwater flow field is uniform in one direction and that the subsurface is homogeneous in composition (Falta, 2007). Analytical models become increasingly complex to create while based on closed-form functions as more conditions and variables are introduced. Analytical models give way to numerical models that are better suited for modeling increasingly complex scenarios (Freeze & Witherspoon, 1966).

Numerical models allow for more detailed simulations by dividing groundwater processes into finite volumes. These multiple small units are used to develop a system of simultaneous algebraic equations. The discretized approach used in numerical modeling interlinks equations in multiple dimensions and time. Properties of an aquifer are stored in arrays that combine to create a conceptual groundwater model formed from a system of discretized equations. The simultaneous equations are solved relative to each other over discretized time steps until the desired result is obtained (Freeze and Witherspoon, 1966). The individually adjustable elements, characteristic of a numerical model, allow for granular characterization of an aquifer heterogeneity that would be difficult or impossible to account for in analytical models.

The suite of TOUGH codes are numerical solutions used to simulate multiphase flow and heat transfer, developed initially in the 1980s at the Lawrence Berkeley

National Laboratory (Pruess, 1988). They have the capacity to account for multiphase fluid flows in fractured and porous mediums while accounting for sorption, dissolution, phase changes, heat convection and conduction, and many other variables. Modern variations of the TOUGH codes can simulate contamination transport with multiple phase changes and degradation (Jung et al., 2017). The ability to model complex non-isothermal flow of various types in heterogeneous systems is a strength of numerical models.

When designing numerical models, the operator manually determines the grid spacing. Poorly designed anisotropic grids, grids diagonal to flow, or large grid sizes may yield inaccurate results as they influence the discretized equation used in simulations (Krakauer et al., 2014). As numerical groundwater models become increasingly refined for the sake of accuracy, the number of required calculations increases exponentially as well. A multiphase model of a large contamination site over decades discretized into small elements could be demanding to run on an ordinary computer. Teaching people to use numerical modeling software is difficult. Testing multiple remediation system layouts can be time-consuming in the planning phase and nearly impossible in the field. While models represent real-world scenarios, they are only as precise as their inputs and assumptions (Anderson et al., 2015). A highly refined numerical groundwater model made without subsurface observations is still an inaccurate model. Locations without previous research, such as prospective contamination remediation sites, may be simpler to model using analytical methods.

1.2 Thermal In-Situ Remediation

This research project was done in conjunction with Arcadis, centered around planning and installing Thermal In-Situ Remediation systems (TISR™, U.S. patent number 10,384,246 & 10,688,545) for environmental remediation. The modeling tool for solar-powered borehole heat exchangers created in this project will be publicly available.

TISR systems are a supplemental subsurface remediation strategy that boosts the productivity of remediation systems by adding heat to the aquifer. TISR systems use arrays of low-temperature borehole heat exchangers (BHEs) heated with solar energy using evacuated tube collectors or flat panel collector units. Pumps with controllers circulate a hot working fluid as necessary to reach a desired subsurface heating temperature for remediation (Figure 1).

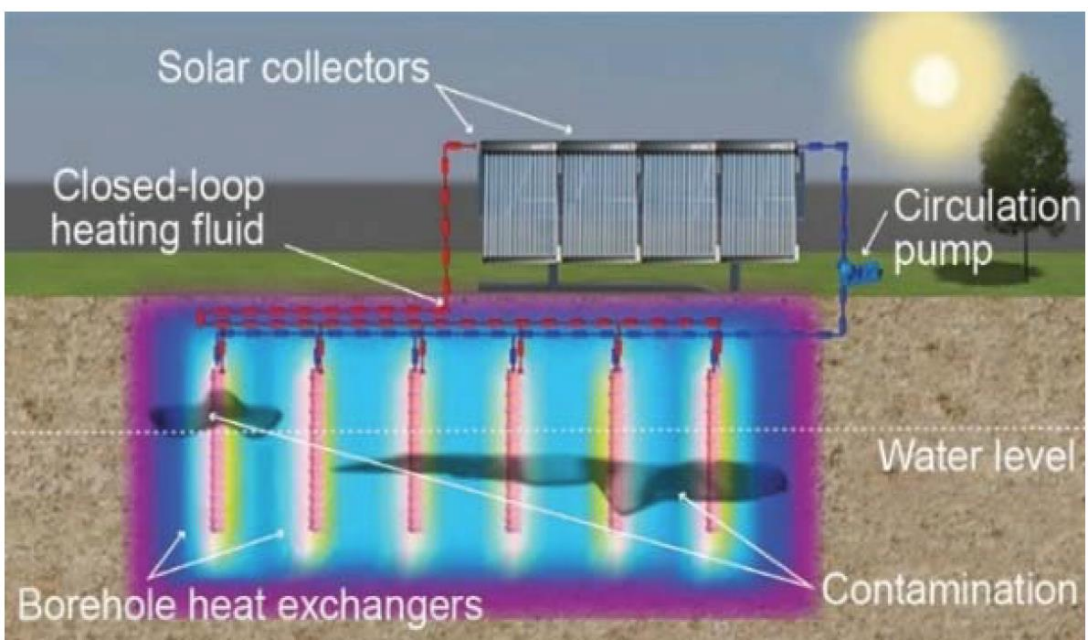

Figure 1: Diagram of a Thermal In-Situ Remediation system (TISR™). Permission for use granted by Randhawa Davinder, Arcadis (Divine, 2020).

The borehole heat exchanger loop is filled with a 50% propylene glycol, 50% water working fluid that transfers heat to the surrounding aquifer via coiled metal tubing grouted into 8" boreholes (Randahawa, Personal Communication, September 2020). The heat from the borehole heat exchanger system then travels through the closed-loop system and is imparted to the subsurface via thermal conduction, where it spreads throughout the subsurface (Florides & Kalogirou, 2007).

Using solar energy, low-temperature borehole heat exchangers in TISR systems can increase the subsurface temperature from ten to sixty degrees Celsius, increasing the rate of VOC removal or increasing natural attenuation (Randahawa, Personal communication, September 2020). An example of this is visible at the CDOT TISR site where bi-products of vinyl chloride reduction and TCE attenuation were visible after TISR system implementation (Figure 2).

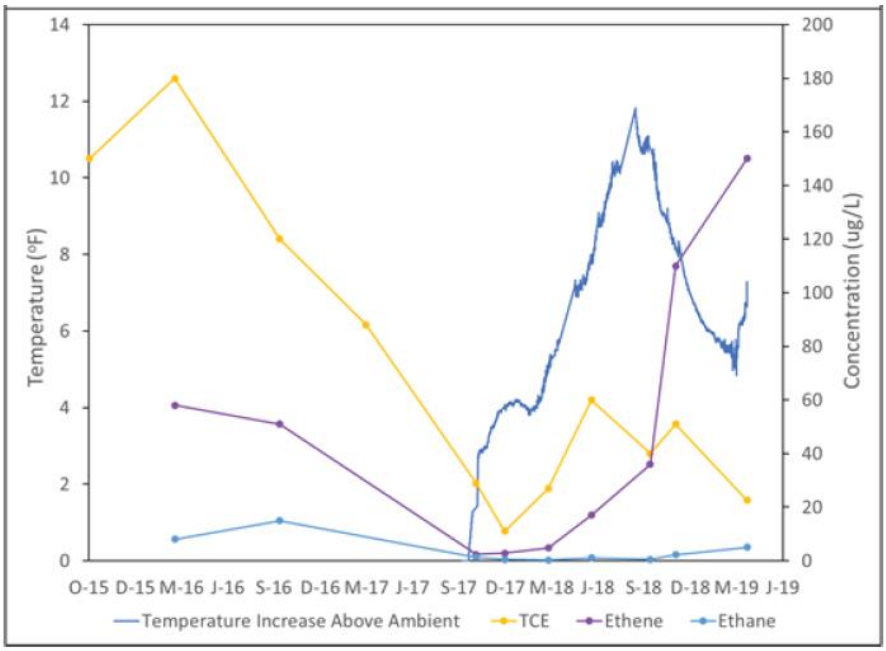

Figure 2: The relation of moderate subsurface temperature increase from a TISR system to elimination of TCE and increase in constituents of Vinyl Chloride reduction (Divine, 2020).

A 20-degree Celsius temperature increase can boost the microbial activity of dechlorinating bacteria, increasing the removal rate of VOCs in biodegradation remediation systems at least four-fold (Macbeth et al., 2012). Moderate temperature increases, such as the changes observed from TISR borehole heat exchangers, were shown to double the Henry's constant of most VOCs (Chen t al., 2012). With higher volatility, VOC removal via air sparging and soil vapor extraction systems improves. Increasing temperatures over ambient levels may also improve extraction efficiency and natural attenuation due to decreased contaminant viscosity and increased solubility.

TISR systems have been installed in various locations, with a pilot study at the Colorado Department of Transportation (CDOT) site that has been operating since 2018

(Personal Communication, Randhawa, September 2020). Once implemented as a supplemental aid to various methods, the reduced time of remediation afforded by a TISR system quickly outweighs the cost of a TISR system (Divine, 2020).

The CDOT TISR system in Denver, Colorado, was installed to increase the soil temperature with a target of 5-10 °C to aid an enhanced in situ bioremediation system for reducing TCE and petroleum distillates (Divine, 2020). Moderate temperature increases from borehole heat exchangers, such as with the CDOT site, have been shown to accelerate VOC remediation (Figure 2). The TISR system installation costs were approximately 200,000 dollars, representing a payback time in less than one year after reducing the expected remediation time in half (Figure 3). The projected net savings from installing a TISR system at the CDOT site is 500,000 dollars (Divine, 2020).

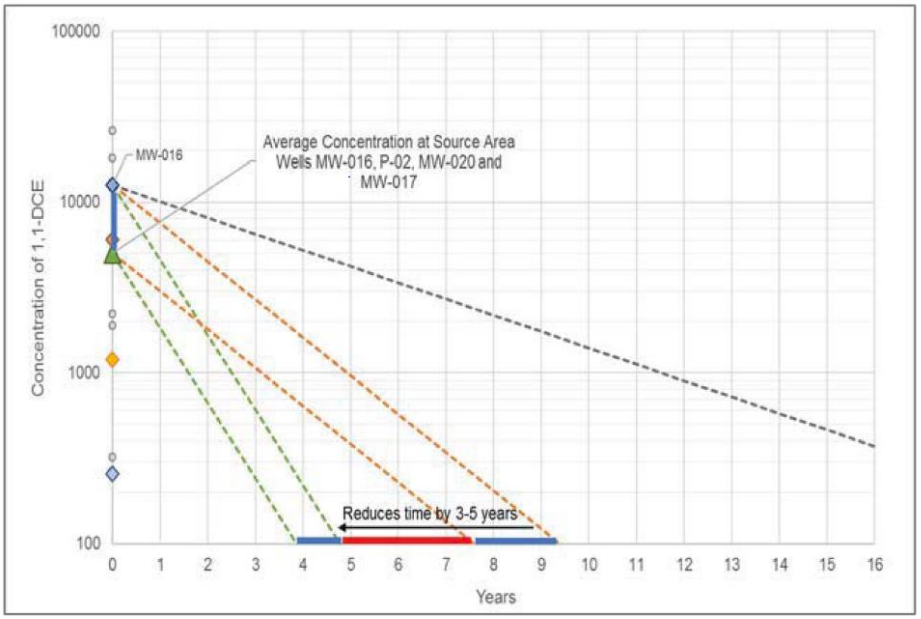

Figure 3: Reduction in the active remediation time of TCE, based on standard biologically enhanced treatment, represented by the orange lines, versus the anticipated TISR-enhanced rate of treatment, versus the expected natural attenuation rate of removal, in grey at the CDOT site (Divine, 2020).

Modeling the heat propagation of borehole heat exchangers in a TISR system is relatively simple, relying on relatively uniform thermal properties rather than hydraulic ones. An analytical model is well-suited for quickly modeling and proposing potential system designs.

2. RESEARCH OBJECTIVES

The main goal of this study was to develop and validate a simplified analytical model for solar powered borehole heat exchangers for use in planning remediation sites quickly and accurately. The specific objectives are to:

- Create an analytical solution and interface to easily model borehole heat exchanger arrays in 3 dimensions with variable heat flow and groundwater flow.
- Verify the analytical solution as valid by showing it performs similarly to the more complex, recognized, TOUGH EOS1 and EOS3 modeling codes.
- Assess the limitations of the analytical solution, which makes the simplifying assumption that the aquifer modeled is homogenous by comparing it to variably saturated numerical models created with TOUGH EOS3.
- Use the analytical solution to model field sites in order to assess the accuracy of the TISR modeling tool to observe data from the real world.

3. DEVELOPING AN ANALYTICAL SOLUTION FOR LOW-TEMPERATURE BOREHOLE HEAT EXCHANGERS (TISR MODELING TOOL)

3.1 Background

As part of the ESTCP project ER20-5028, a modeling tool for TISR installation was developed. The model has a graphical user interface in Microsoft Excel for inputs and is coded in visual basic, modifying a solution given by Molina et al. (2011). The new solution was adapted to be more relevant for environmental modeling of borehole heat exchangers with additions as follows:

- The ability to define boreholes situated below surface level (z=0) with a defined interval length.
- The ability to model simple groundwater flow in a chosen compass direction.
- Superposition of temperature in space to allow for multiple borehole heat exchangers to be modeled at once.
- Superposition of a transient heat flow rate from borehole heat exchangers over time.

3.2 Current Analytical Solutions for Borehole Heat Exchangers

A solution from Molina et al. (2011) designed for ground source heat pumps was adapted to create a low-temperature borehole heat exchanger modeling solution. With this newly proposed solution, groundwater flow and the finite geometry of a borehole heat exchanger are accounted for, allowing the new borehole heat exchanger modeling

program to perform more detailed tasks that would normally be done with a numerical model.

A standard equation for modeling two-dimensional heat transfer in the subsurface through a porous medium with groundwater flow, used for ground source heat pump calculation, would be expressed as in equation 1 (Molina et al., 2011). T as the temperature in degrees C, t as time in seconds, V_d representing Darcy velocity in m/s in the x-direction, ρ_{w} as the density of water and ρ as the density of the aquifer material in kg/m^3, C_{w} as the specific heat capacity of water and C as the specific heat capacity of the aquifer material in kJ/kg°C, and λ as the thermal conductivity of the aquifer material in W/m°C with x and y cartesian coordinates in meters.

$$\rho C \frac{\partial T}{\partial t} + V_d \rho_{\mathrm{w}} C_{\mathrm{w}} \frac{\partial T}{\partial x} - \lambda \left(\frac{\partial^2 T}{\partial x^2} + \frac{\partial^2 T}{\partial y^2} \right) = 0 \qquad (1)$$

The following solution in equation (2) is for a single line source heater with a specified heating rate, q_L, defined in Eksilon, 1987. Variable v_{t} is the linear heat transport velocity from advection m/s while q_{L} is the heat flow rate per unit length of the borehole (W/m). Variable ψ is an integration parameter, and α is the thermal diffusivity of the subsurface in m^2/s.

$$T - T_0 = \frac{q_{\mathrm{L}}}{4\pi\lambda} \exp\left[\frac{v_T x}{2\alpha}\right] \int_0^{\frac{v_T^2 t}{4\alpha}} \frac{1}{\psi} exp\left[-\psi - \frac{v_T^2 (x^2+y^2)}{16\alpha^2 \psi}\right] d\psi \qquad (2)$$

In which:

$$v_{\mathrm{T}} = V_d \rho_{\mathrm{w}} C_{\mathrm{w}} / \rho C$$

$$\rho C = \phi \rho_{\mathrm{w}} C_{\mathrm{w}} + (1 - \phi) \rho_{\mathrm{R}} C_{\mathrm{R}}$$

Where ρ_{R} is the rock grain density and C_{R} is the rock grain heat capacity. In these solutions, an infinite line source of heat on a z coordinate represents the borehole heat exchanger. This solution was historically designed for transient thermal borehole energy propagation over a short time interval (Phillipe et al., 2009). An issue with using analytical modeling solutions that rely on infinite line heat sources is that they do not account for vertical heat flow (Man et al., 2010). In a short-term model, vertical flow may not be of concern, but it becomes a more significant mode of heat propagation in long-term models, such as thermal remediation projects designed to reduce subsurface contamination over multi-year spans.

Molina et al. (2011) developed a 3-dimensional version of the solution shown in equation 2 for a finite length heater which is more appropriate for long-term borehole heat exchanger modeling. This solution is relatively new and allows the borehole heat exchanger model to be more accurate than the 2-dimensional conduction model given in equations 1 and 2. The ability to model heat flow vertically is essential for borehole heat exchanger systems like the ones used at the CDOT site with heating elements installed from only 5 to 10m depth, for example. Using a solution in 3-dimensions also allows for temperature observations at specific coordinates and depth, which is crucial in predicting if the heat would properly reach a specific depth of contaminant, such as a NAPL plume.

3.3 Variable Line Source for Borehole Heat Exchangers

In this project, the solution for heat propagation from a finite line source used in Molina et al. (2011) was adapted and expanded upon for use in borehole heat exchanger modeling. It was shown previously that the single borehole analytical solution from Molina et al. (2011) was accurate when compared using paired 20-year heat flow models, matching results from numerical models created in FEFLOW closely (Molina et al., 2011).

The new analytical solution for modeling borehole heat exchangers developed in this project is fundamentally based on equation 3 where variable ϕ is the void porosity, C_R is the specific heat capacity of the rock and ρ_R is the density of the rock. The following partial differential equation allows for transient heat conduction with convection due to groundwater flow in three dimensions with x, y, and z as cartesian coordinates in meters:

$$[\phi\rho_w C_w + (1-\phi)C_R\rho_R]\frac{\partial T}{\partial t} = -V_d\rho_w C_w\frac{\partial T}{\partial x} + \lambda\frac{\partial^2 T}{\partial x^2} + \lambda\frac{\partial^2 T}{\partial y^2} + \lambda\frac{\partial^2 T}{\partial z^2} \quad (3)$$

Assumptions made by this analytical solution are that the hydraulic properties of the aquifer are homogenous and that groundwater flow direction is constant. While it is assumed that convection from density-driven flow does not occur in this solution, it is accepted to play a minor role in heat flow processes in low permeability subsurfaces (Hecht-Mendez et al., 2010). The new solution treats a heater as a continuous line source of heat of Q watts over a vertical thickness extending from a denoted range of *a* to a depth of *b* in meters to better reflect the nature of a borehole heat exchanger buried along

a specific interval at a location of x_0, y_0. The initial subsurface temperature is T_0 and the ground surface is maintained at T_0.The solution to equation 3 with these conditions in a system that is infinitely deep is:

$$T = T_0 + \frac{Q}{2\pi\lambda(b-a)} \exp\left\{\frac{v_T x}{2\alpha}\right\} \left[\int_a^b f(x,y,z,t)dz' - \int_{-b}^{-a} f(x,y,z,t)dz'\right] \quad (4)$$

Where:

$$r = \sqrt{(x-x_0)^2 + (y-y_0)^2 + (z-z')^2}$$

$$\alpha = \frac{\lambda}{\phi\rho_w C_w + (1-\phi)\rho_R C_R}$$

$$v_T = \frac{V_d \rho_w C_w}{\phi\rho_w C_w + (1-\phi)\rho_R C_R}$$

The function f appearing in the integrals is defined in equation (5) with r representing the radial distance from the borehole of the observation point, in meters:

$$f(x,y,z,t) = \frac{1}{4r}\left[\exp\left(\frac{-v_T r}{2\alpha}\right) \operatorname{erfc}\left(\frac{r - v_T t}{2\sqrt{\alpha t}}\right) + \exp\left(\frac{v_T r}{2\alpha}\right) \operatorname{erfc}\left(\frac{r + v_T t}{2\sqrt{\alpha t}}\right)\right] \quad (5)$$

Equation 4 applies to define only a single borehole heat exchanger in an infinite system with the ground surface as a temperature boundary condition maintaining a constant temperature of T_0. The case of an insulated ground surface can be obtained by replacing the minus sign in front of the second integral in equation 4 with a positive sign. The integrals in equation 4 can be evaluated numerically using Gaussian Quadrature (Den Isegar, 2006).

3.4 Superposition of Multiple Borehole Heat Exchangers

The solution can be adapted for scenarios with multiple borehole heat exchangers by superimposing the changes in temperature resulting from heat sources. This is done by stacking the sum temperature change from each borehole heat exchanger at the specified well locations. For a system consisting of *nheater*, representing the total number of heaters, the composite solution appears as equation 6:

$$T = T_0 + \sum_{m=1}^{\text{nheater}} \left\{ \frac{Q_m}{2\pi\lambda(b_m - a_m)} \exp\left\{\frac{v_T x}{2\alpha}\right\} \left[\int_{a_m}^{b_m} f_m(x,y,z,t)dz' - \int_{-b_m}^{-a_m} f_m(x,y,z,t)dz' \right] \right\} \quad (6)$$

Where Q_m is the heat input in watts to heater number "*m*" and a_m, and b_m are the top and bottom depths of each heater and

$$r_m = \sqrt{(x - x_{0m})^2 + (y - y_{0m})^2 + (z - z')^2}$$

Variables x_{om} and y_{om} are the coordinates of the heaters used to determine distance relative to the heater r_m, with the updated function shown as:

$$f_m(x,y,z,t) = \frac{1}{4r_m}\left[\exp\left(\frac{-v_T r_m}{2\alpha}\right)\operatorname{erfc}\left(\frac{r_m - v_T t}{2\sqrt{\alpha t}}\right) + \exp\left(\frac{v_T r_m}{2\alpha}\right)\operatorname{erfc}\left(\frac{r_m + v_T t}{2\sqrt{\alpha t}}\right)\right] \quad (7)$$

At this stage, the equation 6 solution is still assuming a constant thermal power input from the borehole heat exchangers over time.

3.5 Variable Heat Flow over Transient Time Periods

For a variable change in borehole heating rate, values of heat flow delivered by the borehole, Q_m , is broken into time steps of Q_{mn} where n is the number of heating periods, for example Q_{m0} , Q_{m1} , Q_{m2}. The variable t_n is the starting time of the heater period n and $\Delta Q_{mn} = (Q_{mn} - Q_{mn-1})$. The updated equation appears as:

$$T = T_0 + \sum_{n=0}^{ntimes} \sum_{m=1}^{nheater} \left\{ \frac{\Delta Q_{mn}}{2\pi\lambda(b_m - a_m)} exp\left(\frac{V_t x}{2\alpha}\right) \left[\int_{a_m}^{b_m} f_m\,(x, y, z, (t - t_n)) - \int_{-b_m}^{-a_m} f_m(x, y, z, (t - t_n))dz' \right] \right\} \quad (8)$$

3.6 Accounting for Partially Saturated Conditions

The analytical modeling solution cannot directly account for partially saturated conditions since the solution assumes the subsurface is homogenous in composition. In order to compensate for the unsaturated zone, saturated water content and, therefore, thermal conductivity of the aquifer along the borehole depth is roughly estimated using the commonly available basic properties of thermal conductivity, aquifer porosity, and depth to groundwater. The method used for a simple estimate of capillary action and water saturation is further explored in Hird (2017) and Lie et al. (2014) “An approach for quick estimation of maximum height of capillary rise” .

The average thermal conductivity λ_{sa}, used by the analytical model is interpolated from the average volumetric water content, S_{wa}, and the known wet (λ_{wet}) and dry (λ_{dry}) thermal conductivity of the aquifer in W/m°C using the following equation:

$$\lambda_{sa} = \lambda_{dry} + \sqrt{S_{wa}} \cdot (\lambda_{wet} - \lambda_{dry}) \quad (10)$$

The average volumetric water content, S_{wa}, is determined using equation 11, where the water content is determined along the top a and bottom b depth of the borehole heater:

$$S_{wa} = \frac{1}{(b-a)} \int_a^b f(z)dz \tag{11}$$

S_w is a assumed to be a simplified function depth z, in meters, where h_{cd} is the calculated depth to capillary fringe from the surface, W_t is the known depth to groundwater and S_{wr} is the volumetric soil water residual saturation of the aquifer material:

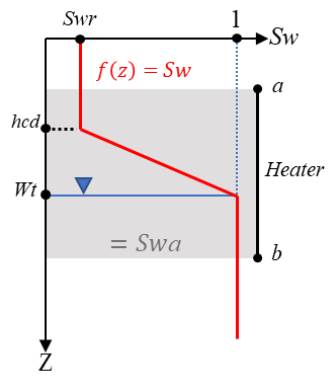

$$0 \leq z < h_{cd}: S_w = S_{wr}$$

$$h_{cd} \leq z < W_t: S_w = \frac{(1 - S_{wr})}{(W_t - h_{cd})} z - \frac{(1 - S_{wr})}{(W_t - h_{cd})} h_{cd} + S_{wr}$$

$$W_t \leq z < \infty: S_w = 1$$

The maximum capillary rise, h_c in mm, is determined using the Young-Laplace equation for capillary rise (Hird & Bolton, 2017) where water at 20 °C is defined with a density of ρ_w=1000 kg/m^3, surface tension of σ=72.75 mN/m, d_{mm} as the d_{10} of the aquifer in mm, g as the gravitational constant, and full wettability assumed, giving a wetting phase contact angle of α = 0.

$$h_c = \frac{4\sigma cos\alpha}{d_{mm}\rho_w g}$$

Where

$$h_{cd} = W_t - h_c$$

The d_{10} can be estimated from hydraulic conductivity when unavailable using the Kozeny-Carman equation, a more accurate solution for low to high permeability materials compared to the older Hazen solution (Carrier, 2003). K is hydraulic conductivity in m/s, and volumetric porosity is defined as ϕ, and d_m is defined as the d_{10} in units of meters. Constant v is the kinematic velocity of water, assumed to be 1mm^2/s, and C is the Kozeny-Carman constant of 1/180.

$$K = C\frac{g}{v}\frac{\phi^3}{v(1-\phi)^2}{d_m}^2$$

3.7 Solution for Adjusting Groundwater Flow Direction

While this solution applies the groundwater flow direction along the positive x-axis, it is possible to adjust the groundwater flow direction in any direction using a simple transform solution (equation 12). The coordinates can be translated from the original inputs to a new system of x' and y' to be used in the analytical modeling solution in chapter 3.5. Angle θ is the change in degrees counter-clockwise relative to the positive x-axis, east in map coordinates, necessary to obtain the desired flow direction orientation. Coordinates y and x refer to the original coordinates that were input to define boreholes and observation points, while y' and x' are the new coordinates used in the analytical calculations.

$$x' = x\,cos(\theta) + y\,sin(\theta)\,, \quad y' = -x\,sin(\theta) + y\,cos(\theta) \tag{12}$$

After the thermal borehole calculations are made, the coordinates are reversed back to their original coordinate system using the inverse transform equation 13 for ease of use.

$$x = x'cos(\theta) + y'sin(\theta)\,, \quad y = -x'sin(\theta) + y'cos(\theta) \tag{13}$$

A conceptual diagram visualizing the coordinate change is shown in Figure 4.

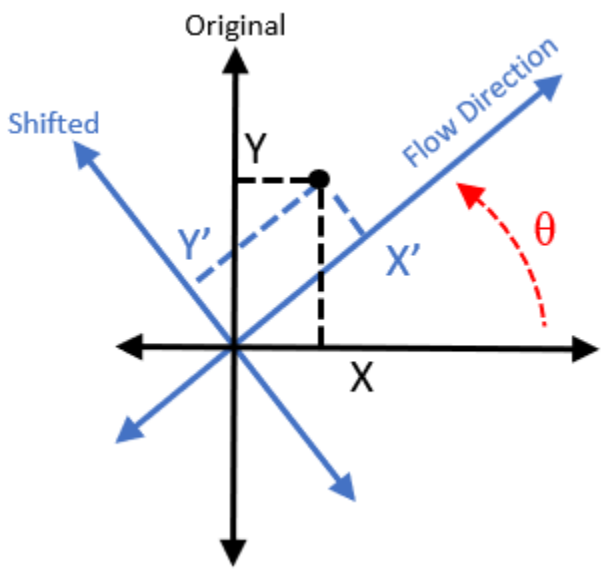

Figure 4: Diagram of how the coordinate system in the analytical solution is rotated relative to the desired groundwater flow direction.

3.8 Modeling Tool and Interface

The new analytical solution for modeling multiple borehole heat exchangers with finite geometry and groundwater flow, shown in equation 8, was coded with Visual Basic into an easily usable program. A graphical user interface in Microsoft Excel is used to define the model properties such as thermal conductivity, groundwater flow, borehole coordinates, and temperature observation points, which are input into the Excel interface

pictured in Figure 5. In this project, “An updated ground thermal properties database for GSHP applications” by Dalla et al. (2020) was a useful resource in estimating the thermal conductivities of various subsurface materials for use with the modeling tool.

3D Analytical solution for borehole heat exchanger with regional GW flow								1095	
Ron Falta 2/14/2021	Run Program				heater		N obs loc	3	
Darcy velocity	5	m/yr	month	months	Q (Watts)		xobs	yobs	zobs
number of heaters	1	unitless	January	1	0		1	1	6.25
Background T	0	C	February	2	200		2	2	6.25
porosity	0.01	unitless	March	3	200		5	5	6.25
Rock heat capacity	1000	J/kg*C	April	4	200				
Rock grain density	2650	kg/m^3	May	5	200				
Thermal conductivity	2.5	W/m*C	June	6	200				
Heater length	5	m	July	7	200				
depth to top of heater	5	m	August	8	200				
Snapshot flag yes=1, no=-1	1.0		Septembe	9	200				
xmin	-25	m	October	10	200				
xmax	25	m	November	11	200				
ymax	15	m	December	12	200				
ymin	-25	m	January	13	200				
dx	1	m	February	14	0				
dy	1	m	March	15	0				
z for xy plot	9	m	April	16	0				
y for xz plot	0	m	May	17	0				
zmin	0	m	June	18	0				
zmax	-20	m	July	19	0				
dz	1	m	August	20	0				
N Gauss (integration)	16		Septembe	21	0				
Flow direction angle	45	degrees	October	22	0				
t start, day of year	1	days	November	23	0				
t end, days since start	300	days	December	24	0				
delta t for time series	30	days	January	25	0				
heater data			February	26	0				
x (m)	y (m)		March	27	0				
0	0		April	28	0				
			May	29	0				
			June	30	0				
			July	31	0				

Figure 5: Example of the graphical user interface for the analytical modeling solution coded in Visual Basic.

By defining the x, y, and z dimensions of the model in the user interface (Figure 5), the analytical solution will populate a temperature contour map of the subsurface by

calculating the change in temperature relative to the boreholes at every coordinate. An example of the temperature plots produced by the analytical model, shown in Figure 6.

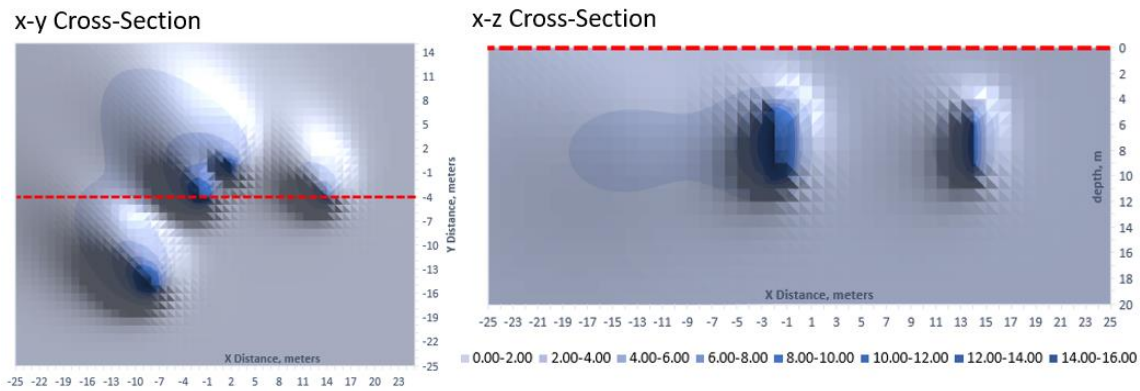

Figure 6: Example of the cross-sectional contour plots of heat using the Excel user interface. The x-y plot shows a top-down view of the model at a set depth; the x-z cross-section shows the side view of the model along a set y coordinate.

The model also calculates the change in temperature at designated observation points, set in the user interface (Figure 5), which will produce a graph of temperature change over time to be used for quantitative analysis, shown in Figure 7.

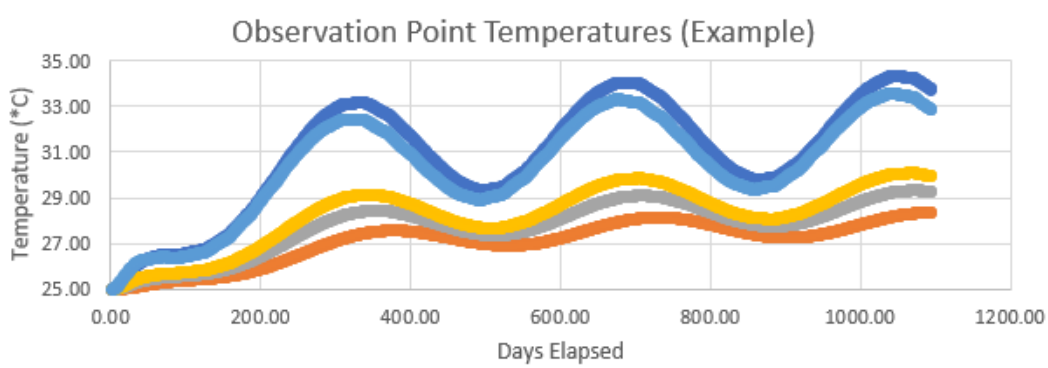

Figure 7: Example of how transient temperature is recorded by the modeling tool at observation points placed around the borehole.

The visual basic code for the model solution can be found in appendix (1).

4. CALCULATING HEAT FLOW TO BOREHOLE HEAT EXCHANGERS

4.1 Background on TISR System Functionality

TISR systems consist of multiple borehole heat exchangers used to heat the subsurface using a pump-circulated loop of working fluid heated using solar energy (Figure 8). Borehole heat exchangers in TISR systems may be stainless steel or copper coils grouted into an 8" borehole along a specified depth interval (Flanders et al., 2020). The working fluid can be pure water or a propylene glycol solution diluted to 50% water to prevent potential freezing or raise the boiling temperature. Flat plate or evacuated tube solar collectors may be used to heat TISR systems depending on the site's desired heating effects and climate. Locations with colder environments may use evacuated tube collectors for their better-insulated properties, while warmer climate sites may use flat panel solar collectors (Flanders et al., 2020). Typically, a single pump feeds all of the borehole heat exchangers, which may have their own inlet and outlet temperature monitors. The pumps in TISR systems are not operating at all times, shutting off automatically at set high and low-temperature limits depending on the desired usage of the system or to protect itself from overheating, with TISR systems targeting increases of temperature ranging from 5 to 70 °C (Flanders et al., 2020).

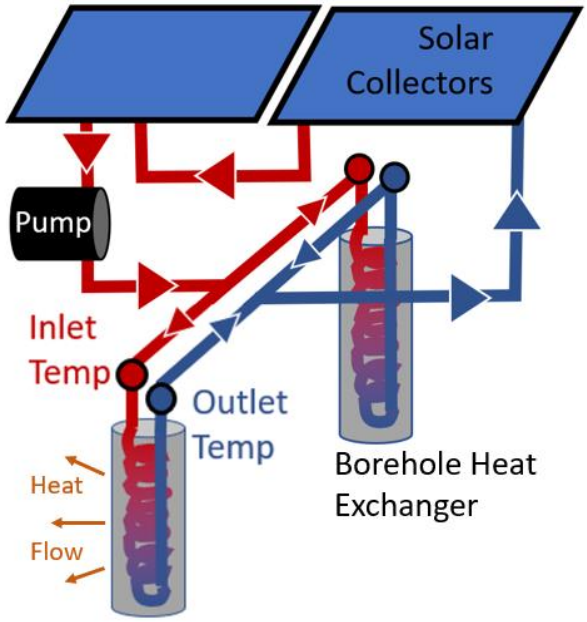

Figure 8: Simplified conceptual model of TISR^{TM} systems, used to calculate heat flow from a borehole heat exchanger using borehole inlet and outlet temperature readings.

4.2 Calculating Heat Flow From Pre-Existing Borehole Data

In order to fulfill the objective of validating the analytical model, it was necessary to calculate historical heat flow, the energy imparted to the subsurface by the borehole heat exchangers on-site, in order to simulate the scenario in the analytical model and compare it to observed values in the real world. Heat flow can be determined by assuming the temperature lost between the inlet and outlet of a borehole heat exchanger is energy being directly imparted into the soil as heat flow. Extracting this data uses a solution that requires knowledge of the pump rate, pump operating time, and specific heat capacity and density of the working fluid used in a borehole heat exchanger system.

The equation created to determine the borehole heat flow, Q_i in watts, from a borehole heat exchanger over a period of time is defined in equation 14, where Q_i is the average heat flow into the subsurface (kJ/s) while the system is actively pumping, where T_{in} -T_{out} is the change in temperature ($°C$) between the borehole heat exchanger inlet and outlet, while C_f is the specific heat capacity of the working fluid, in units of $\frac{kJ}{kg°C}$, the density of the propylene glycol water mixture is defined as ρ_f in units of kg/m^3, and the flow rate of the working fluid pumped through the borehole is defined as Q_p in units of m^3/s.

$$Q_i = (T_{in} - T_{out})Q_p\rho_f C_f \tag{14}$$

The average rate of heat flow is defined as

$$Q_a = \frac{\int_0^{time} Q_i}{time} dt$$

To find the average heat flow rate over time (Q_a), Q_i is averaged over the system's total running time, where Q_i equals zero when the pump is non-operational.

4.3 Estimating Heat Flow from Solar Insolation For Modeling

4.3.1 Estimating Average Yearly Heat Flow Rate

In addition to the borehole heat exchanger modeling tool, a heat flow calculator was added to the model to aid in designing solar thermal remediation systems. Using readily available solar insolation values from the (Global Solar Atlas, 2021), the solar heat flow calculator determines the heat flow output of the borehole heat exchanger system dependent on local solar data and system design, allowing for optimization of solar collectors and the borehole heat exchanger loop as necessary in the design process (Figure 9). Users input collector type, number of collectors, number of boreholes, the longitude and latitude of the site being modeled, and the average daily global tilted solar irradiation (GTI) of the location into the model, which is used to calculate a per-borehole monthly average heat flow rate in Watts.

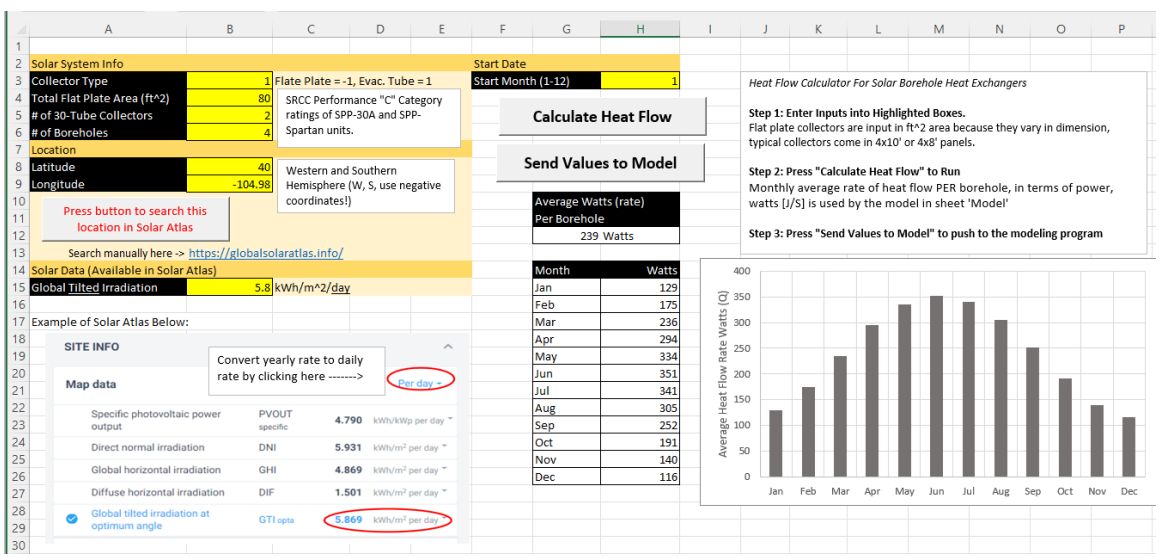

Figure 9: Example of the solar heat flow calculator tool that sends data to the analytical model.

The solar heat flow calculator uses the daily global tilted solar irradiation ($kWh/m^2/d$) value in combination with the Solar Rating and Certification Corporation (SRCC) ratings of either flat panel (Solar Panel Plus SPP-Spartan, 2020) or evacuated tube solar collectors (Solar Panel Plus SPP-30a, 2020) to determine the total solar energy produced by the system. The model uses the SRCC class C certification for the efficiency of heating water with a collector inlet temperature 5 to 20 degrees C higher than the average ambient temperature. This value is most appropriate for solar thermal borehole heat exchangers, which generally target a 5 to 20 degrees Celsius increase in the subsurface temperature over ambient. The SRCC rating curves are then used by the model to determine total heat flow to the system, shown in Figure 10 & Figure 11.

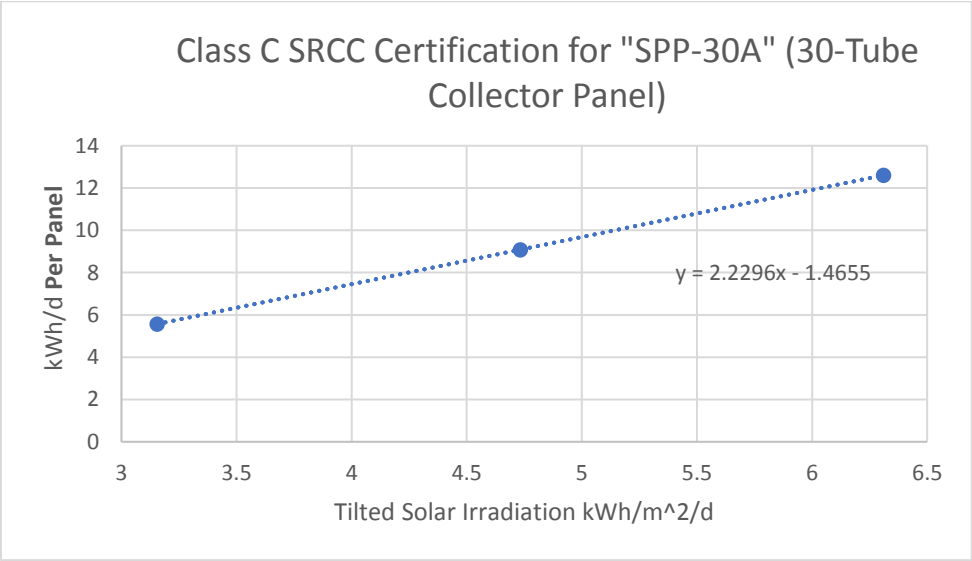

Figure 10: SRCC Certification for the “SPP-30A” solar collector, used as the representative rate of solar efficiency used to define 30-tube evacuated solar collectors in the model.

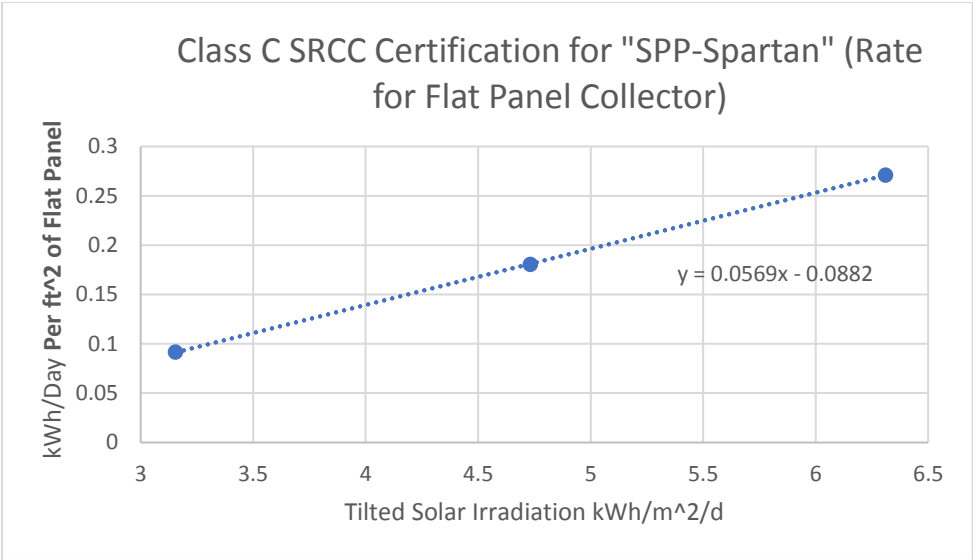

Figure 11: SRCC Certification for the "SPP-Spartan" flat panel, used as the representative rate of collector efficiency for flat panels in the model (the flat panel efficiency is referred to in units of energy per area as flat panel collector sizes vary more widely in area than evacuated tube arrays).

Once the total solar energy output of the system is determined, it is converted to a rate of power in Watts and divided by the number of boreholes in the system to produce an annual, average heat flow rate per borehole for use in the analytical model.

4.3.2 Estimating Average Monthly Heat Flow Rate

While the average heat flow rate from the Solar Atlas is accurate, it was also necessary to model seasonal fluctuations in heat flow due to varying monthly solar insolation. The Nasa ModelE AR5 SRMONLAT solar insolation modeling code (ModelE AR5 Simulations, 2021) is used to quickly produce a monthly periodical rate of heat flow from the average heat flow calculated in chapter 4.3.1 that reflects real seasonal

fluctuations in solar insolation. This was important for modeling monthly variations in temperature that may stray outside the desired range of subsurface heating.

The SRMONLAT code calculates the variance in solar insolation on a monthly basis for any latitude using the solar incidence angle, orbit, and tilt of the earth. The SRMONLAT code does not account for cloud cover and weather like the Solar Atlas data, however, which is why the solar atlas is used to provide the average heat flow. The SRMONLAT code was was used to produce a reference table of monthly percent change in insolation for every latitude, which is then automatically referenced using the solar insolation tool based on the latitude of the site in question.

An example of the percent change in heat flow predicted by the SRMONLAT solar insolation climate tool is shown in Figure 12.

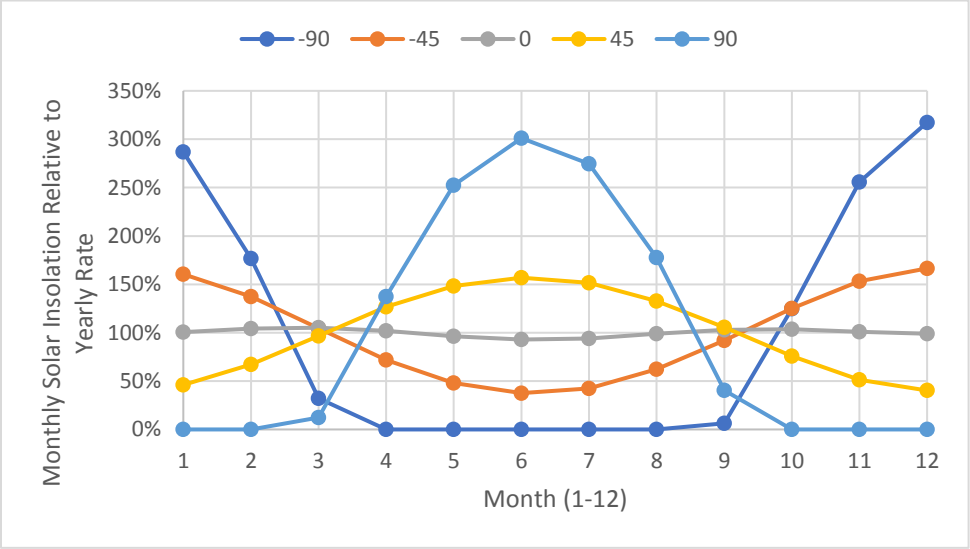

Figure 12: Example of monthly solar insolation rates relative to average, produced by the SRMONLAT ModelE AR5 NASA code at various latitudes.

5. COMPARISON OF ANALYTICAL AND NUMERICAL MODELS WITH NO GROUNDWATER FLOW

5.1 Single Borehole Heat Exchanger Models with No Groundwater Flow

In order to demonstrate the analytical model is a valid solution for modeling thermal heat flow, it was compared with the TOUGH multiphase EOS1 and EOS3 numerical modeling codes (Pruess et al., 1999.

The analytical solution was used to model simple borehole heat exchanger scenarios compared to identical simulations created using the TOUGH code. The TOUGH EOS1 solution was used for saturated numerical models, and the TOUGH EOS3 solution was used for partially saturated models, created using the Petrasim graphical user interface (Yamamato, 2008). The TOUGH code is an accepted numerical modeling solution that was used as the standard for the expected analytical model performance. The analytical model results were compared against the models running on the TOUGH code, also referred to as the numerical models, in all the simulations presented in chapter 5. The numerical model was also used to create and compare realistic vadose zone models to the analytical model, making it possible to assess whether the assumption of homogenous conditions carried by the analytical model is a source of significant inaccuracy when modeling partially saturated conditions.

5.1.1 Methods: Identical Saturated Models

The first scenario created was a comparison of near-identical models. The purpose of comparing a numerical model created using the TOUGH code with identical parameters to the analytical model was to validate the accuracy of the analytical solution.

If the analytical solution were accurate, the output from both models would be very similar. The sole difference that the analytical model could not account for is density-driven flow, which TOUGH models readily. To prevent this, low isotropic permeability of $1x10^{-15}$ m^2 was used in the numerical model to limit natural convection resulting from the borehole heat. Hydrogeologic properties such as porosity, rock heat capacity, rock grain density, and material thermal conductivity were all matched between the two saturated models (Table 1).

Table 1: Aquifer properties used by the single borehole saturated analytical model and single borehole saturated numerical model.

Shared Model Characteristics	Constants	Units
Porosity	0.1	Unitless
Rock heat capacity	1000	J/kg°C
Rock grain density	2650	kg/m^3
Wet Thermal Conductivity λ (all saturated)	3	W/m°C
Permeability (horizontal and vertical)	$1x10^{-15}$	m^2

A conceptual model was created, representing typical borehole heat exchanger placement from a depth of 5 to 10 meters. Both models' temperature observation points were placed at distances along the x-axis at distances of 1, 3, and 5 meters to the east of the borehole heat exchanger (Figure 13). Temperatures in both models were recorded at the midpoint depth of the borehole heat exchangers. The analytical model was adjusted to observe temperatures at points that matched the numerical model depending on vertical grid spacing. For example, if the numerical model read the temperature of a cell that spanned depths 7 to 8 meters, the analytical model was set to observe the temperature at a depth of 7.5 meters.

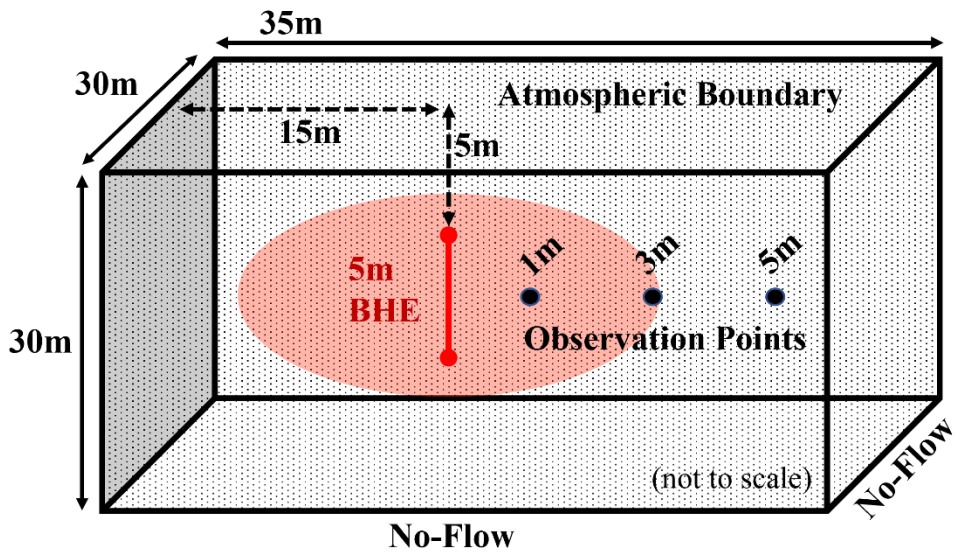

Figure 13: Conceptual model for comparing the analytical model to the numerical model in single borehole scenarios with no flow defining borehole placement and model boundaries.

The analytical model had a built-in atmospheric boundary temperature condition with a constant initial temperature. Unlike the numerical model, it has no depth and horizontal range boundaries since it assumes an infinite system.

The numerical model had a 0.01 m top layer fixed at a steady state of 101,325 Pa and 25 degrees Celsius to create a boundary condition simulating the atmosphere. The model has horizontal dimensions of 30 by 35 meters and is 30 meters deep. The horizontal boundaries of the numerical model were placed at distances from the borehole heat exchanger where heat conduction would not reach in order to avoid irregularities associated with no flow conditions (Figure 14). Multiple models with a vertical grid spacing of 2.5, 1, and 0.5 meters were created to evaluate the potential influence of grid spacing. A

Voronoi polygon system was used for horizontal discretization, with a minimum area of 0.1 meters refined around the observation points and the borehole heat exchanger.

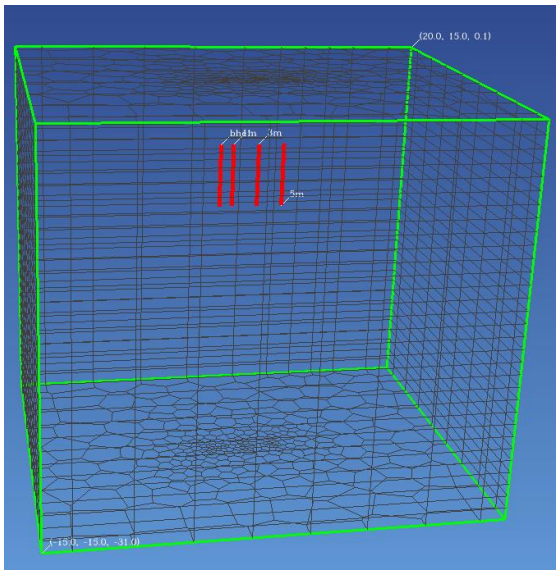

Figure 14: 3-dimensional representation of the simplified model in Petrasim operating off the TOUGH code. Boreholes and monitoring wells are represented by red lines, while grey lines outline the integral finite-difference grid.

Over one year, the models were subjected to a heat flow rate of 1000 watts from the single 5m borehole heat exchanger, after which the borehole was turned off, allowing the aquifer to cool. Temperature readings from the numerical and analytical models were compared using normalized root mean squared error and maximum error to evaluate the accuracy of the analytical solution. The normalized root mean squared error (NRMSE) of the analytical model over the max change in temperature observed in the numerical model benchmark was used to assess the model's accuracy.

5.1.2 Results: Identical Saturated Models

Shown in Figure 15 is an example of the numerical model with the borehole heat exchanger, a red line in the far left heating the subsurface. One may observe the top boundary condition of the atmosphere, where the heat travels to, with the other edges being infinite flow boundaries and the red observation wells to the right of the borehole heat exchanger, which were used to determine temperatures at a designated point.

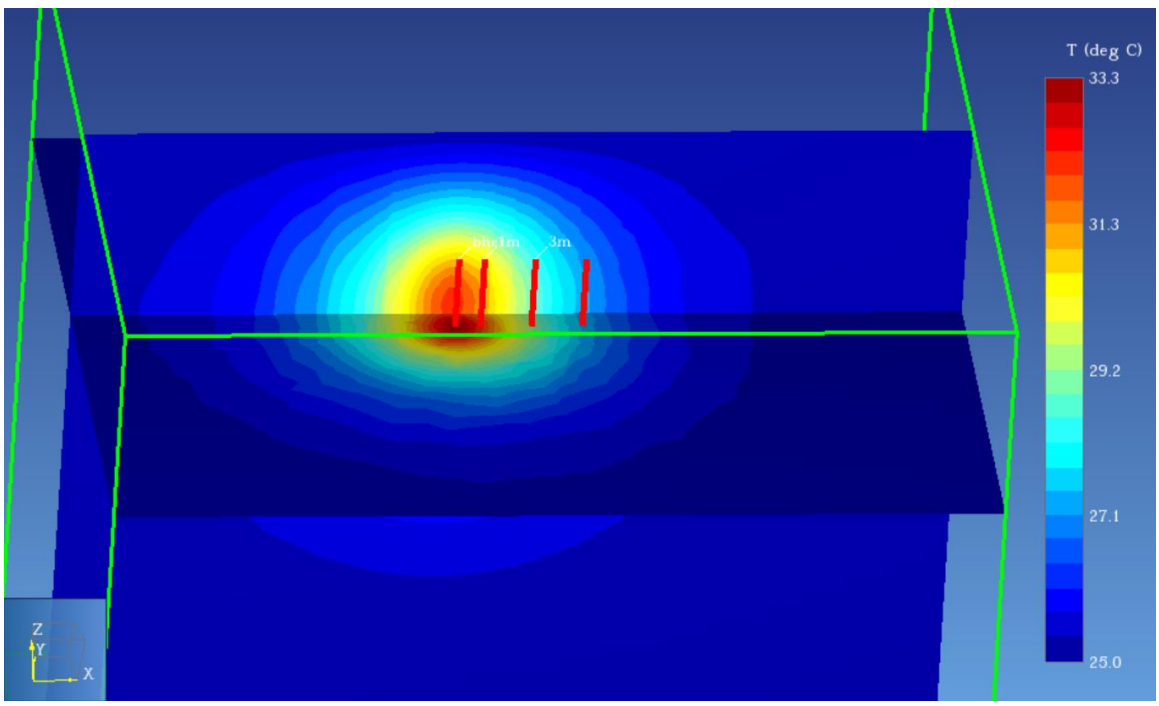

Figure 15: Saturated numerical model showing temperature gradient interpolated between grids at T=15 months after the boreholes were turned off. Presented as a 3-dimensional sliced plane view of z=-7 and y = 1. Model orientation indicated in the bottom left.

The normalized RMSEs of the analytical model versus the numerical model are shown in Figure 16 were: A) 1.4%; B) 0.5%; C) 0.2% with maximum errors in degrees C of: A) 0.88; B) 0.25; C) 0.16.

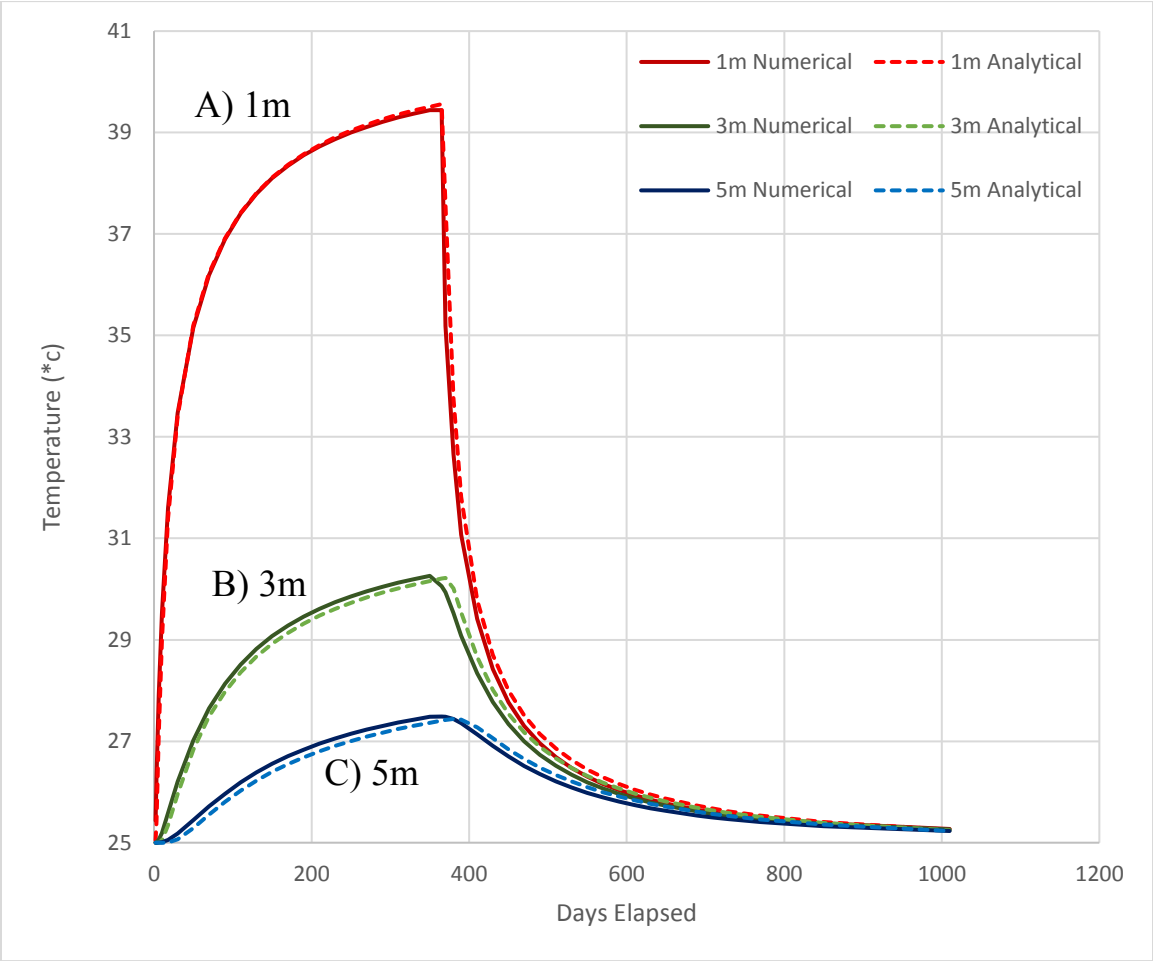

Figure 16: Comparison of temperatures observed in the saturated analytical flow model and saturated numerical flow model. Observation points at depth z=7.5m.

5.1.3 Methods: Analytical Model Versus Partially Saturated Numerical Models

Numerical models with vadose zones of different depths were created to assess the potential inaccuracies of the analytical model, which cannot simulate partially saturated conditions due to the assumption of a homogenous aquifer. The partially saturated numerical models used the TOUGHEOS3 code, designed for partially saturated water, air, and heat systems (Pruess et al., 1999). This proven numerical model was used as the benchmark for the analytical model, which produced similar results.

The numerical models were created with water tables at depths of 5, 7.5, and 9 meters from the surface. At 5 meters depth, the water table was the same level as the top of the borehole heat exchanger, at 7.5 meters depth, the water table was at the midpoint of the borehole heat exchanger, and at 9 meters depth, the water table only covered the bottom meter of the borehole heat exchanger, leaving it primarily in the unsaturated zone. The water tables were created using the bottom boundary conditions of fixed hydraulic pressure equivalent to the desired groundwater head. Pressures of 245,159, 220,643, and 205,934 Pa over the atmospheric pressure of 101,325 Pa were used to add 25, 22.5, and 21 meters of hydraulic head into the models, respectively (Figure 17). The darkest blue contour shows a pressure head of 101,325 Pa, equal to atmospheric pressure, defining the boundary of the groundwater table where the partially saturated vadose zone begins.

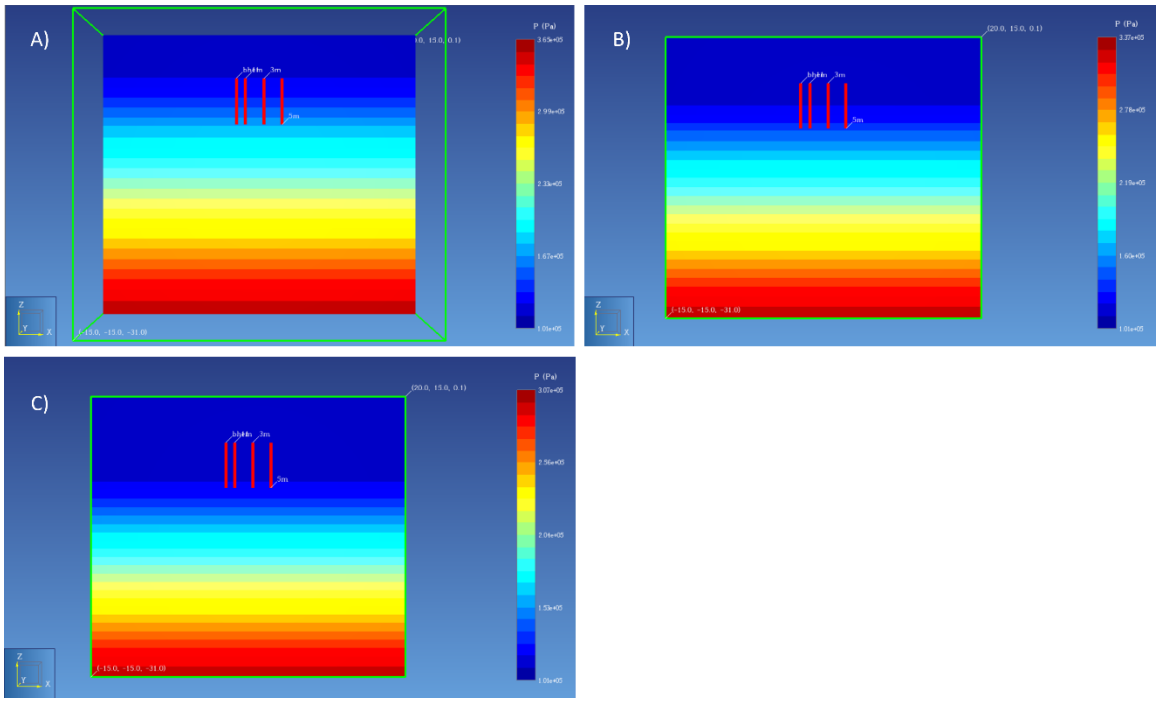

Figure 17: Cross-sectional view of the contours of water pressure in the partially saturated models, in Pascals. Numerical models have fixed pressure heads used to emulate vadose zones. Model A) has a water table depth of 5 meters. Model B) has a depth to water table of 7.5 meters. Model C) has a depth to water table of 9 meters.

In the models λ_{dry} = 0.7 W/m°C while λ_{wet} = 2.0 W/m°C. Heat conductivity of the aquifer material (λ) was interpolated in the numerical model using the method shown in equation 15. S_w of the model, the volumetric water saturation, is used to dictate the thermal conductivity of the subsurface, interpolating between the values of λ_{wet} conductivity and λ_{dry} conductivity in units of W/m°C.

$$\lambda = \lambda_{dry} + \sqrt{S_w} \cdot (\lambda_{wet} - \lambda_{dry}) \tag{15}$$

The interpolated heat conductivities taken from grid values of the numerical model are shown in Figure 18.

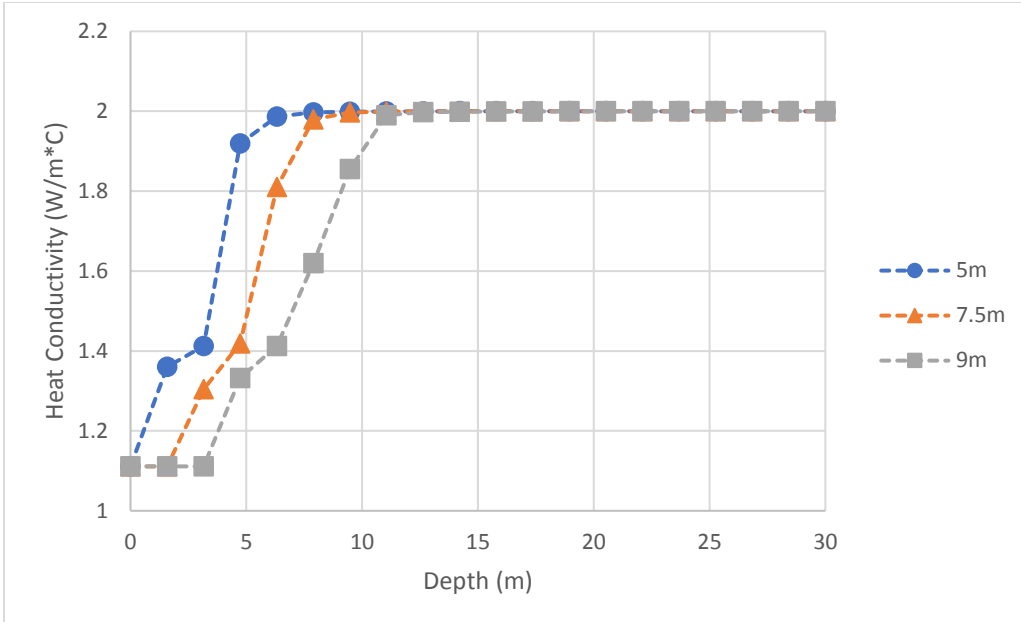

Figure 18: Interpolated heat conductivity, by depth, of the numerical models with water tables at depths of 5, 7.5, and 9 meters depth.

Capillary pressure in the numerical model was determined using the Leverett J-Function with a residual saturation value, S_{wr}, of 0.1 and capillary pressure p_c of $1x10^6$. The equalized, steady-state models were used to set the initial conditions for the numerical vadose zone models with borehole heat exchangers. Excluding the new bottom layer boundary condition, these models were constructed with horizontal boundaries, borehole installation geometry, grid sizing, and observation points identical to the methods listed for the saturated numerical models in 5.1.1.

The average thermal conductivity of the analytical models was determined using the methods listed in chapter 3.7. The analytical model with the 5m deep groundwater table had a thermal conductivity of 2.0 W/m°C as borehole heater was completely

saturated, the analytical model for the 7.5m deep groundwater table used a calculated average thermal conductivity of 1.8 W/m°C, while the analytical model with the 9m depth to groundwater used a calculated thermal conductivity of 1.3 W/m°C. The plot used to interpolate average thermal conductivity λ for the analytical model along depths 5 meters to 10 meters is shown in Figure 19. Other key characteristics of the analytical and numerical models are listed in Table 2.

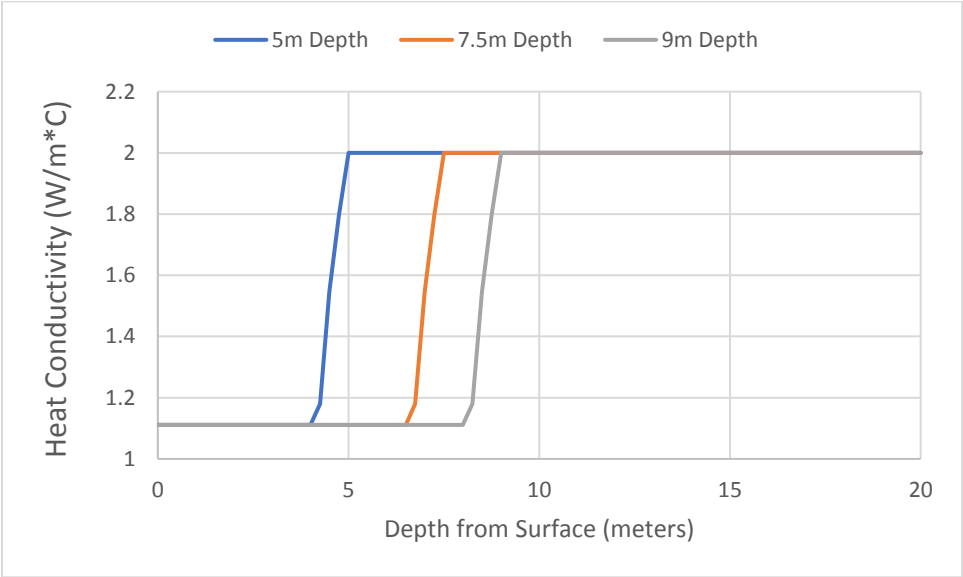

Figure 19: Heat conductivity plot used by the 5m, 7.5m, and 9m, analytical groundwater models to estimate average thermal conductivity along the length of the borehole from 5m to 10m depth.

Table 2: Aquifer properties used by the analytical model and paired unsaturated numerical models.

Shared Model Characteristics	Constants	Units
Porosity	0.2	unitless
Rock heat capacity	1000	J/kg°C
Rock grain density	2650	kg/m^3
Wet Thermal conductivity (λ_{wet})	2.0	W/m°C
Dry Thermal conductivity (λ_{dry})	0.7	W/m°C
Permeability	$1x10^{-12}$	m^2
Water Residual Saturation (S_{wr})	0.1	Dimensionless

The normalized root mean squared error (NRMSE) of the analytical model over the maximum change in temperature observed in the numerical model benchmark was used to assess the model's accuracy. By evaluating the analytical model against partially unsaturated conditions, the error stemming from assumptions of a homogenous aquifer made by the analytical modeling tool can be quantified.

5.1.4 Results: Analytical Versus Partially Saturated Numerical Models

In the model with a depth to water table of 5 meters and permeability of $1x10^{-12}$ m/s, the vadose zone reaches the top of the borehole heat exchanger, but the heater remains entirely submerged in the saturated aquifer (Figure 17, A). The normalized RMSEs of the analytical model versus the benchmark numerical model shown in Figure 20 were: A) 1.5%; B) 1.1%; C) 0.8% with maximum errors in degrees C of A) 3.3; B) 0.8; C) 0.4.

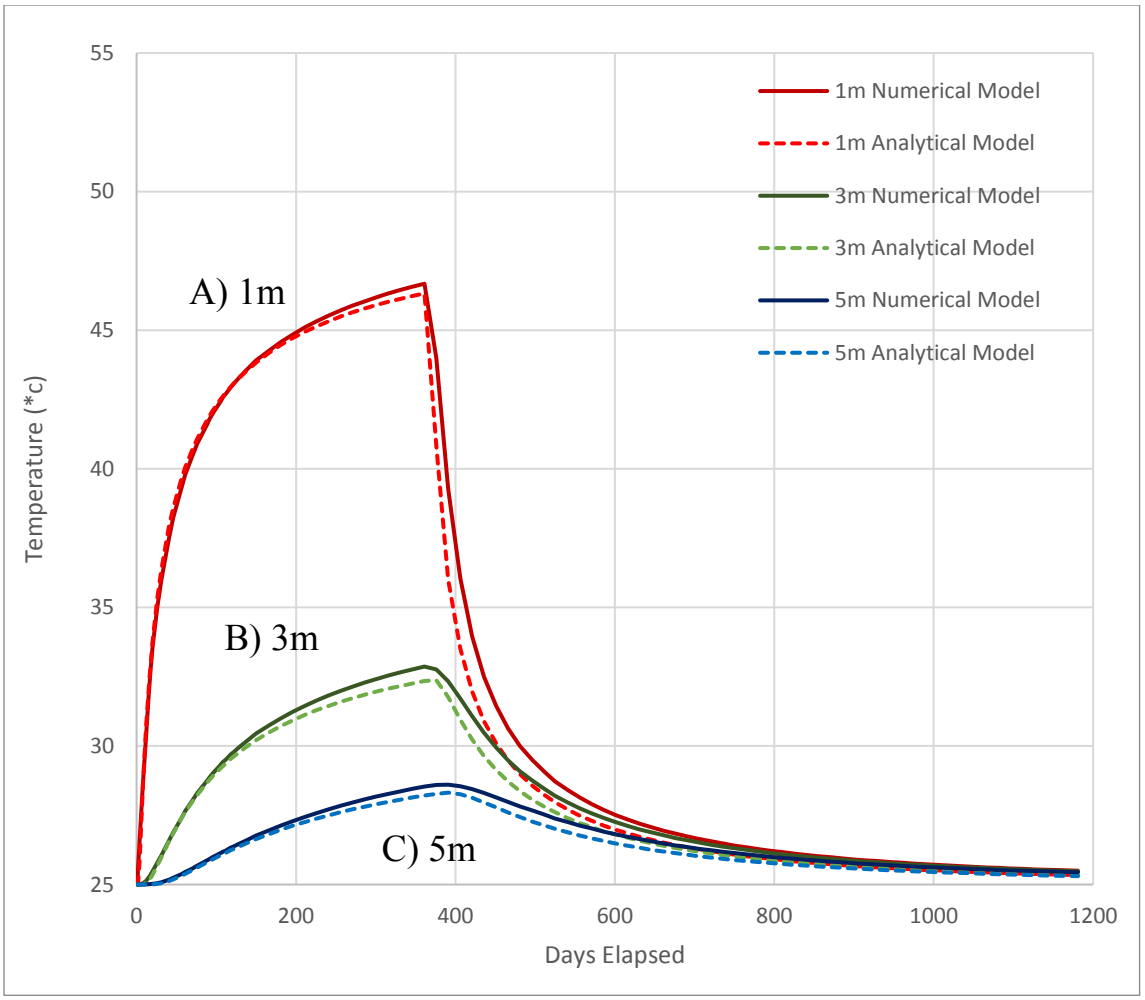

Figure 20: Comparison of temperature over time observed in the saturated analytical model at a permeability of $1x10^{-12}$ and groundwater depth of 5 meters. Observation points at depth z=7.75m, 1m, 3m, and 5m from the BHE.

In the model with a depth to water table of 7.5 meters, the unsaturated zone reached the center of the borehole heat exchanger (Figure 17, B). The normalized RMSEs of the temperatures observed in the analytical model versus the benchmark numerical model shown in Figure 21 were: A) 1.2%; B) 1.0%; C) 0.8% with maximum errors in degrees C of: A) 2.2; B) 0.5; C) 0.4.

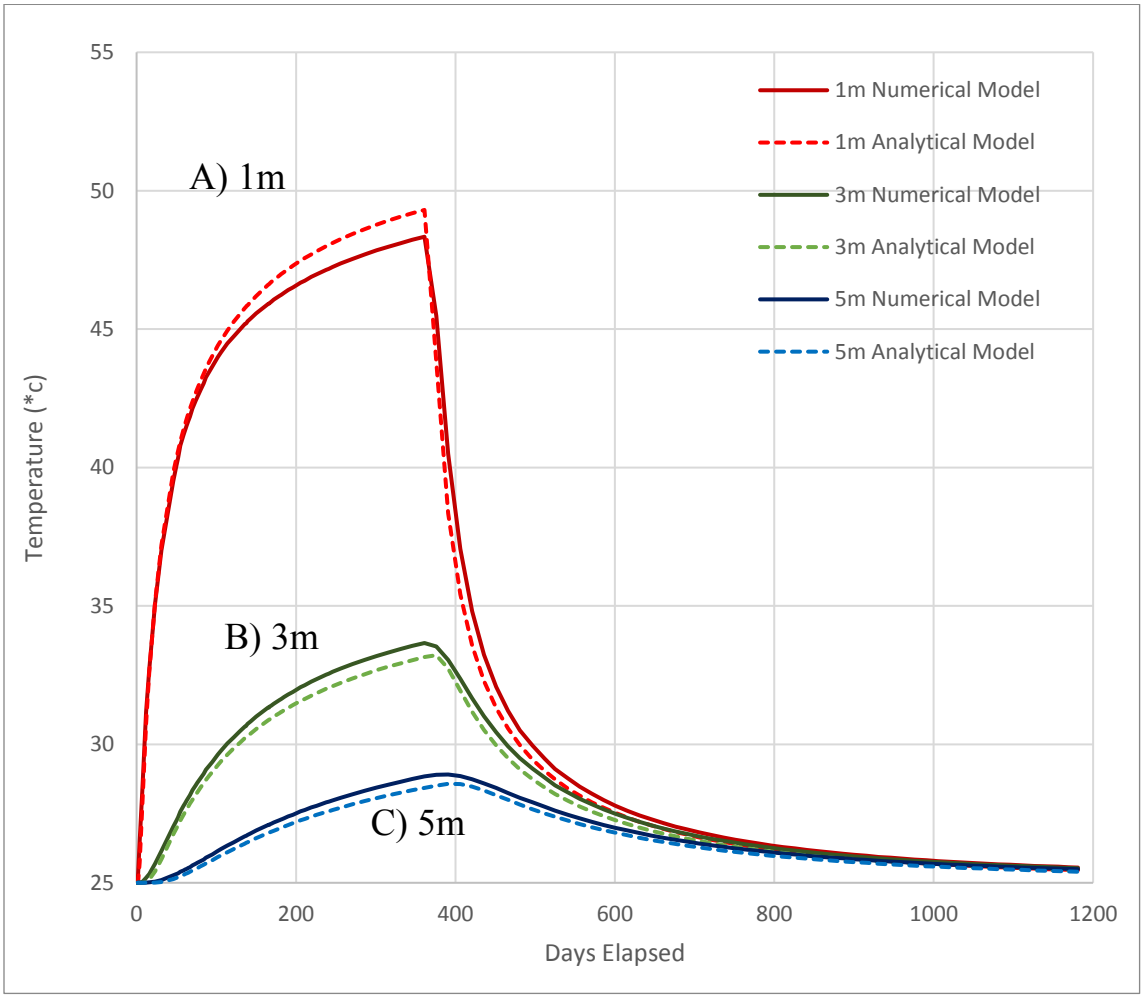

Figure 21: Comparison of temperature over time observed in the saturated analytical model at a permeability of $1x10^{-12}$ m^2 and groundwater depth of 7.5 meters. Observation points at depth z=7.75m, 1m, 3m, and 5m from the BHE.

In the model with a depth to water table of 9 meters, the borehole heat exchanger is primarily placed within the unsaturated zone (Figure 17, C). The normalized RMSEs of the analytical model versus the benchmark numerical model shown in Figure 22 were: A) 2.2%, B) 7.8%, and C) 6.2% with maximum errors in degrees C of: A) 1.5; B) 1.0 C) 0.4.

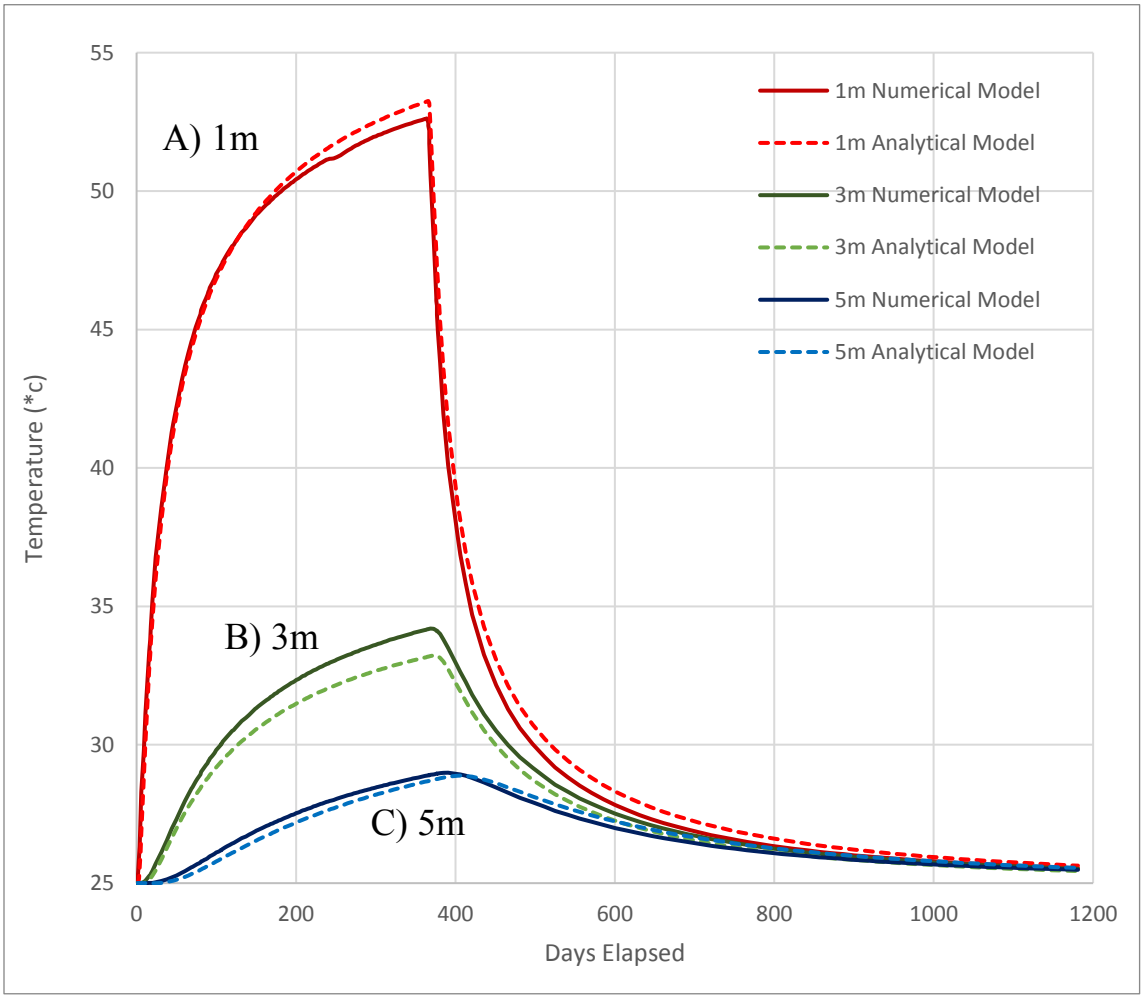

Figure 22: Comparison of temperature over time observed in the saturated analytical model at a permeability of $1x10^{-12}$ m^2 and groundwater depth of 9 meters. Observation points at depth z=7.75m, 1m, 3m, and 5m from the BHE.

A sliced plane view of the numerical models shows that the buoyancy-driven natural convection in saturated zone may have influenced the heat plume shape to move upwards in the numerical model (Figure 23).

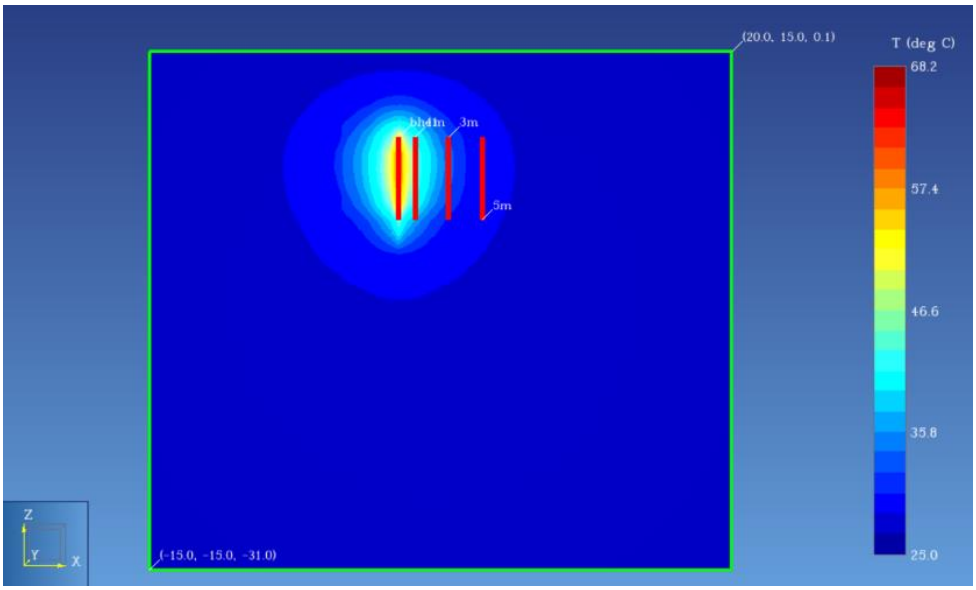

Figure 23: Cross-sectional side view of the heat plume created by the borehole heat exchanger, in the numerical model at t = 360 days.

A comparable cross-section of the same scenario but with entirely saturated conditions was also created using the analytical model. The analytical model shows an idealized heat plume that is more uniform (Figure 24), while the numerical model heat plume (Figure 23) is more “tear-drop” shaped.

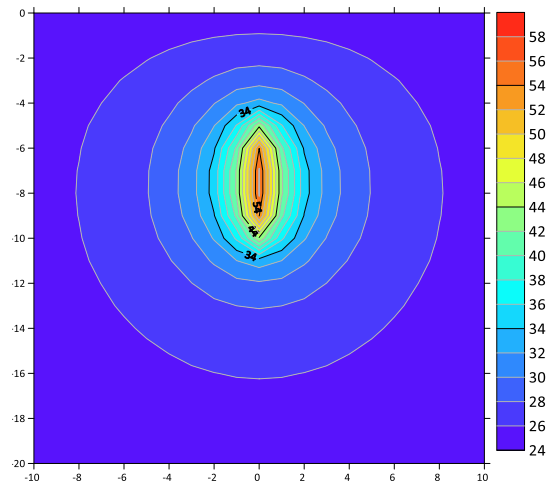

Figure 24: Cross-sectional side view of the heat plume from the borehole heat exchanger created with the analytical model at t = 360 days.

5.1.5 Methods: Analytical Model Versus High Permeability Numerical Model

Another numerical model was created with a 5-meter unsaturated zone but with increasingly high permeabilities to compare with the analytical model. The purpose of this model was to determine where the density-driven flow of heated groundwater becomes a source of error since the analytical model assumes uniform density of water and ignores natural convection. It was shown at higher permeabilities, the inability to model natural convection becomes a source of error in the analytical model.

The numerical model was created nearly identically to the methods in 5.1.3 for creating a partially saturated model in TOUGH EOS3 with a 5-meter vadose zone directly above a borehole heat exchanger pictured in Figure 17 A). The models were raised to a range of permeabilities equivalent to a low hydraulic conductivity of $1x10^{-9}$ m/s to a high conductivity of $1x10^{-3}$ m/s. Properties used to define the model can be

viewed in Table 3. Observation points were placed at a depth of 7.5m at the midpoint of the borehole, 1, 3, and 5m in distance from the borehole.

Table 3: Properties used by the partially saturated numerical models with a high permeability.

Shared Model Characteristics	Constants	Units
Porosity	0.2	unitless
Rock heat capacity	1000	J/kg°C
Rock grain density	2650	kg/m^3
Wet Thermalt conductivity (λ_{wet})	2.5	W/m°C
Dry Thermal conductivity (λ_{dry})	0.7	W/m°C
Permeability	5x10^{-10} to 1x10^{-15}	m^2

5.1.6 Results: Analytical Model Versus High Permeability Numerical Model

In the model with a 5m vadose zone above the borehole, the higher permeability aquifer simulated at 5x10^{-10} m^2 observed a different heat plume in the numerical model compared to the analytical model (Figure 25). In the numerical model, natural convection caused the heated water to rise, while the analytical model could not account for natural convection, exhibiting a maximum error of 15°C from the numerical benchmark at the 1m observation point (Figure 26).

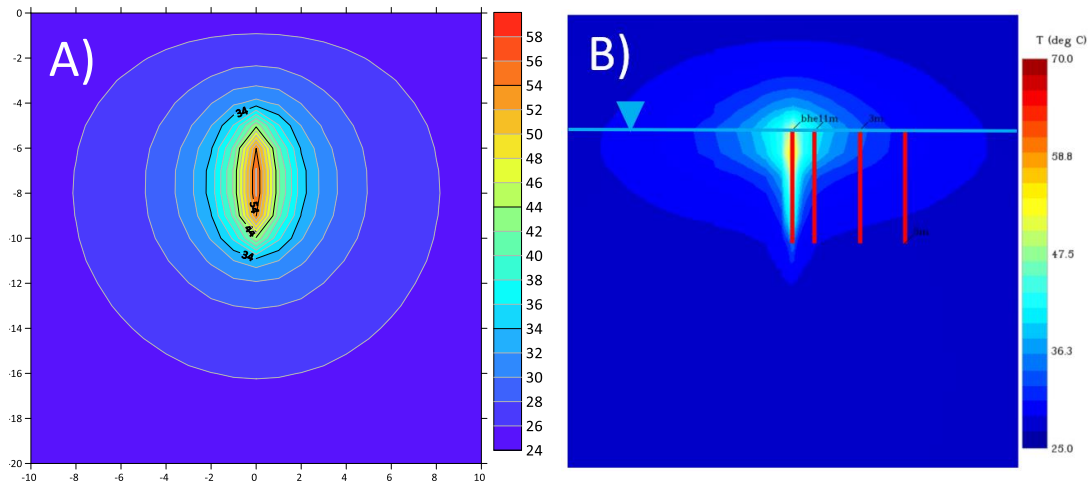

Figure 25: Cross-sectional side view of the temperature contours in the A) analytical model assuming saturated conditions versus B) the numerical model at a permeability of $6x10^{-10}$ m^2 with an unsaturated zone directly above the borehole.

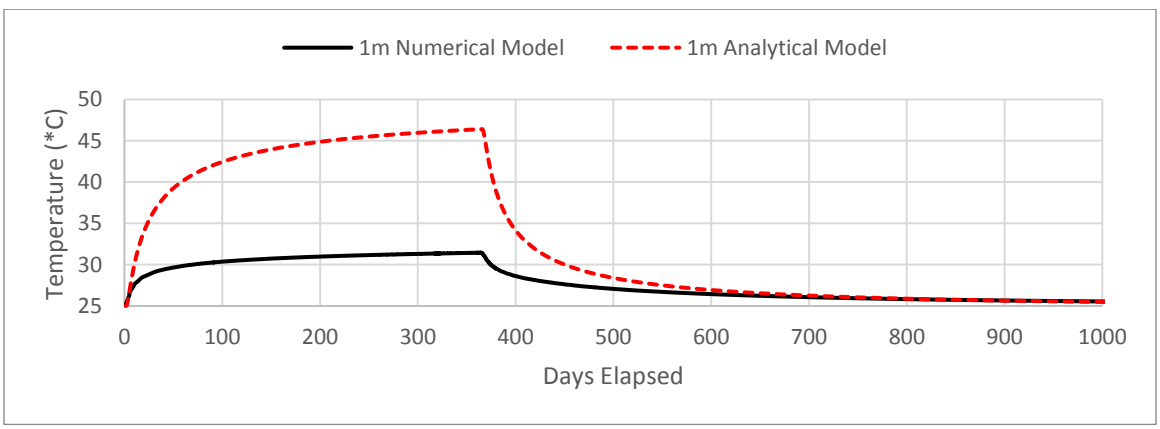

Figure 26: Comparison of the analytical and numerical model temperatures when simulating a system with a hydraulic conductivity of $9.81x10^{-4}$ m/s at a distance of 1m from the borehole, with the observation taken at 7.5m depth.

It was shown that the average error of the analytical model, shown as RMSE normalized over the range of the model, increased as the hydraulic conductivity of the models became greater than $1x10^{-4}$ m/s, shown in Figure 27 when measuring the

temperature 1m from a borehole heat exchanger. The maximum error of the analytical model reached 90% at a hydraulic conductivity of 4.9×10^{-3} m/s (Figure 28).

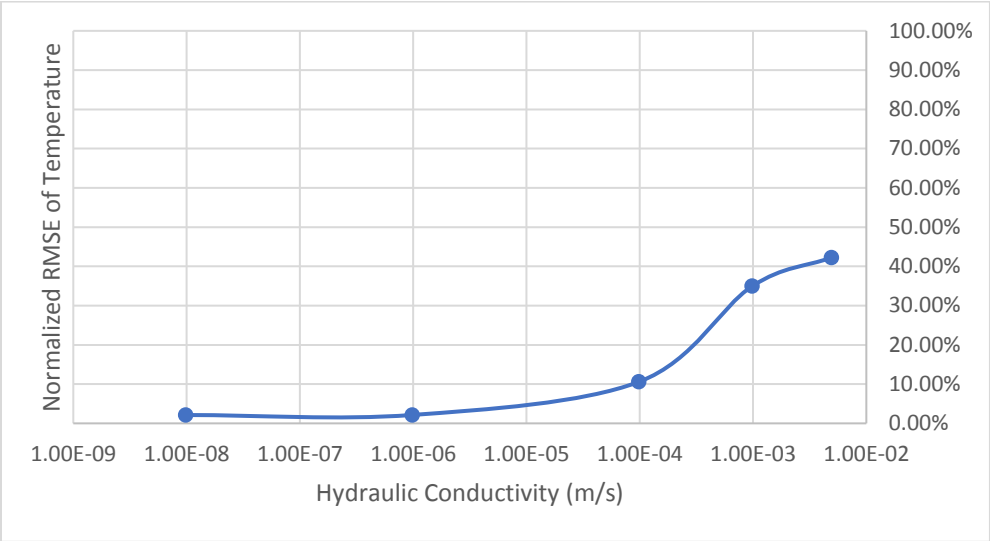

Figure 27: Average percent error, via NRMSE of the analytical model when attempting to model heat flow in increasingly high hydraulic conductivities, ranging from 9.8×10^{-9} to 4.9×10^{-3} m/s with measurements taken 1m from the borehole heat exchanger.

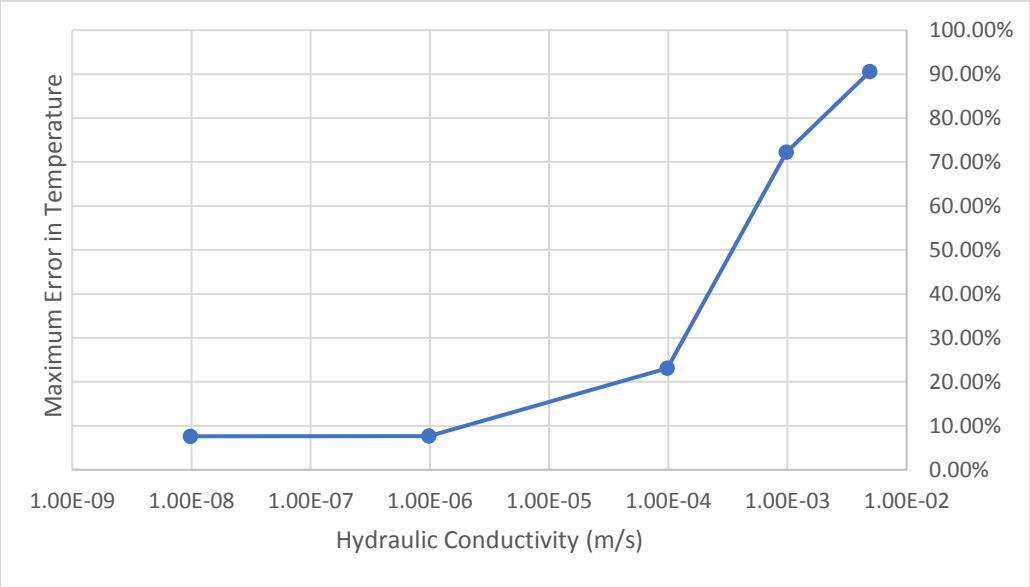

Figure 28: Maximum % error of the analytical model when attempting to model heat flow in increasingly high hydraulic conductivities, ranging from 9.8×10^{-9} to 4.9×10^{-3} m/s with measurements taken 1m from the borehole heat exchanger at its midpoint.

5.2 Single Borehole Heat Exchanger Model with Groundwater Flow

5.2.1 Methods

The analytical model possesses the ability to model homogenous groundwater flow in a system. To verify the accuracy of the analytical flow solution, it was compared to an analogous numerical model with an identical groundwater flow rate to which it performed similarly. The numerical model was created as a fully saturated model based on the TOUGH2 EOS1 code (Pruess, 1999).

The numerical flow model used in this scenario had horizontal no-flow boundaries 500 meters in the y and x-axis with a z-axis depth of 300m. A fixed temperature boundary was set at the top of the model to simulate the atmosphere. A single borehole heat exchanger was placed in the model's center at a depth from 5 to 10 meters. The conceptual model used to define the numerical and analytical model is displayed in Figure 29.

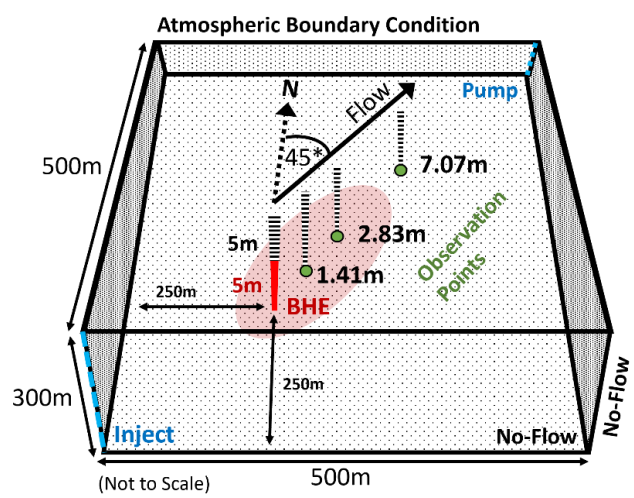

Figure 29: Conceptual model of the diagonal flow scenario created to compare flow scenarios in the numerical and analytical models. Blue dotted lines indicate the simulated well screens used to induce flow.

Observation points were placed diagonally from the borehole heater at an azimuth of 45 degrees, with coordinates relative to the heater at points: x=1, y=1; x=2, y=2; and x=5, y=5. The distances of these observation points from the borehole were calculated to be 1.41, 2.83, and 7.07 meters, respectively. For the numerical model, horizontal discretization of the model was created using Voronoi polygons with a minimum grid size of 0.5m. The vertical layers were refined around the heater and observation points with a minimum height of 0.5 meters.

The analytical model was constructed with identical observation points, borehole heat exchanger placement, and identical aquifer material properties, visible in Table 4.

Table 4: Aquifer properties used by the analytical and numerical models with groundwater flow.

Shared Model Characteristics	Constants	Units
Porosity	0.1	Unitless
Rock heat capacity	1000	J/kg°C
Rock grain density	2650	kg/m^3
Wet Thermal conductivity ((λ_{wet}, Fully Saturated Model)	2.5	W/m°C
Permeability	$1x10^{-12}$	m^2

Flow was simulated in the numerical model by injecting and pumping water from the bottom left corner to the top right corner respectively at a total rate of 70 kg/s along the 300-meter well length (Figure 30). The pressure differential between the two corners was allowed to reach a steady state, providing the initial flow conditions used for the numerical model.

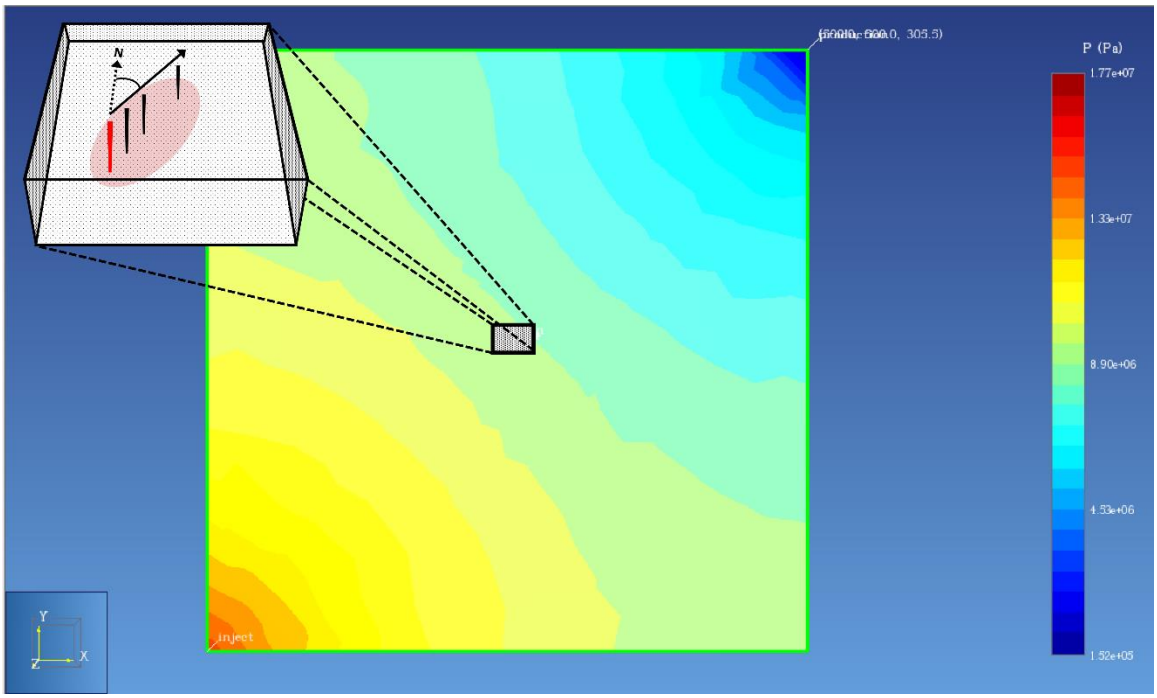

Figure 30: Cross-sectional top view at depth z=8.75m of an exaggerated example (not used for the model) of a pressure gradient induced from injection in the bottom left and pumping in the top right to create diagonal groundwater flow through the highlighted area of interest.

The boundaries of the model were created much larger than the area of interest to allow the flow contours within the area of interest to be near-parallel, resembling a homogenous 45-degree flow. In Figure 30, this can be observed, where the pressure contours are similar to equipotential lines, perpendicular to the flow direction. In the numerical model, the darcy velocity (q) between the closest and farthest observation points was determined to be 15.16 m/yr (4.8×10^{-15} m/s) after recording a pressure differential of -0.272 meters of head over a 5.66-meter length, multiplied by the hydraulic conductivity of the system at 1×10^{-5} m/s, using Darcy's Law. This value was cross-referenced with the measured rate of mass flow in the x and y direction of the grid blocks,

which were equal in both directions, at rates of 3.4×10^{-7} kg/m^{2}s, constraining the vector of groundwater flow to an azimuth of 45 degrees. Converting the mass flow rate (kg/s) to flux (m/s) gave a darcy velocity of 15.6 m/year as well, further validating the flow rate. This rate and flow direction were then applied to the comparable analytical model.

The models were both injected with a heat flow (Q) of 400 watts for a year and allowed to cool. Temperature readings were taken at a depth of 8.75m for both models at each observation point, the closest grid block interval to the midpoint of the borehole in the numerical model. The normalized root mean squared error, calculated as RMSE between the two models, over the maximum change in the numerical model, was used to assess the analytical model's accuracy in modeling advective transport of heat.

5.2.2 Results

The numerical flow model (Figure 21) and the analytical flow model (Figure 22) produced thermal contour maps over time that resemble each other at visual inspection. Once the one-year pulse in heat occurs, the attenuating heat continues to move via advection with the groundwater flow, keeping in mind the scales of the contours are changing.

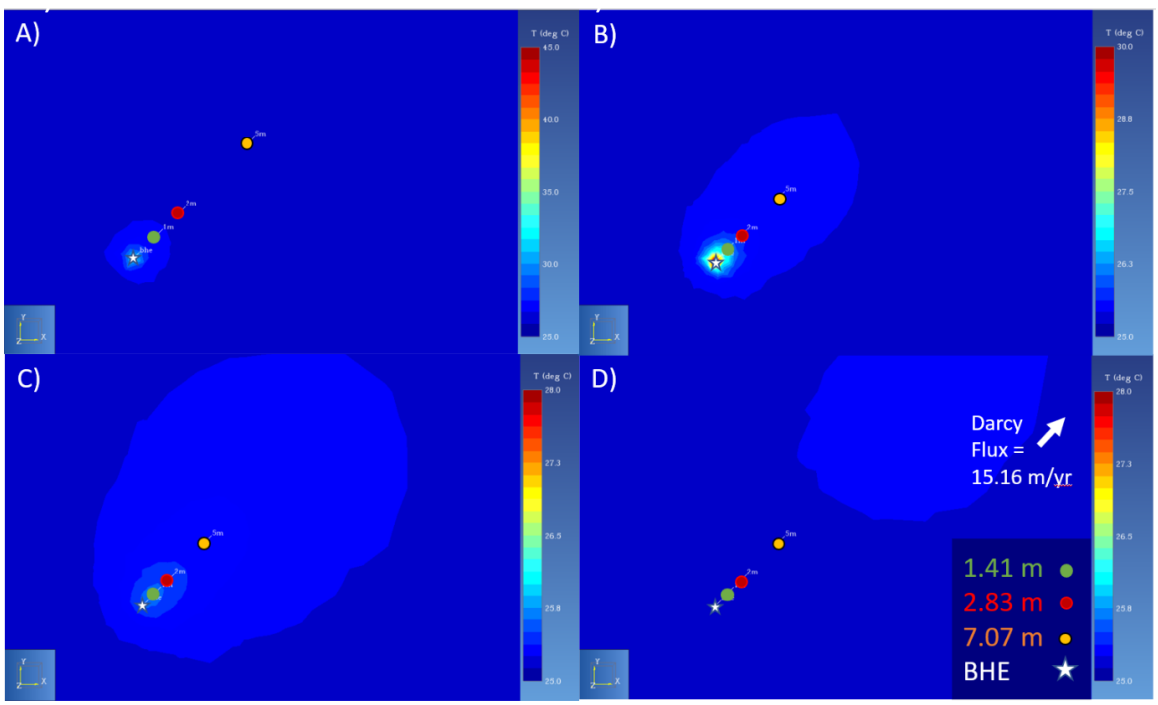

Figure 31: Cross-sectional top view of temperature (°C) at depth z=8.75 of the numerical flow model. A) T=10 day; B) T=360 days; C) T=390 Days; D) T=668 days.

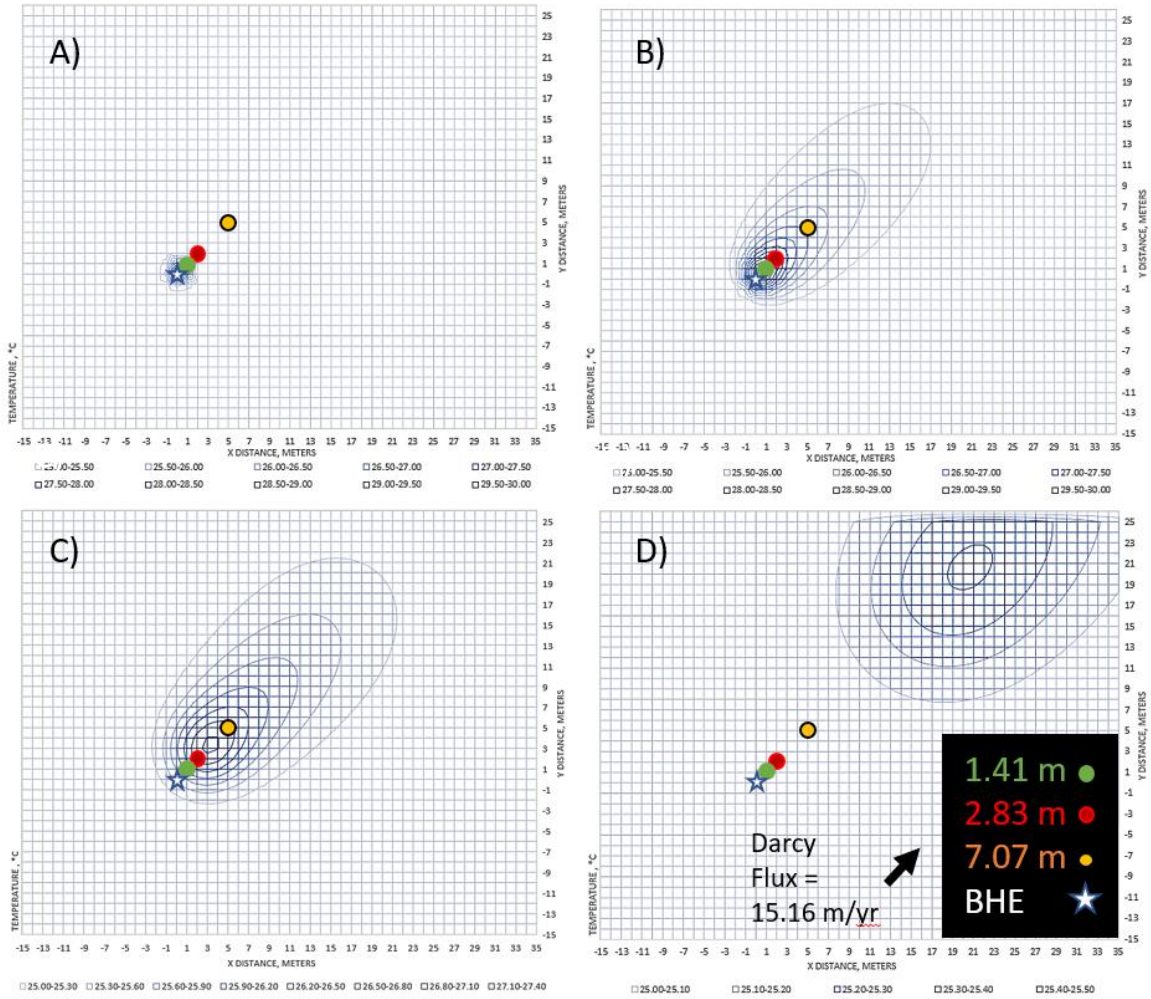

Figure 32: Cross-sectional top view of temperature (°C) at depth z=8.75 in the analytical flow model. A) T=10 day; B) T=360 days; C) T=390 Days; D) T=668 days.

The normalized RMSEs between the analytical and numerical flow model observation points shown in Figure 33 were: A) 6.1%, B) 4.3%, C) 3.2% with maximum errors, in degrees C, of: A) 0.7; B) 0.5 °C; C) 0.1 °C.

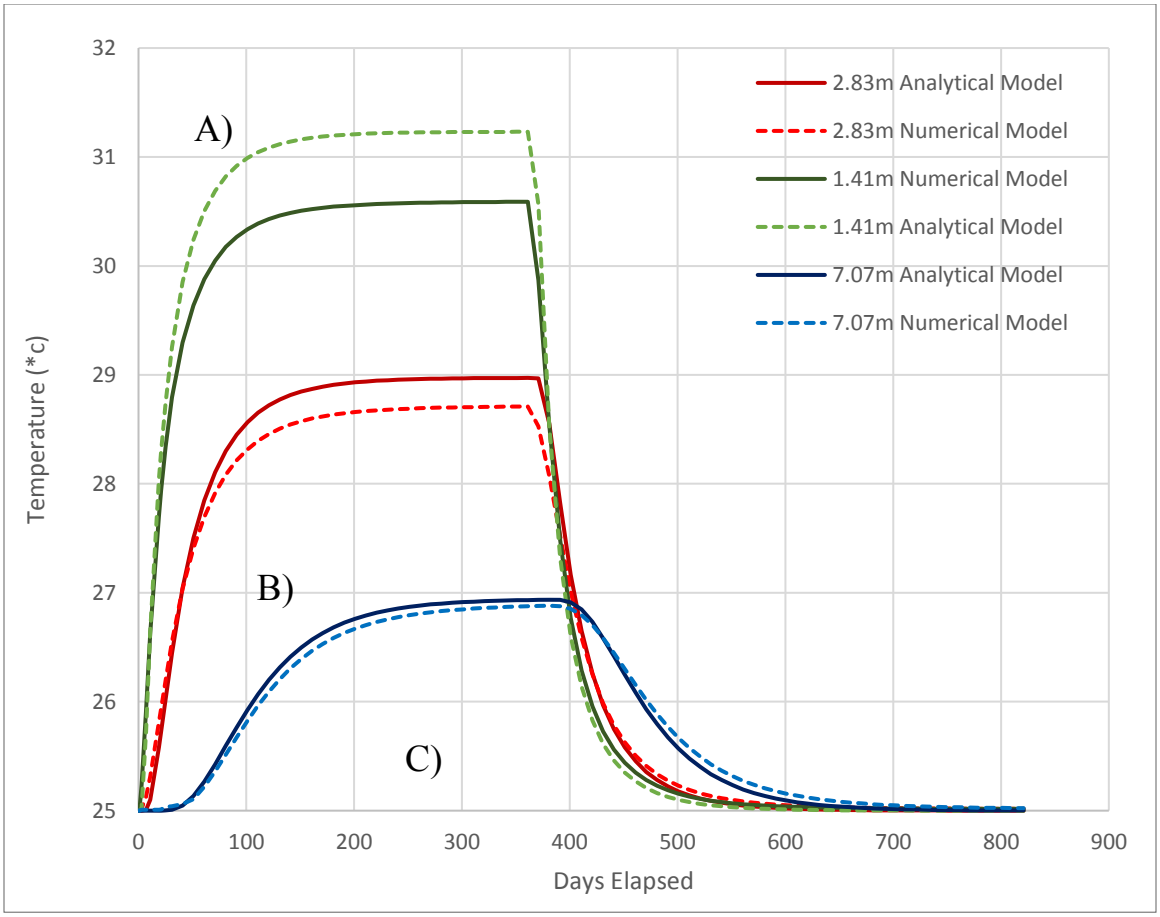

Figure 33: Comparison of temperature over time observed in the analytical flow model and numerical flow model. Observation points at depth z=8.75m and distances 1.41, 2.83, and 7.07m from the heater.

5.3 Multiple Borehole Heat Exchanger Model with Seasonally Variable Heat Flow

5.3.1 Methods

For the third modeling scenario comparing the analytical model to the proven numerical model, a model with multiple borehole heat exchangers with a seasonally fluctuating heat flow was created. The purpose of this scenario was to assess the accuracy of the analytical model when using superposition to model multiple boreholes at once and

test the transient heat flow functionality of the analytical model, which can simulate a monthly variable heat flow rate (Q).

A saturated and partially unsaturated numerical model of the CDOT site was created to function as expected values similar to the previous scenarios in 5.1.1 and 5.1.3. The comparison of identical saturated models was intended to validate the accuracy of the analytical solution. The partially unsaturated numerical model was designed to represent a more realistic real-world scenario and ensure the analytical model is reasonably accurate despite ignoring the variation of thermal properties in the vadose zone.

The analytical and numerical models were constructed with identical borehole heat exchangers and observation locations to the relative coordinates of the real CDOT site, with the model centered around borehole heat exchanger 1 (BHE 1), placed in the center of the model at x=0, y=0 (Figure 34).

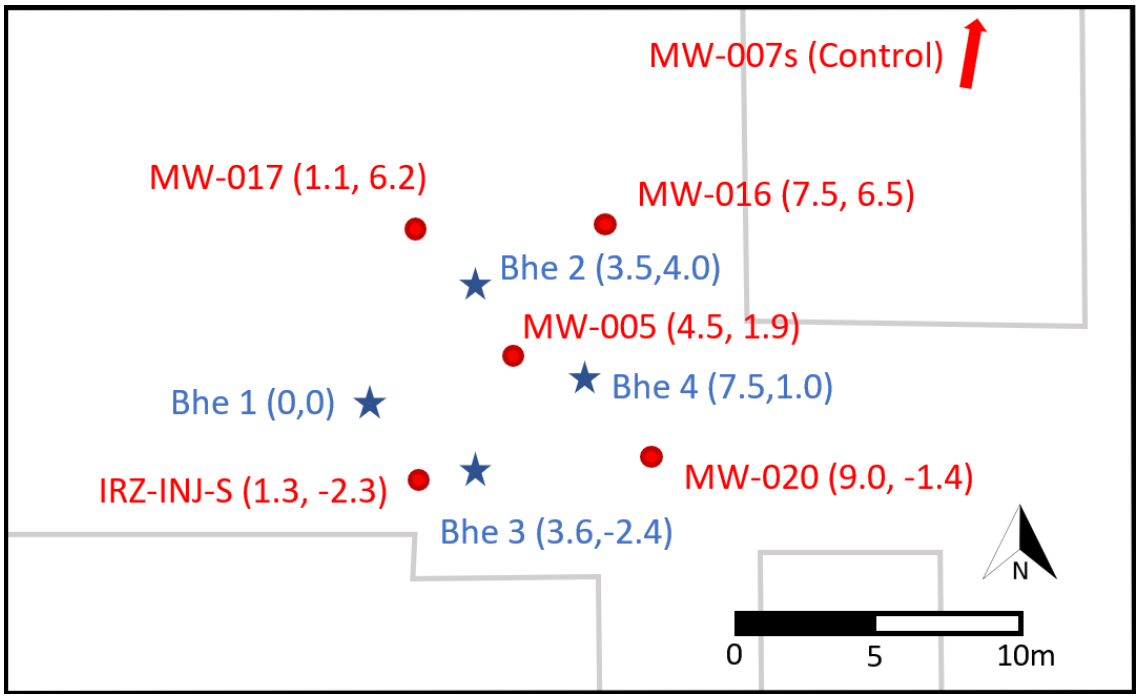

Figure 34: Simplified map of the CDOT site and coordinates of observation wells and borehole heat exchangers (BHEs) used for modeling.

The numerical model was created with a 55-meter x-axis and 40-meter y-axis with a total depth of 30 meters, constraining the system with no flow boundaries on the sides of the model. Atmospheric boundary conditions were identical to the methods used in 5.1.1. For the numerical model that simulated the CDOT site with a vadose zone, a depth to groundwater of 5 meters was created using a hydrostatic pressure gradient that was allowed to reach steady-state for use as the initial conditions, using the same method for creating a 5-meter vadose zone described in chapter 5.1.3, the dry and wet conductivity was interpolated using the values listed in Table 5 and methods listed in chapter 5.1.3.

Table 5: Aquifer properties used by the analytical multi-borehole model and numerical multi-borehole model.

Shared Model Characteristics	Constants	Units
Porosity	0.1	Unitless
Rock heat capacity	1000	J/kg°C
Rock grain density	2650	kg/m^3
Wet thermal conductivity (λ_{wet})	2.5	W/m°C
Dry thermal conductivity (λ_{dry})	1	W/m°C
Permeability (vadose model)	$1x10^{-13}$	m^2
Permeability (saturated model)	$1x10^{-15}$	m^2

The aquifer material characteristics of the paired analytical and numerical models were identical when possible, listed in Table 5. The saturated numerical model, intended to represent the analytical model identically, had an isotropic permeability of $1x10^{-15}$ m^2 to reduce density-driven flow, which the analytical model cannot replicate. The partially saturated numerical model with a vadose zone had a mo permeability of $1x10^{-13}$ m^2 with a porosity of 0.1 representing the claystone and partially cemented limestone beneath the CDOT TISR site (Personal communication, Randahawa, September 2020).

A hypothetical fluctuating heat flow was used to heat the models, shown in Figure 35.

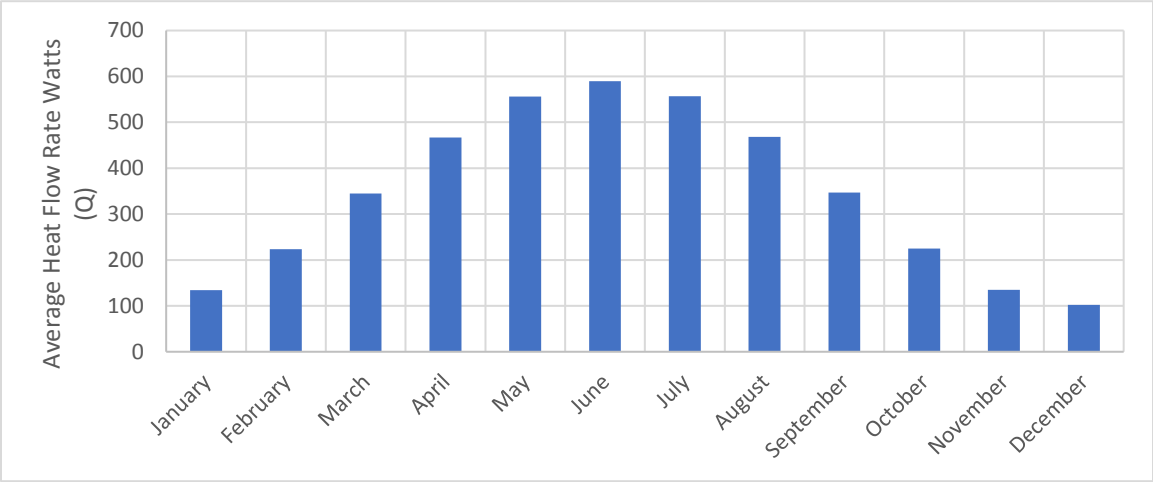

Figure 35: Monthly heat flow rates used to simulate seasonal heat flow in the multi-borehole models.

The heat flow rate (Q) was assigned to each borehole heat exchanger, changing in monthly intervals. The values were calculated using the solar insolation estimation tool explained in 4.3. The analytical and numerical models ran for three years. The seasonal fluctuations in heat flow from the boreholes were applied constantly as temperature readings at the observation points were taken. The root mean squared error (RMSE) of the analytical model temperatures versus the results from the numerical model was used to assess the model's accuracy.

5.3.2 Results: Comparing Model Cross-Sections

It can be observed that the heat flow from the multiple borehole heaters in the numerical model does not reach the lateral boundary conditions of the model at the peak of borehole heat (Figure 36).

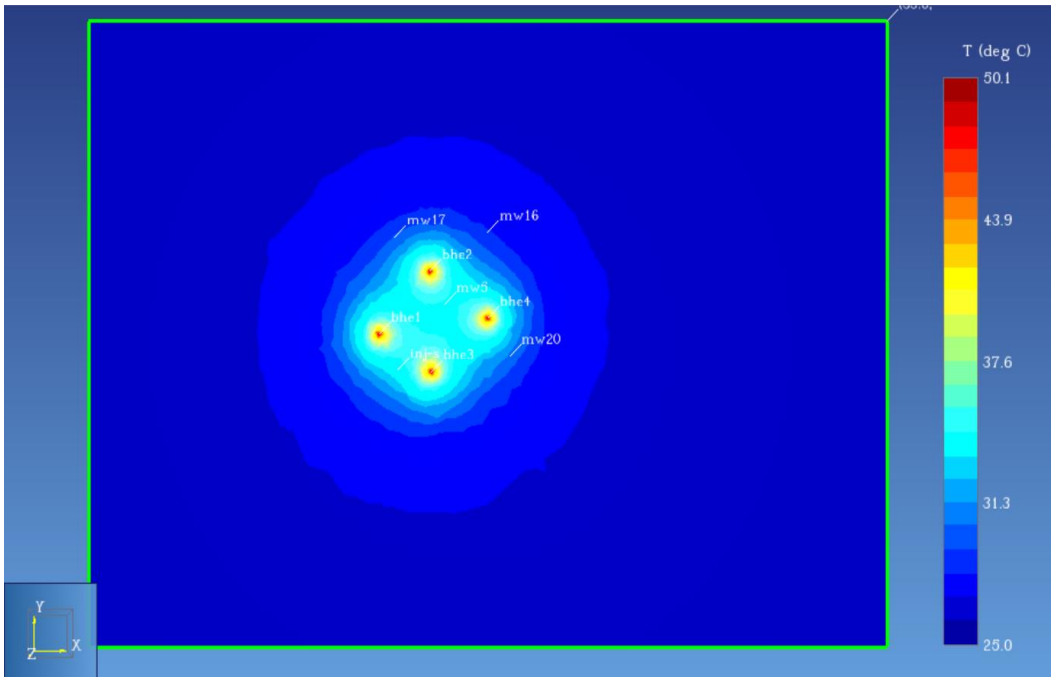

Figure 36: Top-down view of the multi-borehole numerical model at a depth of 7.75 meters. T= 3 years.

Pictured in Figure 37 is an example of the same borehole heat exchanger model calculated and mapped with the analytical solution, displaying similar behavior to the numerical model shown earlier in Figure 36.

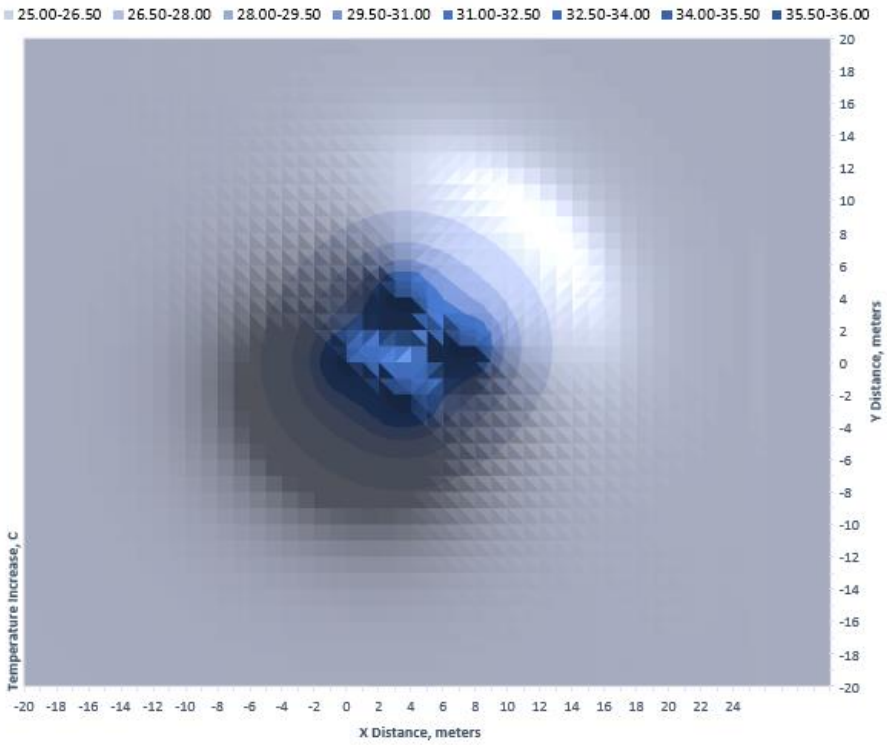

Figure 37: Top-down sliced plane view of the multi-borehole analytical model temperature at a depth of z=7.75. T = 3 years.

While the analytical model may appear to be calculated using finite grids like a numerical model, the temperature output from the analytical models is actually a series of analytical calculations used to populate a grid defined by the user, shown in the temperature contour plots from the analytical model (Figure 37). The cross-sectional view of heat from the numerical model shown in Figure 38 shows how the surface fixed temperature boundary condition influences the shape of the heat plume in the multi-borehole model.

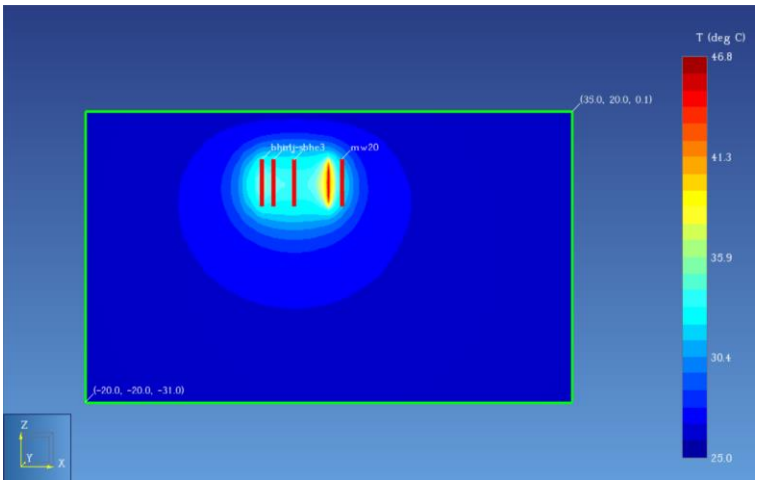

Figure 38: Cross-sectional side view of the multi-borehole numerical model temperature at y=1. T = 2 years. (Temperature appears pronounced where the cross-section intersects BHE4 and not the other boreholes, which are offset.)

The plume of heated water modeled by the analytical model in the multi-borehole scenario (Figure 39) produced similar results to the previously mentioned numerical model (Figure 38), showing that the analytical model works as expected when plotting multiple borehole heat exchangers at once using superposition described in chapter 3.4.

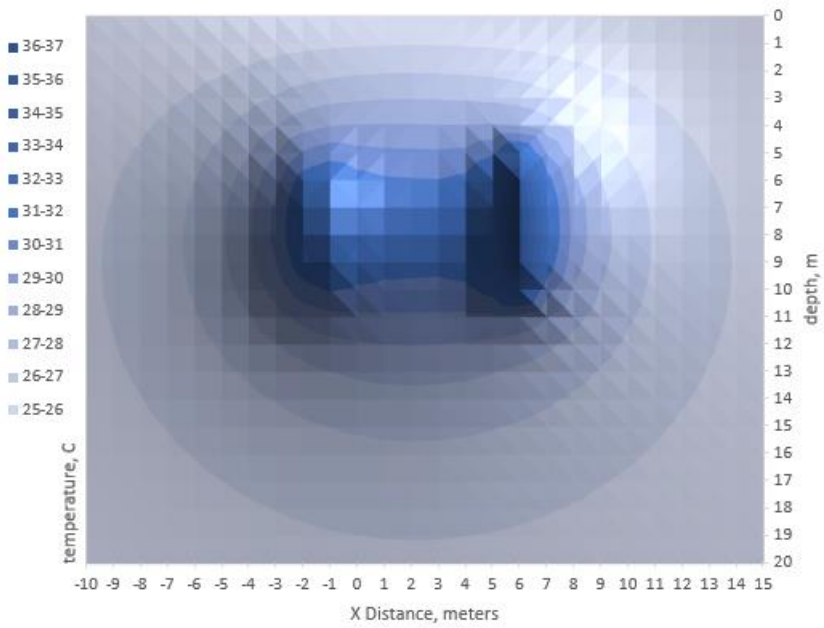

Figure 39: Cross-sectional side view of the multi-borehole numerical model temperature at y=1. T = 3 years created using the analytical model. (Temperature appears pronounced where the cross-section intersects BHE4 and not the other boreholes, which are offset.)

5.3.3 Results: Identical Models

NRMSEs of analytical vs numerical temperatures normalized over the range, shown in Figure 40, were: A) 3.4%; B) 2.9%; C) 2.7%; D) 3.0%; E) 3.7% .

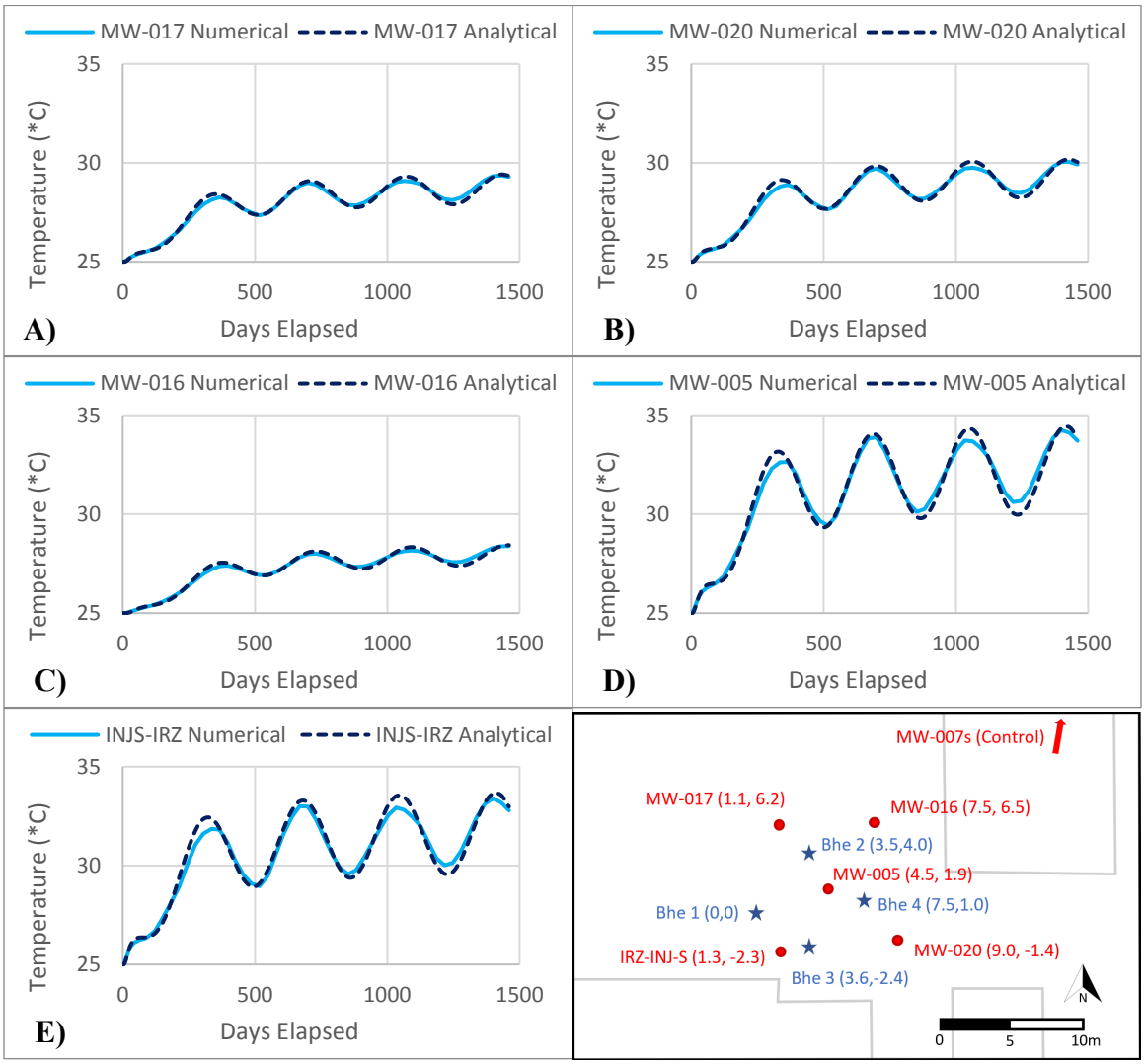

Figure 40: Comparison of temperature over time in the analytical multi-borehole model and saturated numerical multi-borehole model.

5.3.4 Results: Saturated Analytical Model vs. Partially Saturated Numerical Model

NRMSEs of analytical vs numerical temperatures normalized over the range, shown in Figure 39, were: A) 3.2%; B) 2.7%; C) 2.6%; D) 2.8%; E) 3.5% .

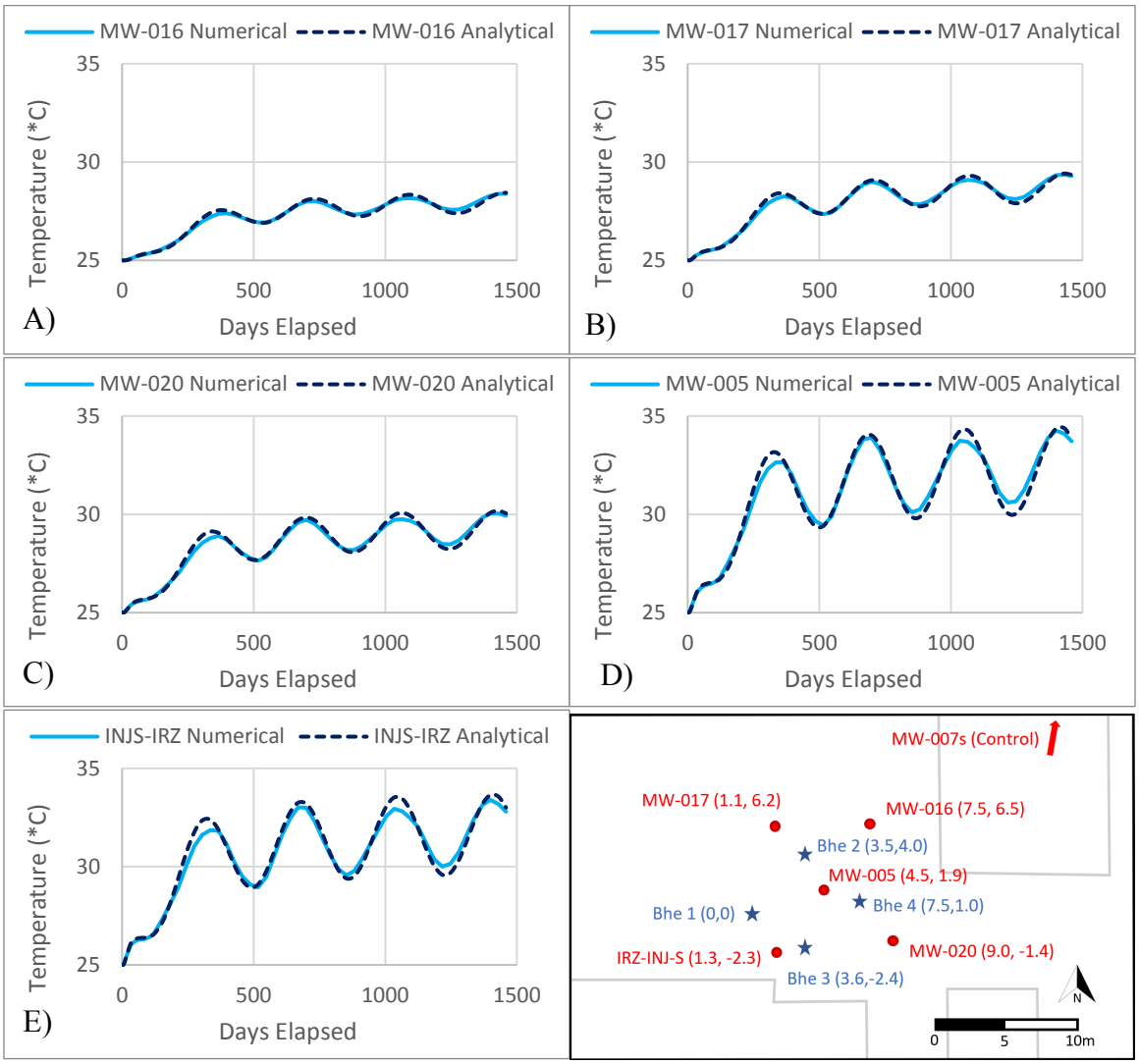

Figure 41: Comparison of the temperature over time of the analytical multi-borehole model and the numerical multi-borehole model with 5m vadose zone.

5.4 Conclusions

In chapter 5, the objective was to compare the analytical model to various hypothetical situations created with the TOUGH EOS1 & EOS3 codes in order to validate the analytical solution. By comparing the analytical model to the aforementioned TOUGH codes, it validates that the analytical model can produce similar results to accepted numerical modeling methods. Creating an easy-to-use modeling tool with capabilities similar to more complex numerical modeling strategies enables faster installation of remediation systems, and cleaning contamination sooner, and benefiting society as a whole.

The first step taken was to evaluate the accuracy of the base equation used to dictate the analytical model (chapter 3.3). By comparing the analytical model to an identical saturated numerical model in chapter 5.1.2, the analytical model was shown to produce near-identical results to the TOUGH2 EOS1 solution (Pruess, 1999). With NRSMEs of the analytical model versus numerical model all below 2% (Figure 16), it was shown the underlying analytical solution for heat flow from a finite line source with an atmospheric boundary condition in 3-dimensions (expressed by equation 8) functions as intended.

The second step was to assess the accuracy of the analytical model when attempting to simulate aquifers with unsaturated zones (chapter 3.6), despite the model's assumption that the aquifer is of uniform thermal conductivity. When modeling partially unsaturated aquifers, the analytical model continued to produce results similar to the numerical model in chapter 5.1.4. The NRMSEs in these test cases at all observation

points stayed below 10% (Figure 22), with the heat plumes in the analytical and numerical model resembling each other (Figure 42). This accuracy between the analytical model and numerical model indicated that the analytical model's underlying solution remains valid in real-world scenarios which may have partially saturated conditions.

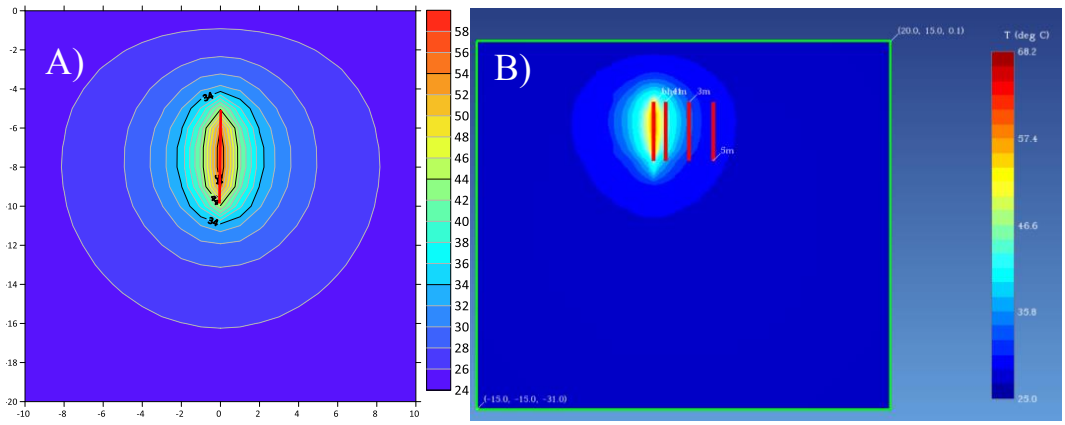

Figure 42: Comparison of thermal plume contours viewd in a side cross-section of the heat plume created by the analytical model assuming homogenous conditions A) and the numerical model B) with a vadose zone directly above the borehole heater, represented by the red lines.

The third step in testing the analytical model was assessing where the model's inability to model natural convection became a noticeable source of error. In scenarios where the aquifer exhibits permeabilities similar or greater than that of course sand or gravel ($K > 1x10^{-4}$ m/s) it was shown in chapter 5.1.6 that natural convection, or density driven flow, becomes a major source of vertical heat movement that the analytical model cannot account for (Figure 25) compared to the TOUGH EOS3 numerical models. In these scenarios the maximum relative error of temperature modeled by the analytical solution reached 90%, suggesting the analytical model is not appropriate for simulating high permeability aquifers (Figure 43).

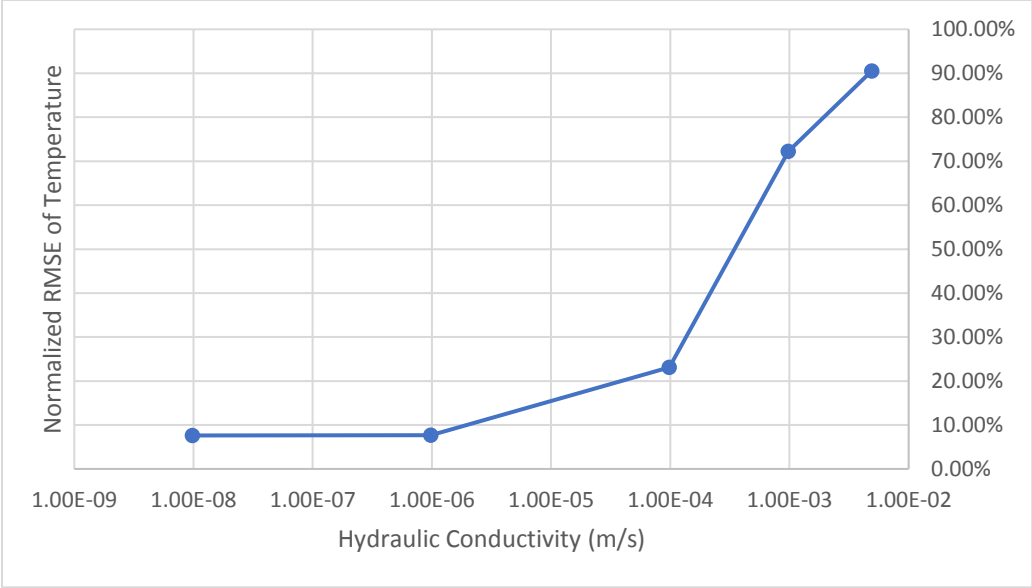

Figure 43: Maximum % error of the analytical model when attempting to model heat flow in increasingly high hydraulic conductivities, ranging from 9.8×10^{-9} to 4.9×10^{-3} m/s with measurements taken 1m from the borehole heat exchanger at its midpoint.

The fourth step of assessing the analytical model was verifying that its function for modeling groundwater flow at any angle worked correctly (chapter 3.7). The analytical model was shown to accurately model the flow of groundwater in chapter 5.2.2 when compared to the numerical model based on TOUGH EOS1. The NRMSE of the observation points in the analytical model with flow compared to an identical numerical flow model observed a maximum NRSME of 6.1% (Figure 33). This low error indicates that the analytical model's ability to simulate the advective transport of heat functions as intended.

The fifth objective towards validating the analytical model was ensuring that the solution for superposition of multiple boreholes (chapter 3.4) and fluctuating rates of heat flow functioned accurately. When the analytical model was compared to the numerical

model in a hypothetical multi-borehole heat exchanger model with changing heat flow, it proved to be accurate. These results, with NRMSE values all below 5% (Figure 40, Figure 41), verified the accuracy of the solution for superimposing temperature to model multiple heaters and the adaption to model heat flow over transient time explained in chapters 3.4 and 3.5.

After testing every aspect of the analytical model against the proven numerical TOUGH2 EOS1, and EOS3 codes, it can be concluded that the analytical function used by the TISR modeling tool works as intended, bearing accurate results in almost all scenarios. The modeling capabilities of the analytical modeling tool stayed within an NRMSEs below 10% in all the scenarios compared to the TOUGH codes throughout chapter 5, with the exception of high permeability aquifer materials. For predicting temperature increases in the subsurface within a general range of 5 to 10 °C, such as needed by TISR systems, the analytical model has been shown to be sufficiently accurate.

6. SIMULATING THE COLORADO DEPARTMENT OF TRANSPORTATION TISR SITE USING THE TISR MODELING TOOL

6.1 Characterization of The CDOT Site

The main reference point for verifying the analytical model against observed readings was the TISR system, named the "Colorado Department of Transportation" site (CDOT) in Denver, Colorado mapped in Figure 44.

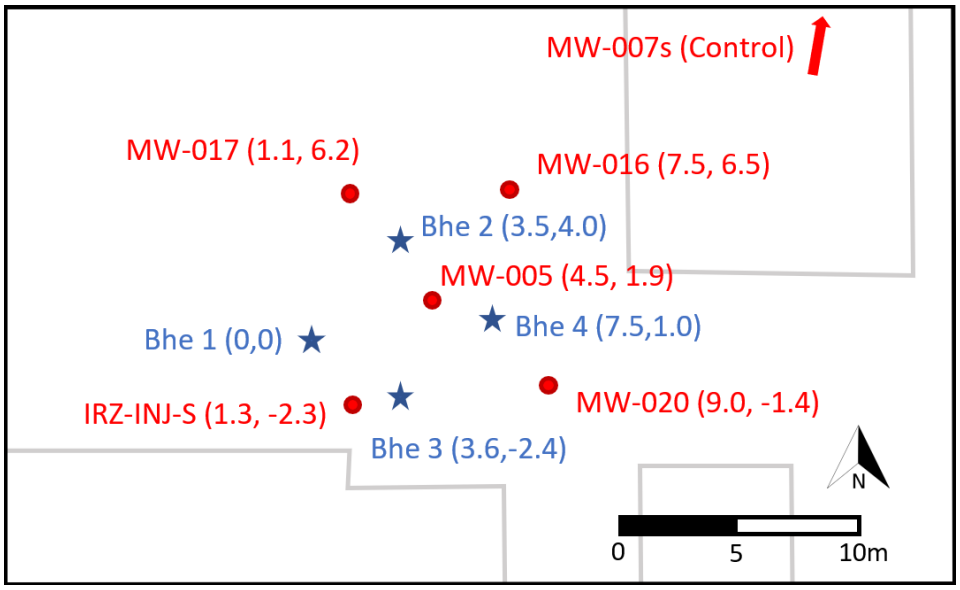

Figure 44: A map of the CDOT TISR site installed by Arcadis. Red dots mark monitoring wells while blue stars indicate borehole heat exchanger placement.

The CDOT site is contaminated with VOCs originating from vehicle maintenance, including the DNAPL trichloroethylene, and was chosen to demonstrate how low-temperature heating would accelerate enhanced biological degradation (Personal communication, Randahawa, September 2020). The CDOT site remediation began in October 2017, with temperature measurements beginning December 2017 available through November 2020. However, borehole heat observations at the CDOT site have gaps in information throughout 2019 when the system went down.

The CDOT site is paved but experiences irregular infiltration from runoff water drains, resulting in fluctuations in the groundwater table and groundwater flow in multiple directions. Average groundwater flow occurs with a Darcy velocity of 0.354 m/yr at an azimuth of 36 degrees after averaging various gradients observed in well logs over time (Personal communication, Randahawa, September 2020). The CDOT site

subsurface is characterized by a 10-foot layer of silt overburden underlain with a bedrock of low permeability compacted claystone and relatively impermeable cemented sandstone layers (Personal communication, Randahawa, September 2020). The borehole heat exchangers are completely submerged below the groundwater table, which remains at a depth of approximately 10 feet. Based on the information from Dalla et al., (2020), "An updated ground thermal properties database for GSHP applications," a useful source for finding wet thermal conductivity of all subsurface materials, it was estimated the average wet thermal conductivity of the aquifer was 2.25 W/m°C. As a heterogeneous aquifer unit with varying sedimentary layers, the CDOT site was thought to be a good test case for assessing the analytical modeling tool's inaccuracies that may stem from assuming a homogenous subsurface.

Subsurface temperature readings from the CDOT monitoring wells were taken from automatic loggers submerged in monitoring wells. The temperature readings from the CDOT site were then used to calculate the increased aquifer temperature over ambient conditions, referred to as Delta T (Figure 45).

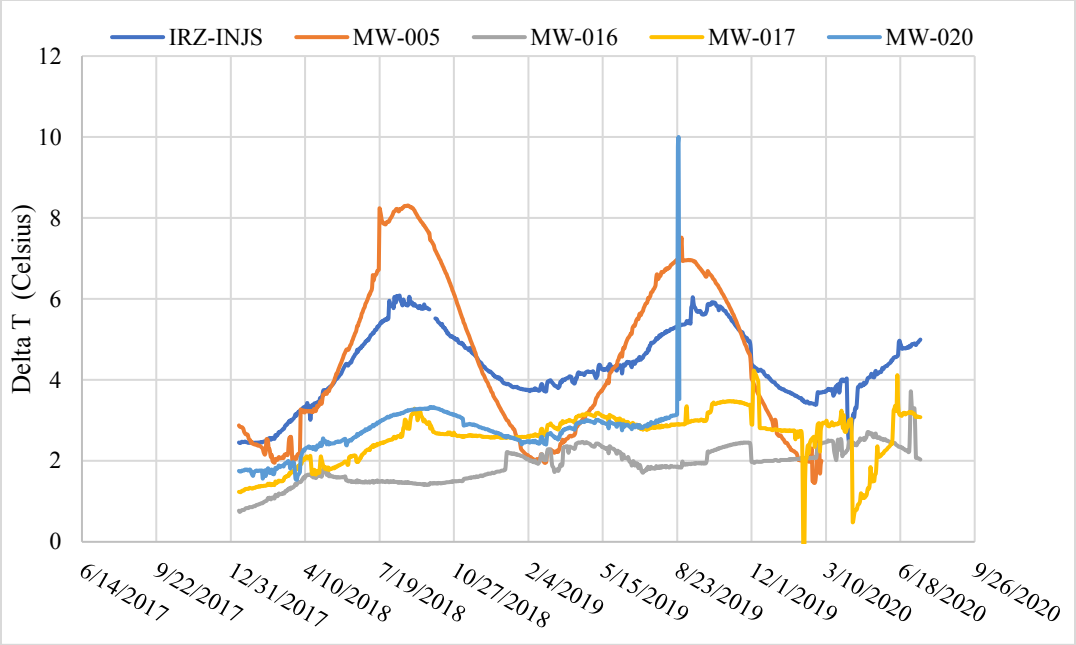

Figure 45: Observed increase in temperature over the ambient subsurface temperature at the CDOT site.

MW-007, a monitoring well placed off-site, functioned as the control for ambient subsurface temperature. Temperature readings began two months after the CDOT TISR system began operating in mid-September (Personal communication, Randahawa, September 2020).

The CDOT site is located at 44 degrees latitude with a recorded global tilted irradiance of 5.8 kWh/m^2/d (Global Solar Atlas, 2021). Two 30-tube array, evacuated solar tube collectors were used to heat a propylene glycol working fluid which was distributed to the borehole heat exchangers with a single pump that turned on and off intermittently for various reasons, operating an average of 30% of the day. The CDOT site has four 5-meter helical thermal borehole heat exchangers, denoted BHE 1, 2, 3, and 4 (Figure 44). The heat exchanger boreholes were placed in 8-inch wells and buried at the

top of the heating element depth of 5m, with the cavity being filled with #1 silica sand (Personal communication, Randahawa, September 2020).

6.2 Methods

6.2.1 Calculating Actual Heat Flow (Q) from CDOT Site

The monthly average heat flow released from a single borehole was calculated using manually collected system data from the CDOT TISR site and the solution for calculating average heat flow in chapter 4.2.

Days with multiple readings were combined into daily averages, with outlying data, such as unrealistic pump rates attributable to human measurement error, were omitted. For days missing flow rate readings while the system was still operating, it was assumed the mass flow rate was the average rate, 0.1 kg/s.

The daily heat flow rates were calculated from each borehole outlet and the pump inlet and combined to find a daily average heat flow rate in Watts per borehole. Once calculated, the daily heat flow averages were intermittent with significant gaps, making the raw data unusable for modeling purposes. To acquire a complete monthly heat flow rate for use with the analytical model, the daily rates were interpolated (Figure 46) using the Loess smoothing method (Jacoby, 2000), alternatively known as Savitzky-Golay processing.

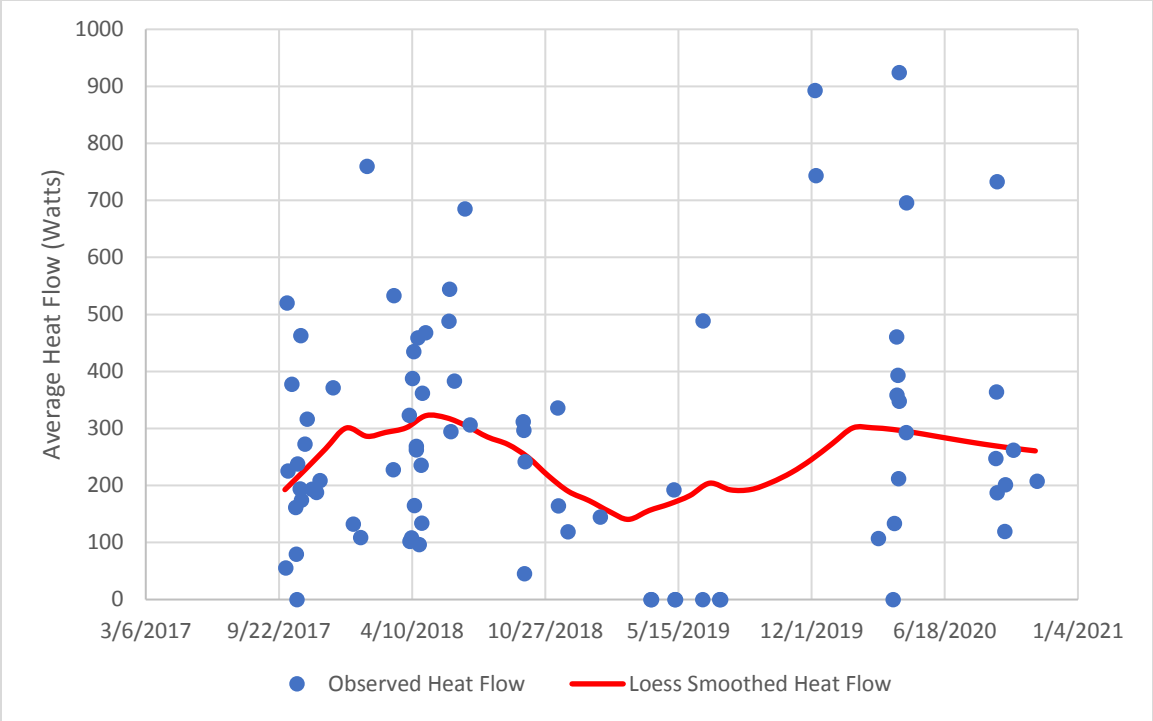

Figure 46: The average daily rate of heat flow from a single borehole at the CDOT site calculated from observed data (when available) and a smoothed monthly heat flow rate (in red) used for modeling purposes.

The interpolated monthly Q rates were then used in the analytical model. The actual heat flow of a single borehole heat exchanger at the CDOT site, after Loess smoothing, was calculated to be on average 235 watts over the lifespan of the system.

6.2.2 Estimated Heat Flow (Q) Using the Solar Insolation Tool

Using the solar insolation tool, the average heat flow of a single borehole at the CDOT site was predicted to be 239 watts, 4 watts higher than the actual heat flow calculated in 6.2.1. The monthly heat flow rates used in the analytical model to reproduce the CDOT site are shown in Figure 47.

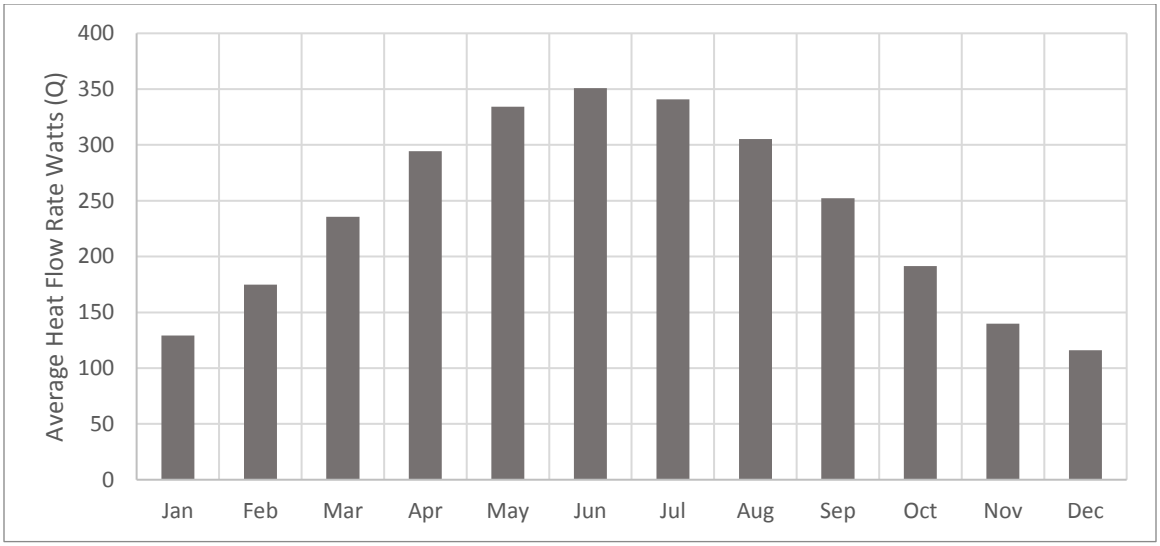

Figure 47: Monthly average heat flow rates (per borehole) used to operate the CDOT site model calculated from solar insolation.

6.2.3 Simulating the CDOT Site with the TISR Modeling Tool

The analytical model was set up to resemble the CEOT site and use the heat flow rates from the CDOT site calculated in chapters 6.2.1 and 6.2.2. These simulated temperature increases predicted with the analytical model were then compared to the observed temperature increases at the CDOT site to assess the validity of the modeling tool in a real-world scenario.

The first model of the CDOT site used the observed monthly heat flow rate taken from observations taken at the CDOT site, expanded upon in chapter 6.2.1.

The second model of the CDOT site used the estimated heat flow from the solar insolation tool, calculated in 6.1.3, such as would be done in the pre-planning of solar borehole installation. This second test assessed the model's accuracy while using the solar

insolation tool, seeing whether the method could reliably predict potential borehole heat exchanger performance.

The analytical model of the CDOT site was set up using the values of aquifer material listed in Table 6 and was defined using the coordinates listed in Table 7.

Table 6: Aquifer properties used by the analytical model to simulate the CDOT site.

Shared Model Characteristics	Constants	Units
Porosity	0.4	Unitless
Rock heat capacity	790	J/kg°C
Rock grain density	2200	kg/m^3
Thermal conductivity (λ_{wet})	2.25	W/m°C

Table 7: Coordinate system used to model the CDOT Site, map of the CDOT site can be seen in Figure 44.

ID	X (meters)	Y (meters)
BHE-01	0.00	0.00
BHE-02	3.51	4.04
BHE-03	3.58	-2.36
BHE-04	7.54	0.99
Mw-005	4.50	1.91
Mw-016	7.54	6.48
Mw-017	1.14	6.25
Mw-020	8.99	-1.45
INJ-S	1.30	-2.29

A darcy velocity of 0.354 m/year at an azimuth of 36 degrees was put into the model. An example of the analytical model user interface is shown in Figure 48.

3D Analytical solution for borehole heat exchanger with regional GW flow								1095	
Ron Falta 2/14/2021	Run Program				heater		N obs loc	5	
Darcy velocity	0	m/yr	month	months	Q (Watts)		xobs	yobs	zobs
number of heaters	4	unitless	January	10	192.669		4.4958	1.905	7.5
Background T	0	C	February	11	228.568		7.5438	6.477	7.5
porosity	0.4	unitless	March	12	264.301		1.143	6.2484	7.5
Rock heat capacity	790	J/kg*C	April	1	300.788		8.9916	-1.4478	7.5
Rock grain density	2200	kg/m^3	May	2	286.273		1.2954	-2.286	7.5
Thermal conductivity	2.25	W/m*C	June	3	293.072				
Heater length	5	m	July	4	301.187				
depth to top of heater	5	m	August	5	322.582				
Snapshot flag yes=1, no=-1	-1.0		September	6	318.609				
xmin	-25	m	October	7	304.298				
xmax	25	m	November	8	285.218				
ymax	15	m	December	9	271.97				
ymin	-25	m	January	10	249.573				
dx	1	m	February	11	216.584				
dy	1	m	March	12	189.483				
z for xy plot	9	m	April	1	173.337				
y for xz plot	0	m	May	2	153.939				
zmin	0	m	June	3	140.586				
zmax	-20	m	July	4	156.141				
dz	1	m	August	5	167.429				
N Gauss (integration)	16		September	6	182.138				
Flow direction angle	45	degrees	October	7	204.062				
t start, day of year	1	days	November	8	192.348				
t end, days since start	1140	days	December	9	193.003				
delta t for time series	1	days	January	10	205.167				
heater data			February	11	222.96				
x (m)	y (m)		March	12	245.63				
0	0		April	1	273.35				
3.5052	4.0386		May	2	301.001				
3.5814	-2.3622		June	3	301.235				
7.5438	0.9906		July	4	298.261				
			August	5	293.205				
			September	6	287.095				
			October	7	281.039				
			November	8	275.060				

Figure 48: Graphical user interface of the TISR modeling tool exhibiting parameters used to model the CDOT site analytically.

6.3 Results

After using the heat flow values observed at the CDOT site to simulate the CDOT site itself with the analytical modeling tool, the temperatures calculated by the model were compared to the observed site data using the RMSE normalized over the range of the observed values (Figure 49). NRMSEs of the observation wells were: A) 25.0%; B) 13.4%; C) 14.2%; D) 5.5%; E) 21.6%. The maximum errors in temperature from modeled to observed, in degrees C, were: A) 7.2; B) 2.63; C) 3.67; D) 4.0; E) 6.58.

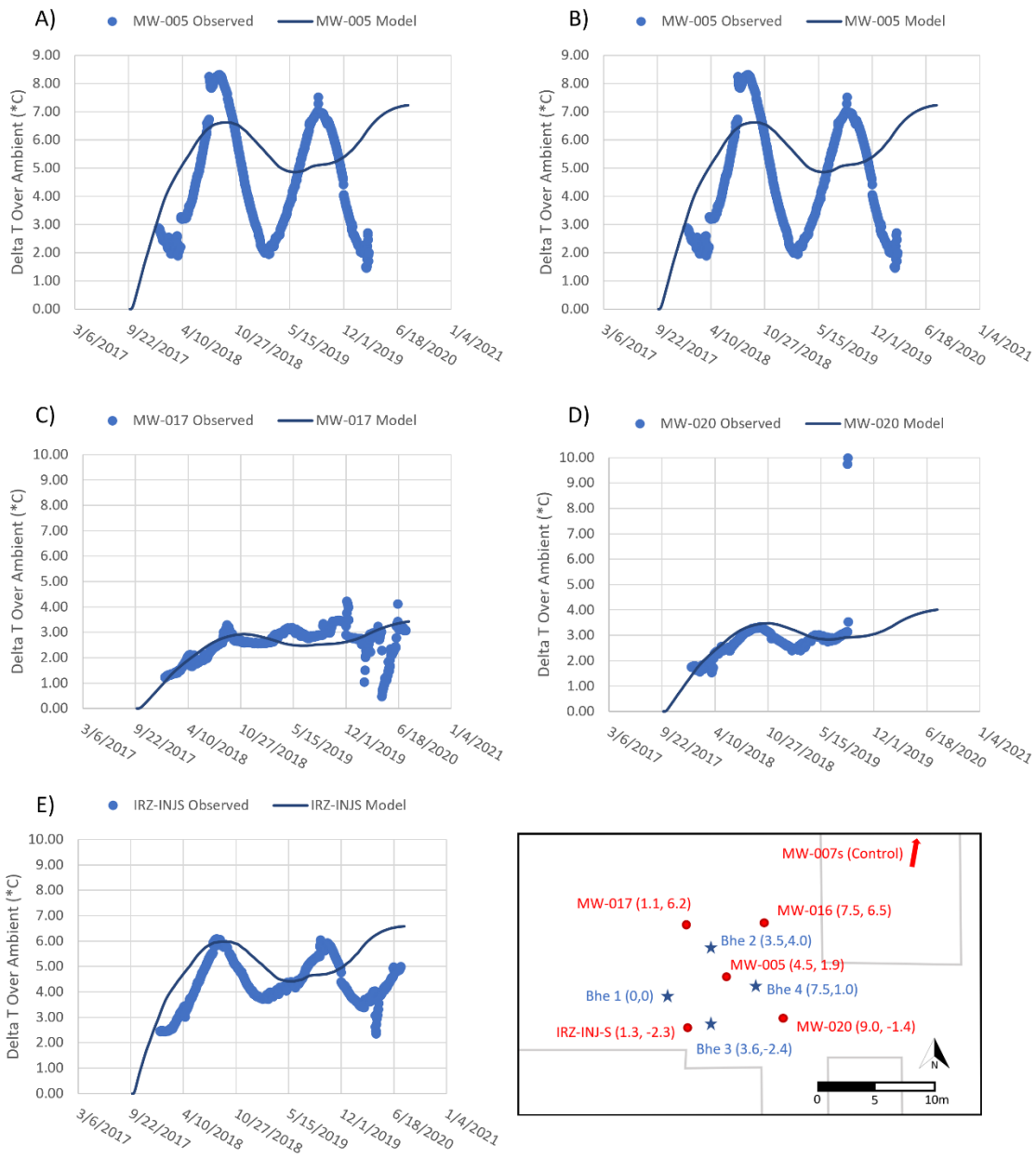

Figure 49: Comparison of temperature over time predicted by the analytical model using calculated heat flow from the CDOT site versus actual observed temperatures. Temperatures taken at z=7.75m depth.

Using the heat flow values from the solar insolation tool, the temperatures calculated by the model were compared to the observed site data using the RMSE normalized over the range of the observed values (Figure 50). NRMSEs of the observation wells were: A) 19.3%; B) 16.8%; C) 12.5%; D) 4.3%; E) 15.7%. The maximum errors in temperature from modeled to observed, in degrees C, were: A) 7.4; B) 2.5; C) 3.5; D) 4.0; E) 6.8.

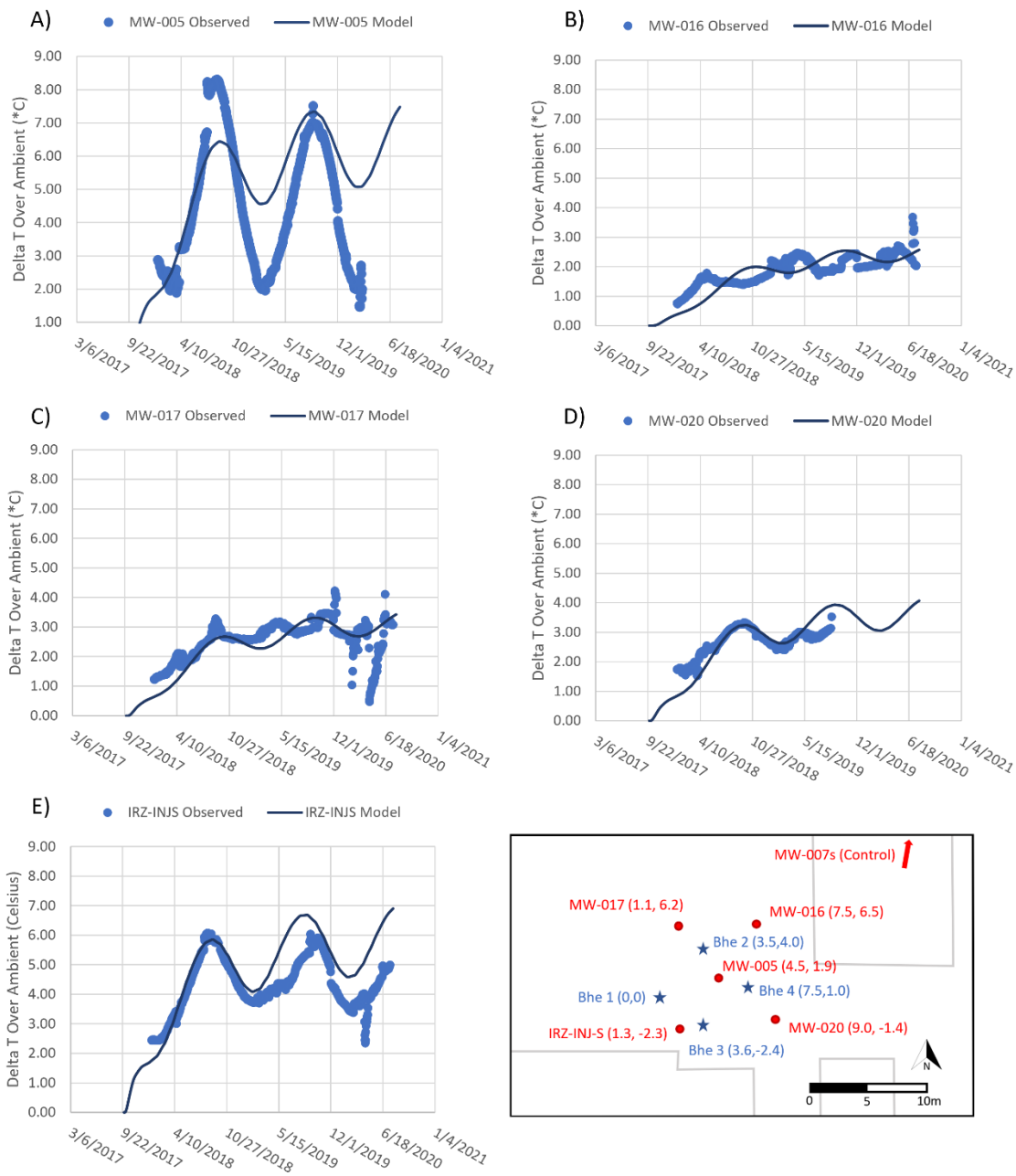

Figure 50: Comparison of the temperature over time predicted by the analytical model using estimated heat flow using the solar insolation heat flow calculator versus actual observed temperatures at the CDOT site.

6.4 Conclusion

In comparing the actual observed data from the CDOT site to the analytically modeled simulation of the CDOT site, it was possible to quantify the accuracy of the modeling tool in a real-world scenario. The strong performance of the analytical model in simulating the CDOT site is a promising sign the analytical modeling tool is fairly accurate even when modeling real-world conditions with various heterogeneities. The analytical model seems to be a promising tool for quickly designing solar borehole heat exchanger systems.

The solar insolation heat flow tool estimated an average heat flow power of only four watts out higher than the calculated annual heat flow rate of 235 watts observed at the CDOT site itself.

Both of the analytical models, one operating from estimated heat flow from solar insolation and the other operating from calculated heat flow from the CDOT system, predicted the temperatures at monitoring well temperatures at a cumulative overage NRMSE of 10%. In the most extreme case, the analytical model based on calculated heat flow simulated temperatures with an NRMSE of 25% (Figure 51), while the analytical model based on estimated heat flow from solar insolation had an NRSME of 19%.

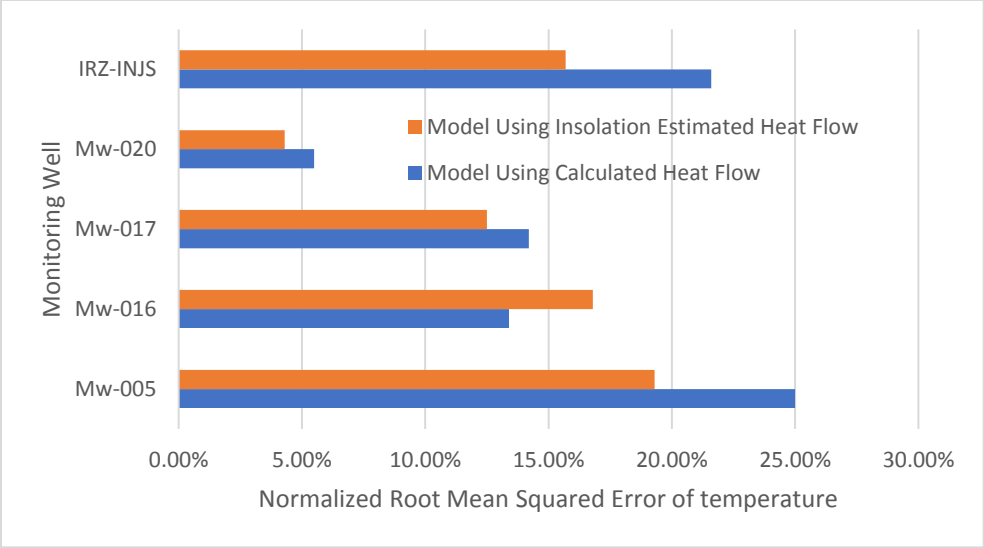

Figure 51: Normalized RMSEs comparing modeled temperatures of the two CDOT models versus the actual observed temperatures from the CDOT site.

Since the desired range of temperature increase desired from a TISR system is within a range of 10 to 20 degrees Celsius, even the maximum error of 25% would be within an acceptable range for modeling TISR systems, suggesting the analytical model is sufficiently accurate even in real-world modeling scenarios.

Unexpectedly, the model using calculated heat flow rates based on measurements from the CDOT site system was shown to be less accurate than the model using estimated heat flow from solar insolation. This lower accuracy is likely due to the noise in the temperature and flow measurements at the site. The model based on estimated solar insolation was more accurate in tracking seasonal fluctuations and more accurate in general, with an average NRMSE of 14% versus 16% from the model using calculated heat flow (Figure 49, Figure 50).

Errors in modeled temperature versus observed temperatures could be attributed to many factors. There could be errors stemming from inaccurately predicting or calculating heat flow from the CDOT site. Assumptions made by the user about the subsurface characteristics such as porosity, rock grain density, and heat conductivity of the subsurface could also be responsible for inaccuracies in simulated temperatures compared to the observed temperatures. Finally, errors could also be attributed to the model itself, which does not account for natural convection and assumes homogenous conditions. In future work, it would be desirable to conduct a solar borehole heat exchanger test with continuous measurement of flow and temperatures at the heat exchangers.

It is also worth mentioning that the temperature recordings from the CDOT site were taken from standing water in groundwater wells, leading to a degree of uncertainty on the accuracy of the observed temperature data itself.

7. MEXICO SITE SIMULATION

7.1 Background

The "Mexico site" is a confidential location in the Tlaxcala region of Mexico used as a pilot study for TISR systems by Arcadis. Relative to the CDOT site, which aimed to moderately increase heat to aid enhanced biological remediation, the Mexico site sought to increase subsurface temperatures by 10 to 15 degrees Celsius for multiphase extraction. The higher degree of temperature change is designed to raise the Henry's constant of VOC contaminants to improve multiphase extraction (Personal communication, Randahawa, July 2021).

The Mexico site began operation in mid-2018 with manually collected data available through November 2019. Relative to the CDOT site, the data set is limited in scope and fragmented due to operating issues with the TISR system for the first six months of use. The observed temperature change (Delta T) resulting from borehole heat exchangers at the Mexico Site was estimated by subtracting the measured temperatures from the initial temperature (Figure 52).

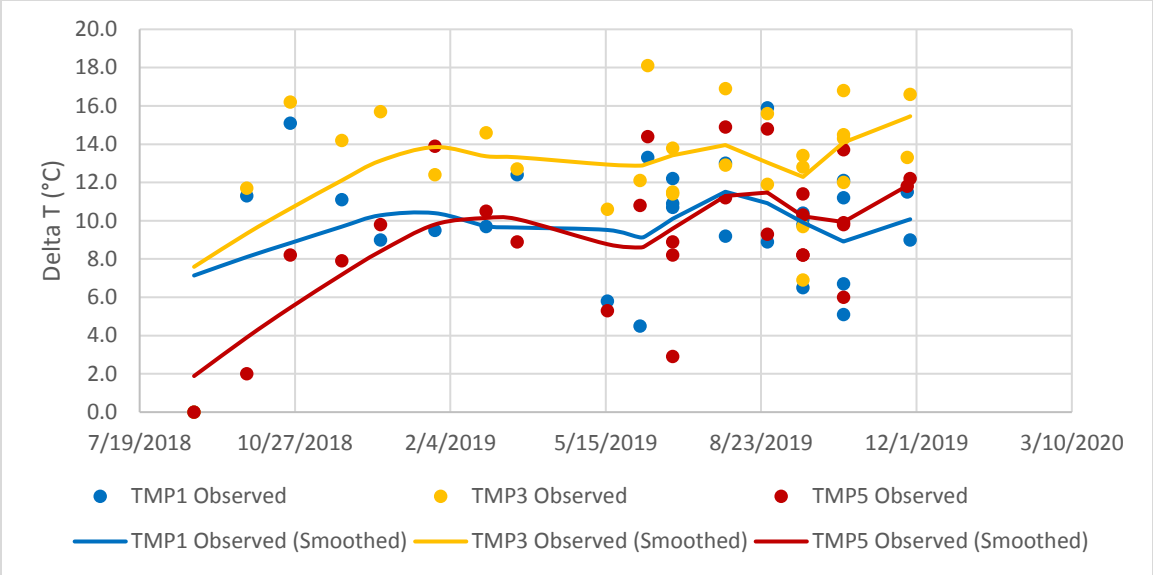

Figure 52: Measured increases in temperature at the Mexico Site after TISR system installation.

Noise from temperature readings taken at the Mexico Site was smoothed using the Loess method (Jacoby, 2000) to make the data usable for RMSE comparison with model results. There were no thermocouples placed off-site to use as a control for ambient subsurface temperature. TMP1, 3, and 5 were chosen to use because they were the only data sets without unusual anomalies, such as larger negative changes in temperature.

7.2 Methods

In order to model the Mexico site, a map of the location was created. Five borehole heat exchangers were placed at a depth of 5 meters to the top of the 5-meter-long heating elements, using coiled borehole heat exchangers (Personal communication, Randahawa, July 2021). The Mexico site uses four 30-tube evacuated solar collector units and is located at a latitude of 20 degrees with a global tilted irradiance of 6.5 kWh/m^2/d

(Global Solar Atlas, 2021). Thermocouples at depths of 5m were used to measure subsurface temperature at this site.

The borehole heat exchangers and thermal monitoring probes were mapped and added to a coordinate system to recreate a model of the Mexico Site, pictured in Figure 53. TMP1, TMP3, and TMP5 were chosen as observation points to be placed in the model because of their varying distance from the borehole array, while other thermocouple readings did not appear to be usable data, at times claiming negative rates of temperature increase over time.

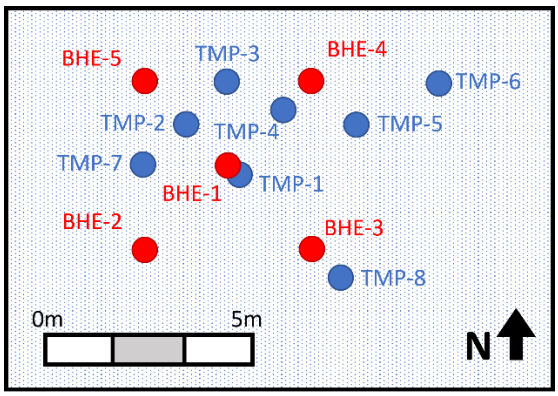

Figure 53: A map of the Mexico site layout. Borehole heat exchangers are represented as red dots, while blue dots represent the thermocouples.

Coordinates of the boreholes and thermocouples used to map the Mexico site, as well as the aquifer characteristics used to define the subsurface, are available in Table 8. Groundwater flow was not used for modeling Mexico Site.

Table 8: Coordinate system and aquifer properties used to construct the Mexico Site model.

ID	X (meters)	Y (meters)
bhe1	2	2
bhe2	0	0
bhe3	4	0
bhe4	4	4
bhe5	0.07	4
tmp1	2.3	1.8
tmp3	2	4
tmp5	5.2	2.9
Model Characteristics	**Constants**	**Units**
Porosity	0.4	Unitless
Rock heat capacity	1000	J/kg°C
Rock grain density	2500	kg/m^3
Thermal conductivity	**2**	W/m°C

The heat flow values used with the TISR Modeling Tool in the simulation are pictured in Figure 54.

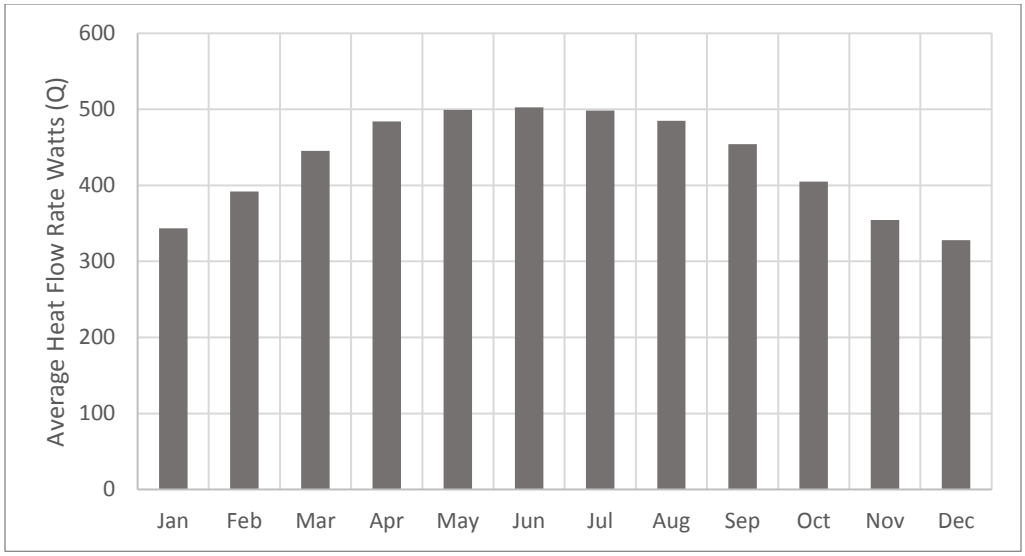

Figure 54: Monthly average heat flow rates (per borehole) used to calculate the heat flow in the Mexico Site model.

Given the Mexico site is 20 degrees from the equator, has twice as many solar collectors as the CDOT site, and experiences greater solar insolation, heat flow is higher and experiences less drastic seasonal fluctuations than the CDOT model. The model ran from July-2018 through December-2019 to match the dates with available measured data.

7.3 Results

Using the heat flow values from the solar insolation tool, the temperatures calculated by the model were compared to the observed Mexico site data using the RMSE normalized over the range of the observed values (Figure 55). NRMSE of the modeled temperatures versus smoothed temperatures were: A) 30%; B) 30%; C) 20%. The maximum errors in temperature from modeled to observed, in degrees C, were: A) 4.8; B) 7.6; C) 4.8.

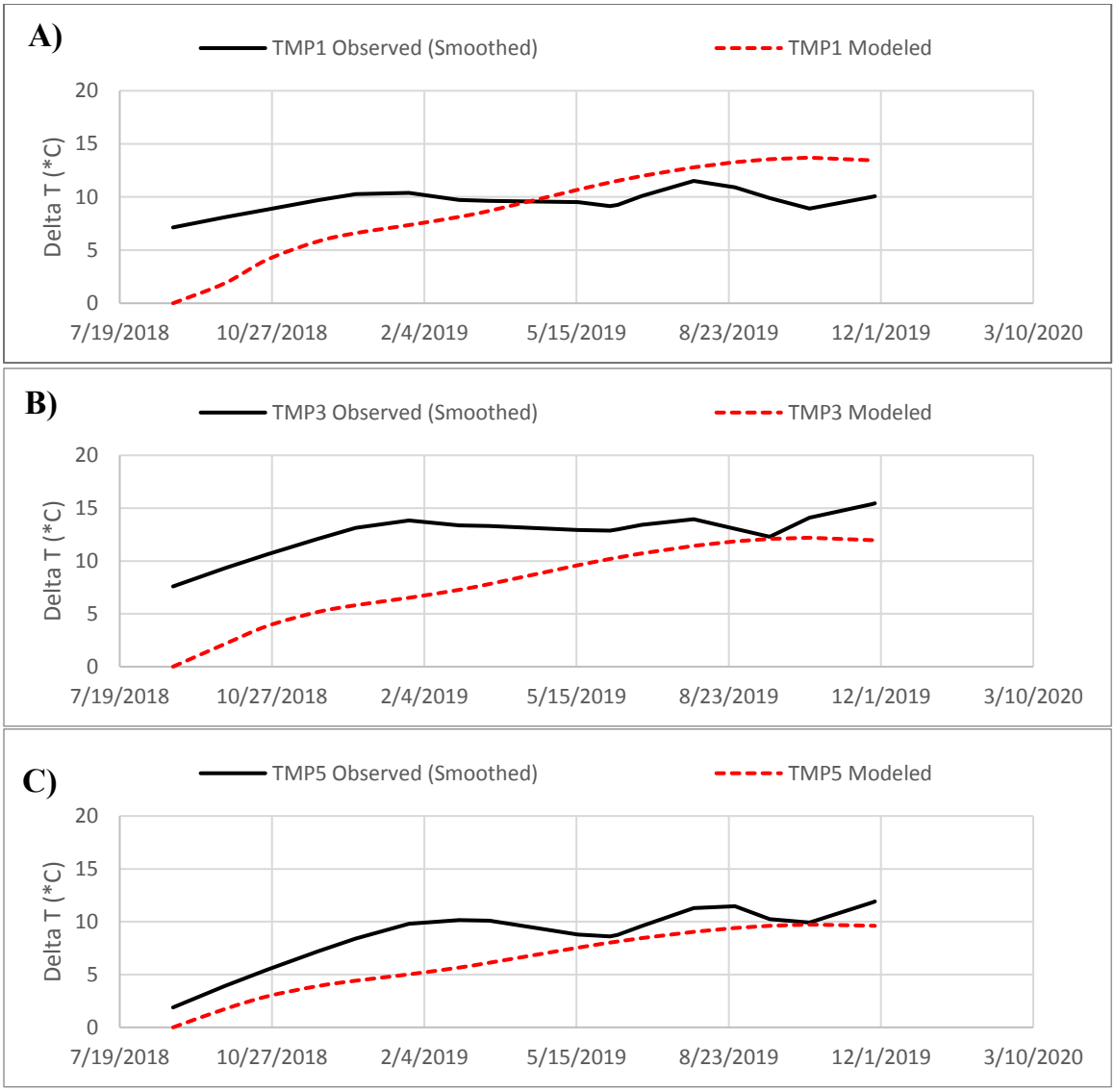

Figure 55: Comparison of the temperature over time predicted by the analytical model versus actual observed temperatures at the Mexico Site. Temperatures were taken at z=5m depth.

7.4 Conclusion

The modeled results at the Mexico site are somewhat unclear because the initial observed data from the site are noisy, meaning assumptions were made about the observed temperatures.

Visually, the temperatures predicted by the analytical model using the solar heat flow calculator appear to match the temperatures recorded at the Mexico site reasonably well (Figure 55). With the lowest NRMSE of temperature versus observed at a 20% error and the highest at 30%, the model is reasonably accurate in this scenario given the uncertainties and noise in the data. It is hard to be certain whether these errors are meaningful given the noisy temperature dataset, which could be unrepresentative of the actual temperatures observed at the site. In future projects, it would be beneficial to collect data that would allow precise calculation of observed heat flow from the borehole heat exchangers to further calibrate the modeling tool.

Given the Mexico site TISR systems' objective was to raise the temperature 10 to 15 degrees Celsius, this model, despite its relative inaccuracies, would still be useful in planning a site with a broad heat range such as that. If this model were to estimate a temperature of 12.5 degrees Celsius with a potential error of ± 20%, it would fall roughly within the desired 10 to 15-degree temperature range.

In the case of estimating the number of solar collectors required to heat the subsurface or doing preliminary planning for a borehole heat exchanger layout, the analytical model appears as though it would still be helpful in this scenario despite the larger apparent error.

8. FINAL CONCLUSIONS

The analytically based TISR modeling tool is quick to use while still offering 3-dimensional modeling capabilities normally associated with numerical models. In various tests comparing the analytical solution to numerical models and TISR field sites, it was shown the model functions as intended:

- It was shown that the analytical solution to 3-dimensional heat propagation in the subsurface functions as intended, recreating models comparable to paired numerical models created with the TOUGH2 EOS1 code.
- The analytical model's novel abilities to simulate multiple boreholes, groundwater flow, and apply variable heat flow rates over time in 3-dimensions were also proven to be accurate compared to the numerical models created with the TOUGH2 EOS3 code.
- The analytical model may struggle with modeling aquifer with hydraulic conductivity in excess of $1x10^{-3}$ m/s due to its' inability to model natural convection.
- When used to simulate the CDOT and Mexico field sites, the analytical model was shown to reasonably reflect the observed subsurface temperature increases at the two locations.
- The Excel modeling tool for modeling thermal boreholes is a user-friendly tool for designing low-temperature solar borehole heat exchanger array.

REFERENCES

Anderson, Mary P. Woessner, William W. Hunt, Randall J.. (2015). *Applied Groundwater Modeling - Simulation of Flow and Advective Transport (2nd Edition) - 2.1 Modeling Purpose.* Elsevier.

Carrier III, W. D. (2003). Goodbye, hazen; hello, kozeny-carman. *Journal of geotechnical and geoenvironmental engineering*, *129*(11), 1054-1056.

Chen, F., Freedman, D. L., Falta, R. W., & Murdoch, L. C. (2012). Henry's law constants of chlorinated solvents at elevated temperatures. *Chemosphere (Oxford)*, *86*(2), 156–165.

Da Conceição Cunha, M. (2002). Groundwater cleanup: The optimization perspective (a literature review). *Engineering Optimization*, *34*(6), 689-702.

Dalla Santa, G., Galgaro, A., Sassi, R., Cultrera, M., Scotton, P., Mueller, J., ... & Bernardi, A. (2020). An updated ground thermal properties database for GSHP applications. *Geothermics*, *85*, 101758.

Den Iseger, P. (2006). Numerical transform inversion using Gaussian quadrature. *probability in the Engineering and Informational Sciences*, *20*(1), 1-44.

Divine, C. (2020). Thermal In Situ Sustainable Remediation (TISR) To Enhanced Biotic and Abiotic Reactions and Accelerate Remediation. Retrieved Oct 28, 2021. https://www.serdp-estcp.org/Program-Areas/Environmental-Restoration/Contaminated-Groundwater/Persistent-Contamination/ER20-5028/ER20-5028 (Full proposal available upon request).

Doty, C. B., & Travis, C. C. (1990). Can contaminated aquifers at superfund sites be remediated. *Environmental Science and Technology ESTHAG,*, *24*(10).

Eskilson, P. (1987). Thermal analysis of heat extraction boreholes.

Evaluation of groundwater extraction remedies. : v.1. (1989). Office of Emergency and Remedial Response, U.S. Environmental Protection Agency.

Falta, R. W., Stacy, M. B., Ahsanuzzaman, N. M., Wang, M., & Earle, R. C. (2007). REMChlor. *Remediation Evaluation Model for Chlorinated Solvents. User's Manual. Version*, *1*.

Florides, G., & Kalogirou, S. (2007). Ground heat exchangers—A review of systems, models and applications. *Renewable energy*, *32*(15), 2461-2478.

Freeze, R. A., & Witherspoon, P. A. (1966). Theoretical analysis of regional groundwater flow: 1. Analytical and numerical solutions to the mathematical model. *Water Resources Research*, *2*(4), 641–656.

Ferguson, G. (2007). Heterogeneity and thermal modeling of ground water. *Groundwater*, *45*(4), 485-490.

Guha, N., Loomis, D., Grosse, Y., Lauby-Secretan, B., El Ghissassi, F., Bouvard, V., ... & International Agency for Research on Cancer Monograph Working Group. (2012). Carcinogenicity of trichloroethylene, tetrachloroethylene, some other chlorinated solvents, and their metabolites.

Global Solar Atlas v2.6 (2021). *Retrieved from* https://globalsolaratlas.info/

Hansen, J., Fung, I., Lacis, A., Rind, D., Lebedeff, S., Ruedy, R., ... & Stone, P. (1988). Global climate changes as forecast by Goddard Institute for Space Studies three-dimensional model. *Journal of geophysical research: Atmospheres*, *93*(D8), 9341-9364.

Hecht-Méndez, J., Molina-Giraldo, N., Blum, P., & Bayer, P. (2010). Evaluating MT3DMS for heat transport simulation of closed geothermal systems. *Groundwater*, *48*(5), 741-756.

Heneghan, A. K. (2000). The Legacy of Woburn, Massachusetts and Trichloroethylene. *Principles of Environmental Toxicology University of Idaho*.

Hird, R., & Bolton, M. D. (2017). Clarification of capillary rise in dry sand. *Engineering Geology*, *230*, 77-83.

Huling, S. G. (1991). *Dense non-aqueous phase liquids / Scott G. Huling and James W. Weaver*. Superfund Technology Support Center for Ground Water, Robert S. Kerr Environmental Research Laboratory, 1991.

Jacoby, W. G. (2000). Loess:: a nonparametric, graphical tool for depicting relationships between variables. *Electoral Studies*, *19*(4), 577-613.

Jo, Y.-J., Lee, J.-Y., Yi, M.-J., Kim, H.-S., & Lee, K.-K. (2010). Soil contamination with TCE in an industrial complex: contamination levels and implication for groundwater contamination. *Geosciences Journal (Seoul, Korea)*, *14*(3), 313–320.

Jung, Y., Pau, G. S. H., Finsterle, S., & Pollyea, R. M. (2017). TOUGH3: A new efficient version of the TOUGH suite of multiphase flow and transport simulators. *Computers & Geosciences*, *108*, 2-7.

Krakauer, N. Y., Li, H., & Fan, Y. (2014). Groundwater flow across spatial scales: importance for climate modeling. *Environmental Research Letters*, *9*(3), 34003–.

Kummu, M., Guillaume, J. H., de Moel, H., Eisner, S., Flörke, M., Porkka, M., ... & Ward, P. J. (2016). The world's road to water scarcity: shortage and stress in the 20th century and pathways towards sustainability. *Scientific reports*, *6*(1), 1-16.

Liu, Q., Yasufuku, N., Miao, J., & Ren, J. (2014). An approach for quick estimation of maximum height of capillary rise. *Soils and Foundations*, *54*(6), 1241-1245.

Macbeth, T., Truex, M., Powell, T., & Michalsen, M. (2012). *Combining Low-Energy Electrical Resistance Heating with Biotic and Abiotic Reactions for Treatment of Chlorinated Solvent DNAPL Source Area*. APPLIED RESEARCH ASSOCIATES INC ALBUQUERQUE NM.

Mackay, D. M., & Cherry, J. A. (1989). Groundwater contamination: Pump-and-treat remediation. *Environmental Science & Technology*, *23*(6), 630-636.

Man, Y., Yang, H., Diao, N., Liu, J., & Fang, Z. (2010). A new model and analytical solutions for borehole and pile ground heat exchangers. *International Journal of Heat and Mass Transfer*, *53*(13-14), 2593-2601.

McDade, J. M., McGuire, T. M., & Newell, C. J. (2005). Analysis of DNAPL source-depletion costs at 36 field sites. *Remediation (New York, N.Y.)*, *15*(2), 9–18.

ModelE AR5 Simulations: Past Climate Change and Future Climate Predictions (2021). *Retrieved from https://data.giss.nasa.gov/modelE/ar5plots/srmonlat.html*

Molina-Giraldo, N., Blum, P., Zhu, K., Bayer, P., & Fang, Z. (2011). A moving finite line source model to simulate borehole heat exchangers with groundwater advection. *International Journal of Thermal Sciences*, *50*(12), 2506–2513

Philippe, M., Bernier, M., & Marchio, D. (2009). Validity ranges of three analytical solutions to heat transfer in the vicinity of single boreholes. *Geothermics*, *38*(4), 407-413.

Pruess, K. (1988). SHAFT, MULKOM, TOUGH: A set of numerical simulators for multiphase fluid and heat flow.

Pruess, K., Oldenburg, C. M., & Moridis, G. J. (1999). *TOUGH2 user's guide version 2* (No. LBNL-43134). Lawrence Berkeley National Lab.(LBNL), Berkeley, CA (United States).

Rahbeh, M. E., & Mohtar, R. H. (2007). Application of multiphase transport models to field remediation by air sparging and soil vapor extraction. *Journal of hazardous materials*, *143*(1-2), 156-170.

Rivett, M. O., Wealthall, G. P., Dearden, R. A., & McAlary, T. A. (2011). Review of unsaturated-zone transport and attenuation of volatile organic compound (VOC)

plumes leached from shallow source zones. *Journal of contaminant hydrology*, *123*(3-4), 130-156.

Roy, J. W., & Bickerton, G. (2012). Toxic Groundwater Contaminants: An Overlooked Contributor to Urban Stream Syndrome? *Environmental Science & Technology*, *46*(2), 729–736.

Seyedabbasi, M. A., Newell, C. J., Adamson, D. T., & Sale, T. C. (2012). Relative contribution of DNAPL dissolution and matrix diffusion to the long-term persistence of chlorinated solvent source zones. *Journal of contaminant hydrology*, *134*, 69-81.

Solar Panels Plus, SPP-30A SRCC Certification. (2020) http://www.solarpanelsplus.com/pdfs/spp30a-srcc.pdf

Solar Panels Plus, SPP Spartan Spec Sheet. (2020)

http://www.solarpanelsplus.com/pdfs/spp-spartanspecs.pdf

Stephens, G. L., Slingo, J. M., Rignot, E., Reager, J. T., Hakuba, M. Z., Durack, P. J., ... & Rocca, R. (2020). Earth's water reservoirs in a changing climate. *Proceedings of the Royal Society A*, *476*(2236), 20190458.

Washington, J. W., & Meiser, E. (1996). Gas partitioning of dissolved volatile organic compounds in the vadose zone: principles, temperature effects and literature review. *Ground Water*, *34*(4), 709–718.

Van Genuchten, M. T. (1980). A closed-form equation for predicting the hydraulic conductivity of unsaturated soils. *Soil science society of America journal*, *44*(5), 892-898.

Yamamoto, H. (2008). PetraSim: A graphical user interface for the TOUGH2 family of multiphase flow and transport codes. *Groundwater*, *46*(4), 525-528.

Zipper, S. C., Gleeson, T., Kerr, B., Howard, J. K., Rohde, M. M., Carah, J., & Zimmerman, J. (2019). Rapid and Accurate Estimates of Streamflow Depletion Caused by Groundwater Pumping Using Analytical Depletion Functions. *Water Resources Research*, *55*(7), 5807–5829.

APPENDIX

(1) Visual Basic solution for modeling thermal heat conduction from borehole heat exchangers used by the analytical model.

```
Sub bhe_solution()
'3D analytical solution for heat conduction from a borehole heat exchanger with convection from
'regional groundwater flow.  Solution adapted from Molina-Giraldo et al. (2011)
'Ron Falta 1/1/2021
'include superposition for multiple heaters
'numerical integration using Gaussian Quadrature with routine adapted from Numerical Recipes book
'
'allow for rotation of flow direction, theta  falta 2/12/21
'theta is angle in degrees of flow direction measured counter-clockwise from positive x-axis
'
'add monthly heat input for heaters; assume same rate for each heater falta 2/14/21
'
'Range clearing subroutine added to avoid issues after overwriting old plots Ornelles 8/10/21

ClearRanges

Dim Q(300), tp(300), x0(200), y0(200), x0p(200), y0p(200), xobs(100), yobs(100), zobs(100) As Double
Dim xgauss1(500), wgauss1(500), xgauss2(500), wgauss2(500) As Double
Dim ngauss As Integer
Dim npstart As Integer
Dim npend As Integer
Dim nobs As Integer
Dim k As Integer
Dim m As Integer
Dim i As Integer
Dim j As Integer
Dim ntobs As Integer
Vd = Cells(3, 2) / 365.25 / 86400#
nheaters = Cells(4, 2)
T0 = Cells(5, 2)
por = Cells(6, 2)
Cr = Cells(7, 2)
rhorock = Cells(8, 2)
lambda = Cells(9, 2)
```

```
d = Cells(10, 2)
dtop = Cells(11, 2)
iflag = Cells(12, 2)
xmin = Cells(13, 2)
xmax = Cells(14, 2)
ymax = Cells(15, 2)
ymin = Cells(16, 2)
dx = Cells(17, 2)
dy = Cells(18, 2)
zz = Cells(19, 2)
yy = Cells(20, 2)
zmin = Cells(21, 2)
zmax = Cells(22, 2)
dz = Cells(23, 2)
ngauss = Cells(24, 2)
theta = Cells(25, 2)
' convert theta to radians for coordinate rotation
theta = (theta / 360#) * 2# * 3.14159265
dt = Cells(28, 2)
'read in well data
For m = 1 To nheaters
  x0(m) = Cells(31 + m, 1)
  y0(m) = Cells(31 + m, 2)
'transform well coordinates to rotated system
'x0p and y0p are now in transformed coordinate, not original
  x0p(m) = x0(m) * Cos(theta) + y0(m) * Sin(theta)
  y0p(m) = -x0(m) * Sin(theta) + y0(m) * Cos(theta)
Next m
'
'read in observation locations if iflag < 0
If iflag < 0 Then
  nobs = Cells(2, 9)
  For i = 1 To nobs
    xobs(i) = Cells(3 + i, 8)
    yobs(i) = Cells(3 + i, 9)
    zobs(i) = Cells(3 + i, 10)
  Next i
End If
'
'read in time dependent heating rate for the heaters
'
tstart = Cells(26, 2)
tend = Cells(27, 2)
' change end time to be relative to jan 1
```

```
tend = tend + tstart
ntobs = (tend - tstart) / dt - 0.5
times = tend * 86400
npstart = (tstart / 30.4375) - 0.5 + 1
tp(npstart) = tstart * 86400#
npend = (tend / 30.4375) - 0.5 + 1
 For k = npstart To npend
'  heating rate during period k
  Q(k) = Cells(k + 3, 6)
'  time when period k starts, typically multiples of 30.4375 days
  If k > npstart Then
    tp(k) = (k - 1) * 30.4375 * 86400
  End If
 Next k
'
'compute main coefficients in PDE
cbar = (1 - por) * Cr * rhorock + por * 4200# * 1000#
vbar = Vd * 1000# * 4200#
vtot = vbar / cbar
If vtot = 0# Then vtot = 0.000000001
alpha = lambda / cbar
const1 = 1# / (2# * 3.14159265 * d * lambda)
'for steady state divide const1 by 2
dbot = dtop + d
' compute weights and abcissas for Gaussian Quadrature
' this is done for twice for the two integrals
'*********************************************************************
'Call GAULEG(dtop, dbot, xgauss1, wgauss1, ngauss)
'Call GAULEG(-dtop, -dbot, xgauss2, wgauss2, ngauss)
'*********************************************************************
'    weights for first integral
'
    eps = 0.00000000000003
      m = (ngauss + 1) / 2
      XM = 0.5 * (dbot + dtop)
      XL = 0.5 * (dbot - dtop)
      For i = 1 To m
        Z = Cos(3.141592654 * (i - 0.25) / (ngauss + 0.5))
1         P1 = 1#
          P2 = 0#
          For j = 1 To ngauss
            P3 = P2
            P2 = P1
            P1 = ((2# * j - 1#) * Z * P2 - (j - 1#) * P3) / j
```

```
        Next j
        PP = ngauss * (Z * P1 - P2) / (Z * Z - 1#)
        z1 = Z
        Z = z1 - P1 / PP
      If Abs(Z - z1) > eps Then GoTo 1
      xgauss1(i) = XM - XL * Z
      xgauss1(ngauss + 1 - i) = XM + XL * Z
      wgauss1(i) = 2# * XL / ((1# - Z * Z) * PP * PP)
      wgauss1(ngauss + 1 - i) = wgauss1(i)
    Next i
'
'   weights for second integral
    XM = 0.5 * (-dtop - dbot)
    XL = 0.5 * (-dtop + dbot)
    For i = 1 To m
      Z = Cos(3.141592654 * (i - 0.25) / (ngauss + 0.5))
2       P1 = 1#
        P2 = 0#
        For j = 1 To ngauss
          P3 = P2
          P2 = P1
          P1 = ((2# * j - 1#) * Z * P2 - (j - 1#) * P3) / j
        Next j
        PP = ngauss * (Z * P1 - P2) / (Z * Z - 1#)
        z1 = Z
        Z = z1 - P1 / PP
      If Abs(Z - z1) > eps Then GoTo 2
      xgauss2(i) = XM - XL * Z
      xgauss2(ngauss + 1 - i) = XM + XL * Z
      wgauss2(i) = 2# * XL / ((1# - Z * Z) * PP * PP)
      wgauss2(ngauss + 1 - i) = wgauss2(i)
    Next i
'
'****skip shapshots for negative iflag
Cells(2, 13) = "        "
If iflag < 0# Then GoTo 100
'
'*********************************************************************
'*********************************************************************
'
nx = (xmax - xmin) / dx
ny = (ymax - ymin) / dy
nz = (zmax - zmin) / dz
'
```

```
' make an x-y plot at depth z=zz first
'*********************************************************************
'x loop
For i = 0 To nx
  x = xmin + i * dx
' transformed xp
  Cells(6, 12 + i) = x
  'y loop
  For j = 0 To ny
    y = ymin + j * dy
    Cells(7 + j, 11) = y
    'transform x and y to rotated system xp, yp
    xp = x * Cos(theta) + y * Sin(theta)
    yp = -x * Sin(theta) + y * Cos(theta)
    'add superposition loop
    ' sum is for spatial superposition summation
    Sum = 0#
'  heater loop
    For m = 1 To nheaters
'   time loop for superposition in time for each heater 2/14/21
     sumt = 0#
     For k = npstart To npend
'     sumg is for gaussian quadrature summation
      sumg1 = 0#
      sumg2 = 0#
      const2 = Exp(vtot * (xp - x0p(m)) / (2# * alpha))
' avoid singularity at line sources
       distxy2 = ((xp - x0p(m)) ^ 2 + (yp - y0p(m)) ^ 2)
       If distxy2 < 0.1 Then distxy2 = 0.1
'  gaussian quadrature loop
        For n = 1 To ngauss
         zprime1 = xgauss1(n)
         zprime2 = xgauss2(n)
         dist1 = (distxy2 + (zz - zprime1) ^ 2) ^ 0.5
         dist2 = (distxy2 + (zz - zprime2) ^ 2) ^ 0.5
         f1 = f(vtot, dist1, (times - tp(k)), alpha)
         f2 = f(vtot, dist2, (times - tp(k)), alpha)
         sumg1 = sumg1 + wgauss1(n) * f1
         sumg2 = sumg2 + wgauss2(n) * f2
        Next n
'  end of integration
       deltT1 = (Q(k) - Q(k - 1)) * const1 * const2 * (sumg1 - sumg2)
       sumt = sumt + deltT1
      Next k
```

```
      deltT = sumt
     Sum = Sum + deltT
    Next m
    t = T0 + Sum
    Cells(7 + j, 12 + i) = t
  Next j
Next i
'
'*********************************************************************
' make an x-z plot at y=yy
'
y = yy

'x loop
For i = 0 To nx
  x = xmin + i * dx
  Cells(60, 12 + i) = x
  'transform x to xp for rotation
  xp = x * Cos(theta) + yy * Sin(theta)
  'transform y to yp for rotation
  yp = -x * Sin(theta) + y * Cos(theta)
  'z loop
  For j = 0 To nz
    Z = zmin + j * dz
    Cells(61 + j, 11) = Z
    'add superposition loop
    ' sum is for superposition summation
    Sum = 0#
    For m = 1 To nheaters
'     sumg is for gaussian quadrature summation
      sumg1 = 0#
      sumg2 = 0#
  const2 = Exp(vtot * (xp - x0p(m)) / (2# * alpha))
' avoid singularity at line sources
      distxy2 = ((xp - x0p(m)) ^ 2 + (yp - y0p(m)) ^ 2)
      If distxy2 < 0.1 Then distxy2 = 0.1
'  gaussian quadrature loop
        For n = 1 To ngauss
          zprime1 = xgauss1(n)
          zprime2 = xgauss2(n)
          dist1 = (distxy2 + (Z - zprime1) ^ 2) ^ 0.5
          dist2 = (distxy2 + (Z - zprime2) ^ 2) ^ 0.5
          f1 = f(vtot, dist1, times, alpha)
          f2 = f(vtot, dist2, times, alpha)
```

```
        sumg1 = sumg1 + wgauss1(n) * f1
        sumg2 = sumg2 + wgauss2(n) * f2
      Next n
'  end of integration
     deltT = Q(m) * const1 * const2 * (sumg1 - sumg2)
     Sum = Sum + deltT
   Next m
   t = T0 + Sum
   Cells(61 + j, 12 + i) = t
  Next j
Next i
'
100  Cells(2, 13) = "skipped"
'
If iflag > 0# Then GoTo 200
Cells(86, 9) = "test"
'
'
'*********************************************************************
' make time-series at the nobs observation locations
'*********************************************************************
'
'loop over observation times
For j = 1 To ntobs
 atimes = ((j - 1) * dt + dt + tstart) * 86400
 npend = ((atimes / 86400) / 30.4375) - 0.5 + 1
 Cells(85 + j, 8) = atimes / 86400#
'loop over observation points
For i = 1 To nobs
  x = xobs(i)
  y = yobs(i)
  Z = zobs(i)
    'transform x and y to rotated system xp, yp
   xp = x * Cos(theta) + y * Sin(theta)
   yp = -x * Sin(theta) + y * Cos(theta)
    'add superposition loop
    ' sum is for spatial superposition summation
   Sum = 0#
'  heater loop
   For m = 1 To nheaters
'   time loop for superposition in time for each heater 2/14/21
    sumt = 0#
    For k = npstart To npend
'    sumg is for gaussian quadrature summation
```

```
      sumg1 = 0#
      sumg2 = 0#
      const2 = Exp(vtot * (xp - x0p(m)) / (2# * alpha))
' avoid singularity at line sources
       distxy2 = ((xp - x0p(m)) ^ 2 + (yp - y0p(m)) ^ 2)
       If distxy2 < 0.1 Then distxy2 = 0.1
'  gaussian quadrature loop
         For n = 1 To ngauss
          zprime1 = xgauss1(n)
          zprime2 = xgauss2(n)
          dist1 = (distxy2 + (Z - zprime1) ^ 2) ^ 0.5
          dist2 = (distxy2 + (Z - zprime2) ^ 2) ^ 0.5
          f1 = f(vtot, dist1, (atimes - tp(k)), alpha)
          f2 = f(vtot, dist2, (atimes - tp(k)), alpha)
          sumg1 = sumg1 + wgauss1(n) * f1
          sumg2 = sumg2 + wgauss2(n) * f2
        Next n
'  end of integration
        deltT1 = (Q(k) - Q(k - 1)) * const1 * const2 * (sumg1 - sumg2)
        sumt = sumt + deltT1
       Next k
       deltT = sumt
      Sum = Sum + deltT
    Next m
    t = T0 + Sum
    Cells(85, 8 + i) = i
    Cells(85 + j, 8 + i) = t
Next i
'
Next j
'
200  Cells(2, 13) = "not skipped"
'
End Sub
    Function f(v, r, t, a)
'  function that is integrated
    a1 = -v * r / (2# * a)
    b1 = (r - v * t) / (2# * (a * t) ^ 0.5)
    a2 = v * r / (2# * a)
    b2 = (r + v * t) / (2# * (a * t) ^ 0.5)
    f = (1# / (4# * r)) * (exer(a1, b1) + exer(a2, b2))
' for steady state, divide const1 by 2 and use f = (1# / r) * (Exp(a1))
    End Function
Function exer(a, b)
```

```
'    function from vanGenucten and Alves (1982) to evaluate
' Exp(a) * Erfc(b) originally from Javandel book, converted to vba falta 1/1/21
     exer = 0#
     If Abs(a) > 170# And b < 0# Then GoTo 140
     If b <> 0# Then GoTo 100
    exer = expd(a)
   GoTo 140
100   C = a - b * b
     If Abs(C) > 170# And b > 0# Then GoTo 140
     If C < -170# Then GoTo 130
   x = Abs(b)
   If x > 3# Then GoTo 110
   t = 1# / (1# + 0.3275911 * x)
   y = t * (0.2548296 - t * (0.2844967 - t * (1.421414 - t * (1.453152 - 1.061405 * t))))
   GoTo 120
110     y = 0.5641896 / (x + 0.5 / (x + 1# / (x + 1.5 / (x + 2# / (x + 2.5 / (x + 1#))))))
120   exer = y * expd(C)
130  If b < 0# Then exer = 2# * expd(a) - exer
140    End Function
      Function expd(x)
'    arguments less than -170 return zero
     expd = 0#
     If x < -170# Then GoTo 100
   expd = Exp(x)
100    End Function

Sub ClearRanges()

Range("K1:BZ82") = ""
Range("H86:R10000") = ""
Range("I85:W85") = ""

End Sub
```